

STUDY OF TWO-PARTICLE RESPONSE AND PHASE CHANGES IN STRONGLY CORRELATED SYSTEMS USING DYNAMICAL MEAN FIELD THEORY

By

BISMAYAN CHAKRABARTI

A dissertation submitted to the
Graduate School—New Brunswick
Rutgers, The State University of New Jersey
in partial fulfillment of the requirements
for the degree of
Doctor of Philosophy
Graduate Program in Physics and Astronomy
written under the direction of
Prof. Kristjan Haule
and approved by

New Brunswick, New Jersey

December, 2016

ABSTRACT OF THE DISSERTATION

Study of two-particle response and phase changes in strongly correlated systems using Dynamical Mean Field Theory

By BISMAYAN CHAKRABARTI

Dissertation Director:

Prof. Kristjan Haule

The study of strongly correlated materials is currently perhaps one of the most active areas of research in condensed matter physics. Strongly correlated materials contain localized electronic states which are often hybridized with more itinerant electrons. This interplay between localized and delocalized degrees of freedom means that these compounds have highly complex phase diagrams which makes these compounds very challenging to understand from a theoretical standpoint. Computer simulations have proved to be an invaluable tool in this regard with state of the art ab-initio simulation techniques harnessing the ever-increasing power of modern computers to produce highly accurate descriptions of a variety of strongly correlated materials. One of the most powerful simulation techniques currently in existence is Dynamical Mean Field Theory (DMFT). This thesis describes this powerful simulation technique and its applications to various material systems, as well as addressing some theoretical questions concerning particular implementations of DMFT.

This thesis is divided into two parts. In part 1, we describe the theory behind DMFT and its amalgamation with Density Functional Theory (DFT+DMFT). In chapters 2 and 3, we provide the basic theory behind DFT and DMFT respectively. In chapter 4, we describe how these two methods are merged to give us the computational framework that is used in this thesis, namely DFT+DMFT. Finally, we round off part 1 of the thesis in chapter 5, which provides a description of the Continuous Time Quantum Monte Carlo (CTQMC) impurity solver, which is at the heart of the DFT+DMFT algorithm and is used extensively throughout this thesis.

In part two of the thesis, we apply the DFT+DMFT framework to address some important problems in condensed matter physics. In chapter 6, we study the Magnetic Spectral Function of strongly correlated f-shell materials to understand two important problems in condensed matter physics, namely the volume collapse transition in Cerium and the valence fluctuating state ground state of δ -Pu. In chapter 7, we study the contribution of lattice parameters and electronic entropy to study the decades-old problem of understanding the spin state transition observed in LaCoO_3 , where we show how lattice expansion, octahedral rotations and electronic entropy are all essential in stabilizing the high-spin state at high temperature. In chapter 8, we switch to studying a more theoretical problem by looking at the problems with using the highly popular constrained Random Phase Approximation (cRPA) method to estimate the screening of local inter-electronic repulsion in strongly correlated systems. We show that cRPA systematically underestimates screening in such systems which makes it an unsuitable method for estimating the repulsion parameter (U) used in impurity solvers. We then develop an alternate method to estimate the screening using the full local polarization which overcomes many of these limitations. Chapter 9 contains all the conclusions obtained in this thesis, followed by references and appendices.

Acknowledgments

I would like to start by thanking Prof. Kristjan Haule for all the help provided by him over the course of my Ph.D. None of this work would have been possible without his constant support, intellectual freedom, guidance as well the computational resources provided by him.

I would also like to thank Prof. Gabriel Kotliar, for all the help he has so freely provided as well as his valuable insight which I have gained a lot from, especially during my study of magnetic spectrum of f-shell materials.

I have gained most of my expertise in physics from the courses taught here at Rutgers by the highly knowledgeable faculty in the physics department. I would like to thank all the professors I have taken courses with, as well the entire faculty of the condensed matter department who have always inspired me with their great dedication to constantly pushing the limits of human knowledge.

Over the course of my dissertation, I have had the opportunity to work with a number of highly talented post-doctoral scholars and doctoral students whom I have collaborated closely with. Dr. Maria Pezzoli was a great help during my initial research on magnetic properties of materials. Dr. Turan Birol has been a constant source of help and support over the last three years of my research and I have gained a lot from his knowledge of physics and life in general. Dr. Chuck Hou Yee has also been a trusted friend and colleague who has always been available whenever I had a question about physics, science or computation in general. Qiang Han and I had a great experience working on the project estimating screening in correlated systems and I wish him the best in all his future endeavors.

In addition to this, the Rutgers has also provided me with a valuable set of friends who have made my experience as a graduate student a lot more enjoyable. To Aniket, Juho, Patrick, Conan, Upamanyu, Dinesh, Kartik, Rahul, Hitesh, Kinnari, Shree, Samruddhi and all the other friends I have been fortunate enough to make at Rutgers, I would like to thank all of you for all the immensely enjoyable experiences which have made my time at Rutgers some of the best years of my life.

Finally, I would like to thank my parents, my sister and my entire extended family for always being there for me whenever I have needed them. Your love and support inspires me to always strive for excellence in whatever I do and I am truly lucky to have been born into a family which has such kind and loving individuals.

Dedication

To my family and friends

Table of Contents

| | |
|---|------|
| Abstract | ii |
| Acknowledgments | iv |
| Dedication | v |
| List of Tables | viii |
| List of Figures | ix |
| 1. Introduction | 1 |
| I The DFT+DMFT Method | 7 |
| 2. Density Functional Theory | 8 |
| 3. Dynamical Mean Field Theory | 13 |
| 3.1. Basics of DMFT | 15 |
| 4. DFT+DMFT | 19 |
| 4.1. A functional Reformulation of DMFT | 19 |
| 4.2. Merging DFT with DMFT | 23 |
| 5. Continuous Time Quantum Monte Carlo Impurity Solver | 28 |
| 5.1. Introduction | 28 |
| 5.2. Details of the Algorithm | 29 |
| II Applications | 32 |
| 6. Calculation of Magnetic Spectral function and Dynamic Magnetic Susceptibility for f-shell materials | 34 |
| 6.1. Details of theory and calculation techniques | 34 |

| | |
|---|------------|
| 6.2. Applications to Real Materials | 41 |
| 7. Spin State Transition in LaCoO_3 | 56 |
| 7.1. Introduction | 56 |
| 7.2. Crystal Structure of LaCoO_3 | 58 |
| 7.3. Density of States | 60 |
| 7.4. The spin state transition | 63 |
| 7.5. Nature of the excited spin state | 64 |
| 7.6. Contribution of Electronic Entropy | 67 |
| 7.7. Summary | 68 |
| 8. Investigation into the inadequacy of cRPA in reproducing screening in strongly correlated systems | 69 |
| 8.1. Introduction | 69 |
| 8.2. Models and Methods | 71 |
| 8.3. Results | 76 |
| 8.4. Discussion and Conclusion | 85 |
| 9. Conclusion | 87 |
| Bibliography | 90 |
| Appendix A. Details of the calculation of Local Screening | 102 |

List of Tables

| | | |
|------|--|----|
| 6.1. | Values of the orbital (μ_L) and spin (μ_S) magnetic moment as obtained in our DFT+DMFT calculations under a magnetic field of 10T. The coefficient $C_2 = \mu_L/(\mu_L + \mu_S)$ determines the shape of the form factor in the dipole approximation and has similar value in both phases. | 44 |
| 6.2. | Comparison of the probabilities of different occupations of the 5f orbital predicted by CHPES and DMFT | 51 |
| 8.1. | Table containing interaction parameters used for the two different Hamiltonians in use in our simulations | 76 |
| 8.2. | Comparison between static values of u_{dd}^{cRPA} and u_{dd}^{cLoc} for different values of bare U in the dp model. | 82 |

List of Figures

| | |
|--|----|
| 1.1. Examples of emergent behavior in nature: (from left) 1) swarms of birds displaying complex behavior. 2) Snowflakes of complex different shapes formed by the same fundamental solid phase of water ¹ | 2 |
| 1.2. The Kmetko-Smith diagram showing the trends in increasing electronic correlation/localization across different shells of the periodic table. The elements at the bottom left corner display the least amount of correlations and form conventional superconductors at low temperatures. At the other extreme elements in top right corner show extremely high localization and typically form local moments which give rise to magnetism ² . | 3 |
| 1.3. The phase diagram of a cuprate superconductor showing the multitude of different phases that can exist in a strongly correlated system ³ | 4 |
| 3.1. Schematic diagram showing the basic DMFT approximation where an interacting lattice system is mapped to an impurity model hybridized with a self-consistently determined bath ⁴ | 14 |
| 4.1. (a) The free energy $F = F[G]$, as a functional of the Greens function G , is originally generally not stationary at the physical Green's function G^0 of the system. (b) In contrast, the Baym-Kadanoff functional $\Gamma[G]$ obtained after performing the Legendre Transform becomes stationary at G^0 and has the value of the physical free energy $\Gamma[G^0] = F^0$ at its stationary point | 20 |
| 4.2. Diagrammatic representation of the full Luttinger-Ward functional containing all the two-particle irreducible skeleton diagrams | 22 |
| 4.3. Diagrammatic representation of the DMFT approximation to the Luttinger-Ward functional with all propagators being replaced by local propagators | 23 |
| 4.4. The DFT+DMFT loop as implemented in the WienDMFT Package | 26 |
| 6.1. The Temperature vs Pressure Phase diagram for Cerium showing the multiple phases of the material. We shall be concentrating on the volume collapse transition between α -Ce and γ -Ce | 41 |
| 6.2. Diagram showing the Volume collapse transition between α -Ce and γ -Ce, where the FCC lattice is retained but unit cell volume decreases | 42 |

| | | |
|-------|---|----|
| 6.3. | Momentum transfer dependence of the normalised magnetic form factor $F_M^2(Q)$ of α -Ce and γ -Ce. Blue circles show experimental data taken from Ref.[90]. | 44 |
| 6.4. | Imaginary part of the local dynamic magnetic susceptibility, $\text{Im}\chi(\omega)$, for α and γ cerium (yellow dotted and red dashed lines respectively). The inset shows the static susceptibility $\chi(q, \omega = 0)$ of α cerium as a function of q in the first Brillouin zone. Note that the q goes from the points (0,0,0) to (1,1,-1) in 12 uniform steps. | 45 |
| 6.5. | Difference of $S(q, \omega)$ between α and γ phase : Left panel shows DFT+DMFT results. Right panel shows high energy neutron inelastic measurements, taken from Ref [90]. | 48 |
| 6.6. | a) The Volume vs Temperature Phase diagram for Plutonium showing the multiple phases of the material. b) The FCC unit cell of δ -Pu | 50 |
| 6.7. | The DMFT form factor obtained by our simulations for δ -Pu, together with neutron scattering results at 250 and 500 meV incident neutron energies and the form factors that would have been obtained by considering a pure $5f^4$ or $5f^5$ valence, as well as a admixture of the two | 52 |
| 6.8. | The imaginary part of the local dynamic susceptibility for δ -Pu compared to neutron scattering experiment [68] | 53 |
| 6.9. | Illustrative figure showing how the magnetic moment is screened by the Kondo screening cloud below the Kondo temperature T_K . Taken from [68] | 54 |
| 6.10. | The Magnetic Spectral Function $S(q, \omega)$ for δ -Pu compared to neutron scattering experiment [68]. The dashed lines on the experimental figure denote the Q and ω values used to obtain the form factor and the susceptibility. The peak position corresponding to $k_B T_K$ is also marked | 55 |
| 7.1. | Schematic illustration of the two different scenarios for the the spin state transition in LaCoO_3 | 57 |
| 7.2. | Conventional cell for a perovskite with no octahedral rotations ($a^0 a^0 a^0$ structure). In LaCoO_3 , the green atoms would be La, the red atoms O and the blue atom Co. The figure also shows the octahedra formed by the oxygen atoms around the Co atom | 59 |
| 7.3. | A depiction of the pattern of octahedral rotations that is present in LaCoO_3 . Each of the oxygen octadra rotates in opposite direction to all nearest neighbour octahedra by the same amount relative to all three coordinate axes ($a^- a^- a^-$ structure). | 60 |
| 7.4. | Density of states (t_2g, e_g and total including all atoms) for all four structures at 116K and 1160K. | 61 |

| | | |
|------|---|----|
| 7.5. | (a) Evolution of $ S_z $ with temperature for all four structures. (b) Evolution of Density of states at fermi level with temperature for all four structures. | 62 |
| 7.6. | Evolution of occupation probabilities for all the spin states for the four structures with temperature. | 65 |
| 7.7. | Occupancy histogram showing the occupancy Probability for the different atomic states for the d orbital of the Co atom for all the four structures at two different temperatures. The different background colors mark the areas reserved for different spin sectors. The lower x axis ticks as well as the color of the histogram bars denote the different occupancies of the d orbital. Note that odd occupancies only allow half integer values of $ S_z $ while even ones allow integer values | 66 |
| 7.8. | A depiction of the switch in stability between the LTa^- and HTa^- structures due to the impact of electronic entropy. | 67 |
| 8.1. | (a)-(b):orbital-resolved dos of dp model with $\mu = 0.28, n_p = 1.78, n_d = 1.22$ and dps model with $\mu = 0.038, n_p = 1.70, n_s = 0.14$ and $n_d = 1.16$.(c)-(d):band structure showing orbital characters of dp model and dps model. The dashed line denotes the chemical potential μ | 72 |
| 8.2. | The Polarization bubble used in the RPA approximation. Note that the variables \vec{k} and Ω are summed over as per usual Einstein summation convention. | 74 |
| 8.3. | a) Figure showing the RPA screening process to obtain the fully screened interaction W from the unscreened interaction V. b) Figure showing the cRPA process to obtain the partially screened u from the unscreened interaction V. | 74 |
| 8.4. | Comparison of $\text{Im}\Sigma$ in all orbital channels in “2-orb/3-orb” scenario for (a) dp model with $U_{dd} = 4.5$ and (b) dps model with $U_{dd} = 6.0$ | 77 |
| 8.5. | u_{dd}^{cRPA} and W_{dd}^{RPA} of the dp(dps) model predicted by (c)RPA is shown in red (blue).The dark dashed horizontal line denotes the bare value of U_{dd} used in dp and dps model. Note that both u_{dd}^{cRPA} and W_{dd}^{RPA} approach the bare value in the limit of high frequency as expected(not shown here). | 78 |
| 8.6. | Comparison of dos of d orbital (d-DOS) within three scenarios for (a) dp model with $U_{dd} = 4.5$ and (b) dps model with $U_{dd} = 6.0$ | 79 |
| 8.7. | Comparison of the quasiparticle residue of the three scenarios varying U_{dd} in (a) dp model with $U_{pp} = 0.2U_{dd}, U_{pd} = 0.8U_{dd}$ and (b) dps model with $U_{pp} = U_{ss} = U_{ps} = 0.1U_{dd}, U_{pd} = 0.6U_{dd}, U_{ds} = 0.3U_{dd}$ | 80 |

| | | |
|-------|---|-----|
| 8.8. | Occupation of d orbital (n_d) in dp model varying U_{dd} with $U_{pp} = 0.2U_{dd}$, $U_{pd} = 0.8U_{dd}$ of 1-orb bare and 2-orb scenario. MIT(1-orb bare) and MIT(2-orb) are transition points inferred from the quasiparticle residue results. | 81 |
| 8.9. | Plot showing the u^{cLoc} and W^{Loc} for $U_{dd} = 2.5$ (top) and $U_{dd} = 4.5$ (bottom) using the Local Polarization method. The RPA W^{RPA} and cRPA u^{cRPA} for both sets of parameters is also shown for comparison. Note: For both runs $U_{pp} = 0.2U_{dd}$; $U_{dp} = 0.8U_{dd}$. Inset shows a magnified portion of the plot for u^{cRPA} and u^{cLoc} near $\omega \rightarrow 0$ | 83 |
| 8.10. | Plot showing the p orbital and d-orbital density of states using two-orbital DMFT (“2-orb”) and effective one-orbital DMFT using the Local Polarization method (“1-orb cLoc”) and cRPA (“1-orb cRPA”). The top two figures are for $U_{dd} = 2.5$ whereas the bottom two are for $U_{dd} = 4.5$ | 84 |
| A.1. | Diagrammatic Representation of a general matrix element of the local Polarization bubble. The blue shading indicates that we take into account all interaction processes inside the impurity. α and β are condensed spin and orbital indices. It is to be noted that we only calculate the local (impurity) bubble hence there is no q dependence | 102 |
| A.2. | Diagrammatic representation of the procedure to calculate the new screened interaction parameters using the local Polarization | 104 |

Chapter 1

Introduction

Condensed Matter Physics involves the scientific study of the properties of macroscopic collections of particles . In a rich history spanning a century since the birth of quantum mechanics, Condensed Matter Physics has grown into one of the most active fields of physics and has had a direct role in enabling the technological revolution that the human species is currently living through. In most fields of physics, the fundamental concept which underlies most research is that of “Reductionism”, which is the belief that every phenomenon exhibited by a system can be explained by understanding the fundamental properties of its most elementary constituents. However, the basic philosophy of condensed matter physics is perhaps best summarized by the oft-quoted phrase coined by P.W Anderson- ”More is different”. It captures the idea that a macroscopic collection of matter exhibits properties which are hard to predict based on merely the microscopic equations governing the individual constituents. This idea, which is known as “Emergence”, is the guiding principle behind the phenomenon that condensed matter physicists strive to understand in the realm of the quantum properties of materials. Some simple examples of emergent properties (see Fig 1.1) include water molecules forming complex waves in water bodies and intricately shaped snow flakes in winter, swarms of living organisms exhibiting behaviors much more complicated than individual members, or perhaps most stunningly, how a collection of lifeless chemical elements can combine to form something as complex as a human being. In condensed matter, the study of emergent properties in material systems has given us a keen understanding of why materials comprised of very similar chemical constituents might behave as a metal,insulator, semiconductor, magnet, superconductor or a variety of other complex phases known to us depending on differences in crystal structure, temperature, pressure or a variety of other controlling factors. The ability to understand and thereby control these material properties have resulted in condensed matter physics having a great impact in engineering and technology, making it a field of physics which has a pronounced real-world impact in society.

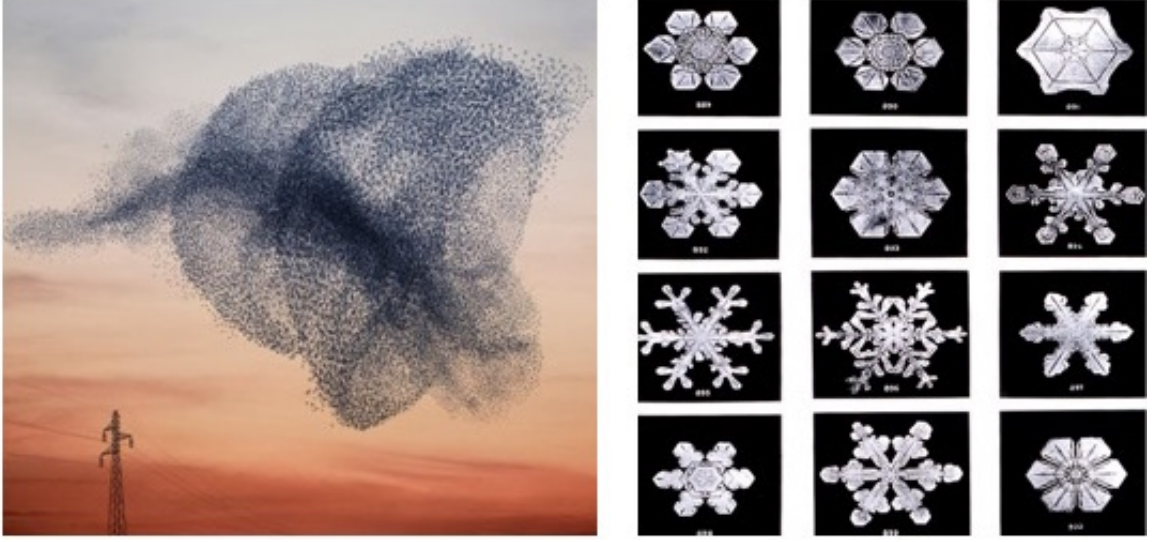


Figure 1.1: Examples of emergent behavior in nature: (from left) 1) swarms of birds displaying complex behavior. 2) Snowflakes of complex different shapes formed by the same fundamental solid phase of water ¹

Within condensed matter, one of the most active and fascinating fields is the study of strongly correlated systems. In most materials (like those where the constituent elements only have open s and p shells), the somewhat naive yet powerful approximation that the electrons in the material act as independent particles moving in an effective medium, known as the independent electron approximation works surprisingly well. This effect, which is explained by the Landau Fermi Liquid Theory, occurs due to these extremely mobile itinerant electrons forming bands consisting of "quasiparticles", which result in the inter-electronic coulomb repulsion being screened highly effectively. This success of the Landau Fermi liquid theory and other theoretical approximation schemes has meant that we have quite a good understanding of the properties of these "weakly correlated systems" (though some particular systems still remain challenging).

However this approximation usually breaks down in materials with incomplete d and f shells, because the electrons in these shells are localized to a much greater extent around their parent atoms (see Fig 1.2). These electrons cannot effectively screen each other, unlike the much more itinerant s and p electrons and therefore retain some of their atomic properties and become highly correlated due to the interactions between them. In addition, there is often strong mixing (hybridization) between them and the outer s and p electrons, leading to a large interplay between itinerant and localized degrees of freedom. Such materials, commonly known as *strongly correlated systems*, often

¹Sources-1) fuelspace.org 2) Wikipedia

have highly complex phase diagrams (see Fig 1.3) with many different phases across which transitions can be tuned by tweaking some external *knob* such as temperature or pressure. This makes these systems particularly useful from a material science/engineering standpoint.

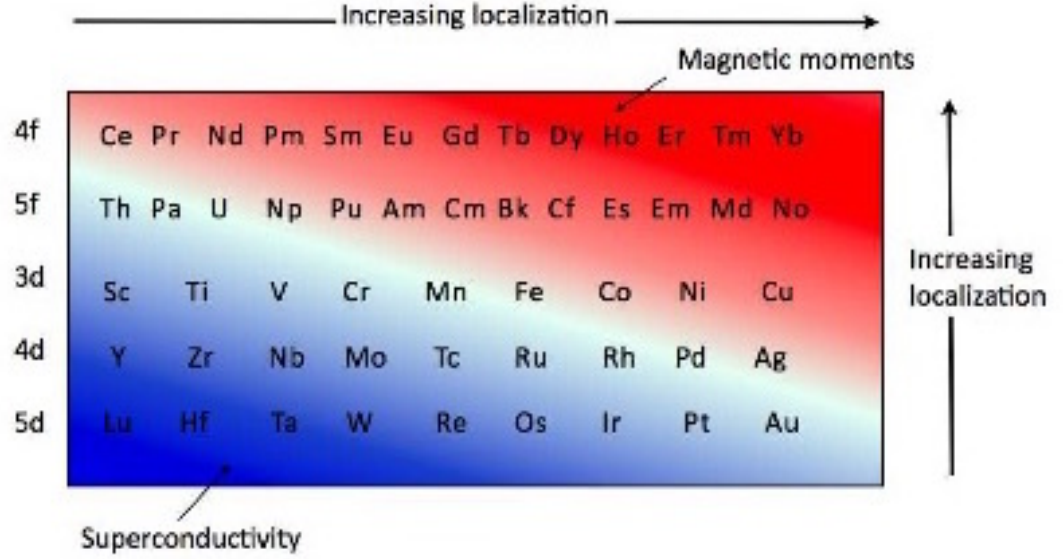


Figure 1.2: The Kmetko-Smith diagram showing the trends in increasing electronic correlation/localization across different shells of the periodic table. The elements at the bottom left corner display the least amount of correlations and form conventional superconductors at low temperatures. At the other extreme elements in top right corner show extremely high localization and typically form local moments which give rise to magnetism ²

²Source- Introduction to Many-Body Physics. Piers Coleman (Cambridge University Press)

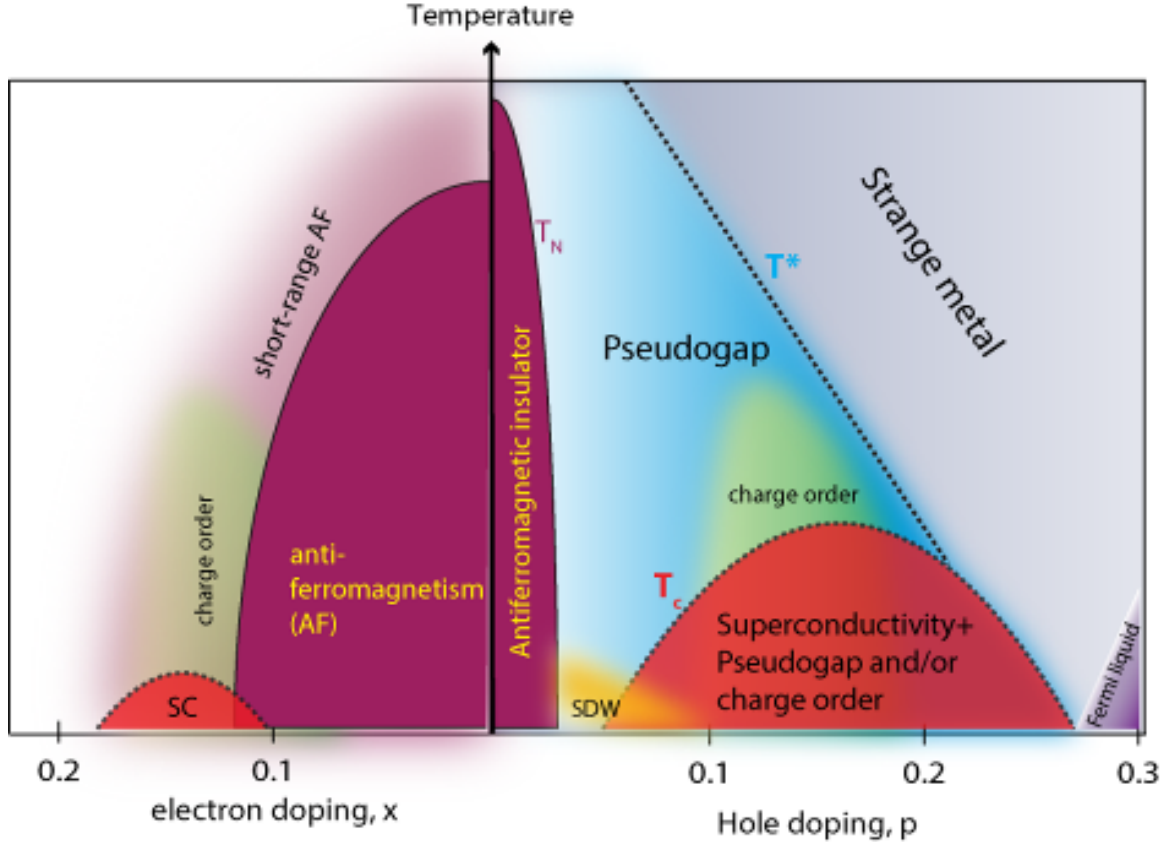


Figure 1.3: The phase diagram of a cuprate superconductor showing the multitude of different phases that can exist in a strongly correlated system ³

Finding a coherent theoretical framework which can capture the essential properties of such complex materials has proved to be immensely challenging and continues to be an area of active research. Computational simulations have played an important role in this effort and have enabled us to study and predict properties of real materials instead of restricting ourselves to model Hamiltonians. These developments have been made possible by large improvements in both the hardware capabilities of modern computers as well as the development of new faster and more powerful simulation algorithms. In the field of weakly correlated materials, Density Functional Theory (DFT) has led to a revolution in material simulation, and has given us the power to compute properties using relatively modest computational resources, which has led to an explosion in research in computational materials physics as well as quantum chemistry. However DFT, while being extremely powerful, is often completely inadequate when applied to strongly correlated systems as the drastic approximations it employs contain only rudimentary treatments of the electronic correlations which are essential to understanding the physics of these compounds (for more details refer to chapters 2

³Source: http://web.mit.edu/~ivishik/www/inna_vishik_files/Page441.htm

and 3).

Dynamical Mean Field Theory (DMFT) is one of the most promising theories which aims to address some of these shortcomings. DMFT provides us a way to simulate strongly correlated systems using controlled approximations which reduce computational complexity while retaining most of the essential physics of the system, including the interplay between itinerant and localized degrees of freedom. This method, which initially became popular as a method to solve model Hamiltonians such as the Hubbard Model, has proved to be a valuable tool to capture the properties of d and f shell systems. This has especially been true in the last decade after the successful merger of DMFT with DFT to yield a framework which is capable of dealing with both the weakly correlated electrons (which DFT is well suited to) as well as the localized d and f orbital electrons, where DMFT shines. This approach, known as DFT+DMFT has proved to be one of the most successful methods in reproducing experimentally verifiable properties of correlated systems and is one of the methods driving the advancement in human understanding in the field of correlated materials .

As result of these and other highly advanced computational techniques available, computational condensed matter today is one of the most exiting fields of physics to be part of. The current algorithms allow us , for perhaps the first time in history, to perform "computational experiments" where we can simulate materials which are extremely difficult to realize experimentally in a reliable and quick manner given sufficient computational resources. It is hoped that soon this would give us the power to perform computational material design, which is perhaps one of the ultimate aims of condensed matter physics. We would then be at a stage where we can solve the inverse problem of having been given a certain set of desired properties, of being able to predict which exact chemical system would satisfy those requirements from first principles without necessarily having to resort to actual experimentation. Since strongly correlated materials display some of the most interesting properties known in nature, it is to be expected that methods such as DFT+DMFT will be at the forefront of such efforts.

In this thesis, we shall study some of the fundamental theoretical aspects of the DFT+DMFT method as well as its applications to real material systems. The thesis is arranged in the following manner: In Part 1 , we shall aim to present a description of the theory behind DFT+DMFT. In chapter 2 we shall give a brief introduction to Density functional Theory (DFT) and the equations which govern the method. In chapters 3 and 4, we shall explain the DMFT method, provide details of the approximations employed in DMFT and explain how the merger of DFT+DMFT is carried out in practice. In Chapter 5 we shall provide more technical details of the Computational algorithm which lies at the heart of our implementation of DFT+DMFT, the Continuous Time Quantum Monte Carlo (CTQMC) impurity solver. Having laid out the major theoretical building blocks of

our framework, in Part 2 we shall move on to particular problems which have been investigated in the course of this doctoral study. Chapter 6 details the investigation of the magnetic spectral function of f-shell compounds such as α Cerium, γ Cerium and δ plutonium. Chapter 7 describes a study (using DFT+DMFT) of the importance of structural parameters and electronic entropy in driving the spin state transition in $LaCoO_3$, which is a problem that has attracted the attention of condensed matter physicists for decades. Chapter 8 contains the investigation of the inadequacy of the Constrained Random Phase Approximation(cRPA), one of the most popular methods to estimate screening in strongly correlated systems and proposes a new way to understand the most important screening processes that dominate at the local level. Chapter 9 contains the conclusion and is followed by the Bibliography and Appendices.

Part I

The DFT+DMFT Method

Chapter 2

Density Functional Theory

Density Functional Theory(DFT) is one of the most successful theories in the world of modern physics. Its immense popularity can be gauged from the fact that the seminal papers by Hohenberg and Kohn [63], and Kohn and Sham [74] are the two most heavily cited papers in modern times. Density functional theory allows for ab-initio (with no arbitrary tunable free parameters) calculations of the zero-temperature ground state material properties of the vast majority of weakly correlated compounds. With the growth of modern algorithms in this field, one can now employ off-the-shelf packages to obtain highly accurate results for a large variety of experimental observables while spending very little computational resources. In this section, we shall concentrate on giving a brief introduction to the principles of DFT, while also mentioning some of the limitations that have led to the search for more advanced methods.

As a starting point for the discussion, we begin with the "Theory of Everything" for condensed matter systems, describing a non-relativistic lattice system of nuclei and the accompanying electrons:

$$H = -\frac{\hbar^2}{2m_e} \sum_i \nabla_i^2 - \frac{\hbar^2}{2M_e} \sum_I \nabla_I^2 + \frac{1}{2} \sum_{i \neq j} \frac{e^2}{|\mathbf{r}_i - \mathbf{r}_j|} - \frac{1}{2} \sum_{i,I} \frac{e^2 Z_I}{|\mathbf{r}_i - \mathbf{R}_I|} + \frac{1}{2} \sum_{I \neq J} \frac{e^2 Z_I Z_J}{|\mathbf{R}_I - \mathbf{R}_J|} \quad (2.1)$$

In this equation, the first two terms describe the kinetic energy of the nuclei and the electrons respectively while the next three terms describe the inter-nuclear, nuclei-electron and electron-electron Coulomb interactions, with \mathbf{R} (\mathbf{r}) denoting the positions of the nuclei (electrons). Note that this equation neglects relativistic corrections such as spin orbit coupling which can become important in some systems (and which most advanced DFT packages are able to treat to some degree). We first simplify this equation by adopting the so-called Born-Oppenheimer approximation, whereby the nuclei are assumed to be fixed. This is an exceptionally accurate approximation due to the much higher mass of the nuclei relative to the electrons. This approximation dispenses with the nuclear kinetic energy term and leaves us with a Hamiltonian for the electrons moving in an effective field created by the lattice of nuclei. The resulting Hamiltonian becomes:

$$H = -\frac{\hbar^2}{2m_e} \sum_i \nabla_i^2 + \frac{1}{2} \sum_{i \neq j} \frac{e^2}{|\mathbf{r}_i - \mathbf{r}_j|} + \sum_i V_{ext}(\mathbf{r}_i) + E_{ion} \quad (2.2)$$

Where E_{ion} is the constant inter-nuclear Coulomb term and V_{ext} is the nuclei-electron repulsion given by:

$$V_{ext}(\mathbf{r}) = \sum_I \frac{e^2 Z_I}{|\mathbf{r} - \mathbf{R}_I|} \quad (2.3)$$

However, even this simplified many-electron Schrodinger equation is essentially impossible to solve for more than $O(10)$ electrons due to the extreme computational complexity introduced by the inter-electronic Coulomb repulsion term. The major breakthrough, first proposed by Hohenberg and Kohn [63] was to show that, at least for the calculation of ground state properties, it is sufficient to work with the charge density rather than the electronic wave function itself. Or in other words, the ground state wavefunction Ψ and other observables are uniquely determined by the charge density-

$$n(\mathbf{r}) = \langle \Psi | \psi^\dagger(\mathbf{r}) \psi(\mathbf{r}) | \Psi \rangle \quad (2.4)$$

Note that this leads to enormous decrease in computational complexity, $n(r)$ is a 3 dimensional scalar instead of the original $3N$ dimensional vector Ψ . The result is proved most easily by contradiction. Let us assume that two different external potentials $V_{ext}(r)$ and $V'_{ext}(r)$ produce the same charge density $n(r)$ when plugged into Eq. 2.2. If we denote these two Hamiltonians H and H' , their ground state wavefunctions Ψ and Ψ' and the corresponding ground state energies E and E' , then without loss of generality we can say

$$E' = \langle \Psi' | H' | \Psi' \rangle < \langle \Psi | H' | \Psi \rangle = \langle \Psi | H + V'_{ext}(\mathbf{r}) - V_{ext}(\mathbf{r}) | \Psi \rangle \quad (2.5)$$

where the inequality comes from the fact that Ψ is not the ground state of H' . From this, we get

$$E < E' + \int d\mathbf{r} (V'_{ext}(\mathbf{r}) - V_{ext}(\mathbf{r})) n(\mathbf{r}) \quad (2.6)$$

Since both external potentials give the same charge density, exchanging the primed and unprimed dummy indices, we get

$$E' < E + \int d\mathbf{r} (V_{ext}(\mathbf{r}) - V'_{ext}(\mathbf{r})) n(\mathbf{r}) \quad (2.7)$$

Adding these two equations, we get the obvious contradiction

$$E + E' < E + E' \quad (2.8)$$

Which proves that V_{ext} (and therefore H and its ground state wave function Ψ) is uniquely determined by the charge density.

The other theorem proved by the authors in their paper proves the existence of a universal functional of the charge density $F[n]$ for which the functional

$$E[n] = F[n] + \int d\mathbf{r} n(r) V_{ext}(\mathbf{r}) + E_{ion} \quad (2.9)$$

attains a minimum for the ground state density, and has the value corresponding to the ground state energy at this point. The proof is relatively simple and can be formulated by identifying $F[n]$ as the part of the Hamiltonian given by Eq. 2.2 containing the electronic kinetic and Coulomb interaction terms. Knowledge of the exact formulation of this functional would reduce the solution of any chemical system (at least the ground state properties) to a minimization problem involving only one 3-dimensional quantity (the charge density). However, the only component of $F[n]$ for which an exact formulation can be found is the "Hartree" component. The functional is then redefined as:

$$F[n] = \frac{e^2}{2} \int d\mathbf{r} d\mathbf{r}' \frac{n(\mathbf{r})n(\mathbf{r}')}{|\mathbf{r} - \mathbf{r}'|} + I[n] \quad (2.10)$$

Where $I[n]$ contains everything in $F[n]$ not including the Hartree term, including the kinetic energy and the non-Hartree potential energy contributions. Therefore the central problem of solving any chemical system is the formulation of an accurate $I[n]$.

The first successful attempt at approximating $I[n]$, without which the findings of Hohenberg and Kohn would have remained a mere theoretical exercise, was achieved by Kohn and Sham [74] in their seminal paper. They proposed breaking up $I[n]$ as follows:

$$I[n] = T_s[n] + E_{XC}[n] \quad (2.11)$$

where $T_s[n]$ is the kinetic energy of an auxiliary non-interacting electron system and $E_{XC}[n]$ is known as the "exchange-correlation" energy of the interacting system. $E_{XC}[n]$ was approximated as:

$$E_{XC}[n] = \int d\mathbf{r} n(\mathbf{r}) \epsilon_{XC}(n(\mathbf{r})) \quad (2.12)$$

where $\epsilon_{XC}(n(\mathbf{r}))$ is the exchange correlation energy per electron of a uniform electron gas which can be computed highly accurately using Quantum Monte Carlo simulations. This approximation of using the charge density of a uniform electron gas is known as the Local Density Approximation(LDA) and is perhaps single handedly responsible for revolutionizing computational Condensed Matter Physics.

In practice, DFT is implemented by assuming the following Hamiltonian for N independent electrons:

$$H = \sum_i^N \left[-\frac{\hbar^2}{2m_e} \nabla_i^2 + V_{KS}(\mathbf{r}_i) \right] \quad (2.13)$$

where V_{KS} is the Kohn-Sham Potential which will be derived later. We then find the N lowest eigenstates and eigenenergies of this hamiltonian, which we denote by $|\psi_i\rangle$ and $|\epsilon_i\rangle$ respectively.

These ψ_i 's allow us to calculate the charge density given by:

$$n(\mathbf{r}) = \sum_{i=1}^N |\psi_i|^2 \quad (2.14)$$

Note that this charge density is still the charge density of the auxiliary non-interacting system defined by Eq. 2.13. This formulation though allows us to calculate $T_s[n]$ for this system using the auxiliary wavefunctions ψ_i 's by using the standard expression

$$T_s[n] = -\frac{\hbar^2}{2m_e} \sum_{i=1}^N \int d\mathbf{r} \psi_i^*(\mathbf{r}) \nabla^2 \psi_i(\mathbf{r}) \quad (2.15)$$

Now we have to ensure that V_{KS} is chosen such that the ground state energy of the Hamiltonian defined in Eq. 2.13 corresponds to the stationary value of the Hohenberg-Kohn functional. To ensure this, we vary the functional against ψ :

$$\frac{\delta}{\delta \psi_i^*} \left(E[n] - \sum_{j=1}^N \epsilon_j (\psi_j^* \psi_j - 1) \right) = 0 \quad (2.16)$$

where ϵ_j ensures normalization of the wavefunctions. The solutions to this equation correspond to Eq. 2.13 as long as the Kohn-Sham potential is defined to be

$$V_{KS}(\mathbf{r}) = V_{ext}(\mathbf{r}) + \int d\mathbf{r}' \frac{e^2}{|\mathbf{r} - \mathbf{r}'|} n(\mathbf{r}') + \frac{dE_{XC}(\mathbf{r})}{dn(\mathbf{r})} \quad (2.17)$$

Therefore we have successfully transformed the solution of the original interacting system to the solution of an auxiliary non-interacting eigenvalue problem. The problem however is nonlinear due to the implicit dependence of V_{KS} on $n(\mathbf{r})$ and thereby on the eigenfunctions themselves. The solution is therefore found iteratively, where we perform the following steps till self-consistency:

1. start with an initial guess for the density $n(\mathbf{r})$
2. use it to construct V_{KS} using Eq. 2.17
3. Solve the eigenvalue problem for the Hamiltonian given by Eq. 2.13 to obtain ψ_i and ϵ_i
4. Construct new $n(\mathbf{r})$ using Eq. 2.14 and go back to step 2

From the converged solution, we calculate the ground state energy by :

$$E = \sum_i \epsilon_i - \frac{e^2}{2} \int d\mathbf{r} d\mathbf{r}' \frac{n(\mathbf{r})n(\mathbf{r}')}{|\mathbf{r} - \mathbf{r}'|} + E_{XC}[n] - \int d\mathbf{r} n(\mathbf{r}) V_{XC}(\mathbf{r}) \quad (2.18)$$

It is to be noted that that apart from the ground state, the eigenvalues and eigenfunctions of the Kohn Sham Hamiltonian are meaningless, strictly speaking. However in practice they are often found to be in good agreement with experimental bandstructures and are used as such.

So we see that Density Functional Theory provides us with a valuable tool with which to perform ab-initio simulations of real materials. The success of this method is mainly based on its computational efficiency and ease of implementation, which has resulted in a number of packages being developed such as VASP [77], Quantum Espresso [38], Abinit [40] and Wien2k [19] which offer off-the-shelf implementations which enable researchers to perform reliable and fast simulations even with very limited resources. However DFT fails when applied to materials with strong correlations because of the relatively naive way it treats electronic correlations with LDA approximation (or improvements on it such as GGA, PBE, Hybrid Functionals etc.). Therefore, one needs more advanced methods to simulate such materials, which is exactly where Dynamical Mean Field Theory (described in the next chapter) comes into its own.

Chapter 3

Dynamical Mean Field Theory

In the previous section, we looked at Density Functional Theory (DFT), which is the current workhorse for materials simulation in Condensed Matter Physics. While exceedingly successful in simulating *weakly correlated* systems (those with open s and p shells), DFT is known to be deficient when simulating open d and f shell materials, where the highly localized d and f electrons play an important role determining the physics of the compound. The main issue is the rather rudimentary treatment of electronic correlations in DFT. In the last section, we explained the Local Density Approximation(LDA) where the uniform electron density of a free electron gas is used to estimate the Exchange Correlation functional. There have been improvements to this approximation where we include higher order corrections to the exchange correlation kernel or otherwise tweak the functional to include terms which allow better agreement with experiment. We therefore have a wide variety of functionals such as GGA, PBE, PBESol and Hybrid functionals which are currently the state of the art in DFT material simulations. Most of the implementations of DFT in off-the-shelf packages also include treatments of spin orbit coupling and other relativistic corrections as well as spin-dependent interactions to some degree which allows us to simulate magnetic phases in weakly correlated systems.

However, all of these treatments are unable to capture the strongly correlated behavior of materials with highly localized electrons. Mott Physics for example, whereby certain compounds such as V_2O_3 become insulators even though they have half-filled electronic shells, is completely beyond the scope of standard DFT. These effects often stem from the fact that the electrons in these materials are correlated, i.e- the behavior of one electron depends on that of other electrons in similarly correlated shells. This effect cannot be described by any scheme which assumes point wise locality (or some weaker form thereof) like DFT does. In addition, the correlated objects can be more complicated than simple atomic orbitals, they can be dimers or some higher aggregation of atoms like in VO_2 or molecular orbitals in molecules. So we can have electronic correlations appear in a wide variety of chemical systems where a simple DFT-like treatment is inadequate.

It should be evident that simulations of such highly correlated systems would be highly expensive because in principle we have to solve the true many body quantum mechanical equation such as

Eqn. 2.2, which is computationally intractable as mentioned earlier. One of the most promising approaches to simulating such systems is Dynamical Mean Field Theory (DMFT). Within DMFT, we simulate the correlated system as an impurity containing the correlated degrees of freedom, embedded in a self-consistently determined effective medium which represents the non-correlated itinerant orbitals (see Fig. 3.1). The approach is *mean field* in the sense that we freeze out some of the spatial extent of electronic correlations. However the resulting *mean field* coupling the impurity and the bath is still time-dependent, allowing us to preserve dynamic (quantum) fluctuations. The true power of the method however comes from the ability to employ highly efficient computational *impurity solvers* such as Continuous Time Quantum Monte Carlo (CTQMC) described in the next chapter, which make the formulation computationally tractable. DMFT can also be very efficiently merged with DFT to create DFT+DMFT, wherein the itinerant bath (which represents the weakly correlated s and p shells) can be solved using DFT while the correlated subspace of d and f orbitals is left to the DMFT impurity solvers and self-consistency conditions.

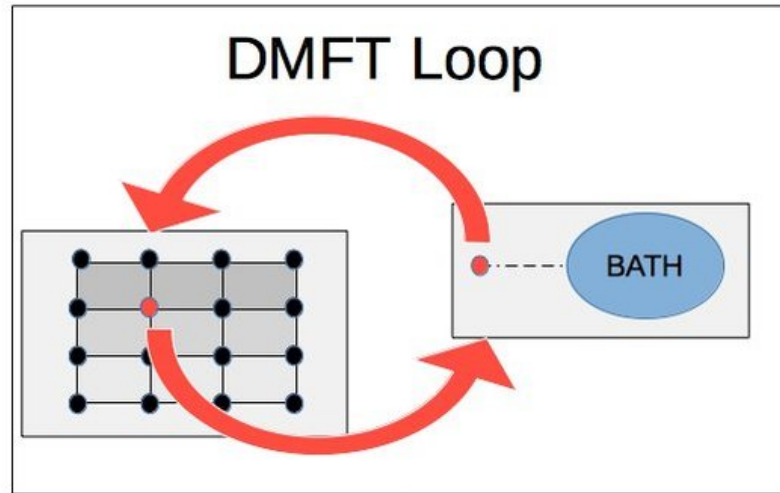


Figure 3.1: Schematic diagram showing the basic DMFT approximation where an interacting lattice system is mapped to an impurity model hybridized with a self-consistently determined bath ¹

¹Source : http://www.theorie.physik.uni-muenchen.de/lsschollwoeck/pollet_group/pollet_bilder/web_bilder_1/dmft_1.jpg

3.1 Basics of DMFT

The simplest model for studying correlated systems is the famous Hubbard Model-

$$H = - \sum_{\langle i,j \rangle, \sigma} t_{ij} c_{i\sigma}^\dagger c_{j\sigma} + U \sum_i n_{i\uparrow} n_{i\downarrow} \quad (3.1)$$

where t_{ij} is the hopping between adjacent sites and U is the on-site Coulomb repulsion. We can write the partition function of this model in the path integral formulation

$$Z = \int \prod_{i\sigma} Dc_{i\sigma}^\dagger Dc_{i\sigma} e^{-S} \quad (3.2)$$

Within DMFT, we simplify the problem by introducing an impurity which we label by site 0 . We then rewrite the action S for the lattice problem as an effective action where the on-site fermionic degrees of freedom on the impurity site are treated exactly. These on-site degrees of freedom are then coupled to an effective time dependent "dynamic" Weiss field which captures the hybridization with the lattice degrees of freedom. This effective action S_{eff} is given by:

$$S_{eff} = \int_0^\beta d\tau \int_0^\beta d\tau' \sum_\sigma c_{0\sigma}^\dagger(\tau) \mathcal{G}_0^{-1}(\tau - \tau') c_{0\sigma}(\tau') + U \int_0^\beta d\tau n_{0\uparrow} n_{0\downarrow} \quad (3.3)$$

where

$$\mathcal{G}_0^{-1}(\tau) = -\frac{\partial}{\partial\tau} - \sum_{ij} t_{j0} G_{ij}^{(0)}(\tau) t_{ik} \quad (3.4)$$

Here \mathcal{G}_0 plays the role of a bare Green's function for the effective impurity problem and can also be thought of as a time-dependent Weiss field. However it is different from the bare Green's function for the original lattice model and captures just the interaction between the lattice bath and the impurity we have constructed. Under this formulation, we can calculate the impurity Green's function under this effective action by :

$$G_{imp}(i\omega_n) = \int_0^\beta d(\tau - \tau') G_{imp}(\tau - \tau') e^{i\omega_n \tau - \tau'} \quad (3.5)$$

where ω_n are the fermionic Matsubara frequencies and

$$G_{imp}(\tau - \tau') = -\langle T_\tau c_0(\tau) c_0^\dagger(\tau') \rangle_{S_{eff}} \quad (3.6)$$

This part of the process is achieved by applying impurity solvers such as CTQMC which calculate the impurity Green's function. Now we write the Green's function of the original Lattice model as :

$$G(k, i\omega_n) = \frac{1}{i\omega - \epsilon_k + \mu - \Sigma(i\omega_n)} \quad (3.7)$$

where $\Sigma(i\omega_n)$ is the self energy. Note that in general the self energy is k -dependent. However within the DMFT approximation it is approximated to be equal to the local part of the self energy. This

approximation is at the heart of DMFT. Detailed accounts of when it can be applied can be found in Ref. [36]. Like most mean field treatments, it becomes exact in the limit of infinite dimensions or more exactly in the limit of infinite co-ordination number. In order to see this one has to look at the diagrammatic expansion for the self energy. By looking at the scaling of the Green's function as the co-ordination number grows, we see that all non-local diagrams between sites i and j scale at least as $1/\sqrt{d_{||i-j||}^3}$ where $d_{||i-j||}$ is the number of equivalent atoms at a manhattan distance of $||i-j||$. However all local diagrams in the self energy scale as $1/\sqrt{d}$. Therefore as the coordination number (or the number of dimensions) approaches $d \rightarrow \infty$, only the local diagrams survive.

Now we have to connect the impurity Green's function calculated by the impurity Green's function to the Lattice Green's function of the original system. In the infinite dimensional limit, it can be shown that that \mathcal{G}_0 in Eq. 3.3 is related to the lattice Green's function of the original system by:

$$\mathcal{G}_0^{-1} = i\omega_n + \mu - \sum_{ij} t_{i0}t_{0j} \left[G_{ij} - \frac{G_{i0}G_{0j}}{G_{00}} \right] (i\omega_n) \quad (3.8)$$

where G_{00} denotes the local (k-summed) Green's function of the lattice.

$$G_{00}(i\omega_n) = \sum_k G(k, i\omega_n) \quad (3.9)$$

The term subtracted from Eq. 3.4 comes due to the so called "cavity construction" formulation where one takes out the impurity and treats it as a "cavity", and is one of the simplest ways to arrive at the DMFT equations (the reader can find a more detailed proof in [58, 36]). Now using the properties of Fourier transforms, we arrive at the following identities-

$$\sum_i t_{0i}G_{i0} = \sum_k \epsilon_k G_k = (i\omega + \mu - \Sigma)G_{00} - 1 \quad (3.10)$$

$$\sum_i t_{0i}G_{ij}t_{j0} = \sum_k \epsilon_k^2 G_k = (i\omega + \mu - \Sigma)^2 G_{00} - (i\omega + \mu - \Sigma) \quad (3.11)$$

Using these expressions, we arrive at the final expression for \mathcal{G}_0 :

$$\mathcal{G}_0 = \Sigma + G_{00}^{-1} \quad (3.12)$$

We can therefore now rewrite the DMFT action in Eq. 3.3 in terms of local quantities of the original lattice. Therefore for any band dispersion(if necessary from DFT) and Coulomb interaction, we can calculate the lattice Green's function by mapping it to an impurity problem and then using the impurity Green's function to extract the Local Self energy which is plugged into the lattice problem. The solution to the problem is usually attempted iteratively, whereby one first chooses a self energy (zero is often a good starting point or we take a previously converged run for a similar system) and then the following steps are performed:

- The Local Green's function of the lattice is computed by summing over \mathbf{k}

$$G_{00}(i\omega_n) = \sum_k \frac{1}{i\omega - \epsilon_k + \mu - \Sigma(i\omega_n)} \quad (3.13)$$

- Compute \mathcal{G}_0 for the impurity solver by:

$$\mathcal{G}_0 = \Sigma + G_{00}^{-1} \quad (3.14)$$

- Solve the impurity problem using the effective action in Eq. 3.3 using an impurity solver to obtain G_{00} , the impurity Green's function
- Calculate the new self energy by using the Dyson Equation:

$$\Sigma = \mathcal{G}_0^{-1} - G_{00}^{-1} \quad (3.15)$$

- Go back to the first step and iterate till Σ is converged.

In practice we often think of the auxiliary impurity problem as an Anderson Impurity Model. Then we can rewrite the impurity Green's function in the form:

$$G_{00}(i\omega_n) = \frac{1}{i\omega_n - E_{imp} + \Delta - \Sigma} \quad (3.16)$$

where E_{imp} is the static energy level of the impurity states and Δ is the hybridization term which captures the dynamic hopping between the impurity and the bath. In this formulation, the DMFT self consistency condition is expressed as the twin assumptions-

$$\frac{1}{i\omega_n - E_{imp} + \Delta - \Sigma} = \sum_k \frac{1}{i\omega - \epsilon_k + \mu - \Sigma(i\omega_n)} \quad (3.17)$$

and that the impurity Σ is the same as the (purely local) lattice Σ .

Thus in this section we have outlined the algorithm behind DMFT. Note that the version we have outlined is what is known as single site DMFT, because we use a single impurity model to model our system. This method is of course limited by the fact that it considers only purely local site-based interactions. There are extensions to this scheme where we transform to a group of impurities, which gives rise to the "cluster-DMFT" algorithm. Cluster-DMFT has been at the forefront of a lot of research into systems where we have to take into account correlations beyond a single site and is one of the most powerful tools in computational condensed matter physics. However the computational cost grows quickly as one increases the size of the impurity cluster, making large clusters very computational taxing. We also mention here that there are other methods such DCA (Dynamical Cluster Approximation) which aim to patch together the self energy in k-space rather than in real

space and more natively preserves translational symmetry. For more details of such methods, the reader is directed to [58].

In conclusion, we can say that DMFT is one of the most powerful methods to simulate correlated systems. However the true power of the method is unlocked when we combine the power of DMFT to accurately describe the strongly correlated degrees of freedom with the tried and tested accuracy of DFT in simulating the weakly correlated bands. In the next chapter we shall outline how these two techniques can be combined to produce DFT+DMFT, the algorithm of choice for the simulations carried out in this dissertation.

Chapter 4

DFT+DMFT

In the previous two sections we have outlined the two major theoretical components which form the core of the simulation algorithm used in this thesis. In chapter 2 we outlined Density Functional Theory, which excels at simulating weakly correlated materials. In chapter 3 we looked at Dynamical Mean Field Theory (DMFT), which is well-suited to simulating more localized electrons in the d and f shells. As mentioned earlier, the development which has revolutionized the field of computational simulation of strongly correlated systems is the successful merger of these two techniques. This merger, usually known as "LDA+DMFT" or more correctly "DFT+DMFT" (because in general we can use other exchange correlation functionals than LDA) is what we shall look at in this chapter. However, before looking at how these two methods are merged, we shall reformulate DMFT in terms of functionals, which shall allow for a easier way to merge DFT with the DMFT method.

4.1 A functional Reformulation of DMFT

The formulation of any theory in a functional form is an elegant way to understand the basic nature of the equations governing the theory. The formulation usually involves defining an observable X and defining a functional $\Gamma[X]$ which has the following properties:

- $\Gamma[X]$ is extremized at the true value of X for the physical solution of the system
- At the extremum, $\Gamma[X]$ attains the value of the Free Energy F of the system.

When X is chosen to be the Green's function G of the system, the functional so defined is known as the Baym-Kadanoff functional. In this section we shall formulate the Baym-Kadanoff functional for a condensed matter system and see how DMFT can be thought of as a particular approximation to this functional.

We start with rewriting Eq 3.2 in terms of the Free Energy:

$$e^{-\beta F} = \int D[c^\dagger c] e^{-S} \quad (4.1)$$

Where the sum over sites and spins is assumed. We also know that the Green's function is given by

$$G(\mathbf{r}'\tau', \mathbf{r}\tau) = -\langle T_\tau c(\mathbf{r}'\tau') c^\dagger(\mathbf{r}\tau) \rangle \quad (4.2)$$

We now add a source term for the Green's function in the expression for the partition function :

$$e^{-\beta F} = \int D[c^\dagger c] \exp(-S - \int d\mathbf{r}' d\tau' d\mathbf{r} d\tau c(\mathbf{r}'\tau') J(\mathbf{r}'\tau', \mathbf{r}\tau) c^\dagger(\mathbf{r}\tau)) \quad (4.3)$$

such that

$$\frac{\delta F[J]}{\delta J} = G[J] \quad (4.4)$$

The physical Green's function is obtained by setting $J = 0$, and the actual Free energy is $F[J = 0] = F^{(0)}$.

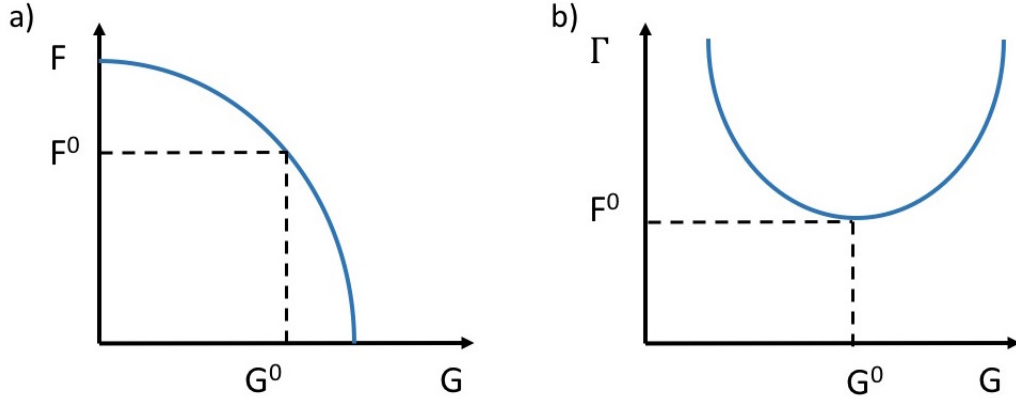


Figure 4.1: (a) The free energy $F = F[G]$, as a functional of the Greens function G , is originally generally not stationary at the physical Green's function G^0 of the system. (b) In contrast, the Baym-Kadanoff functional $\Gamma[G]$ obtained after performing the Legendre Transform becomes stationary at G^0 and has the value of the physical free energy $\Gamma[G^0] = F^0$ at its stationary point

We now perform a Legendre Transform to invert the functional to express the equation in terms of G rather than J , such that $J[G^{(0)}] = 0$ at the physical value of $G = G^{(0)}$. Therefore, we get a formulation in terms of $F[J[G]]$. The new functional obtained as a result of this is the Baym-Kadanoff functional(see Fig. 4.1), which has the form:

$$\Gamma[G] = F[J[G]] - \text{Tr} J[G]G \quad (4.5)$$

We can easily prove that

$$\left. \frac{\delta \Gamma[G]}{\delta G} \right|_{G^{(0)}} = J[G^{(0)}] = 0 \quad (4.6)$$

and at this point

$$\Gamma[J[G^{(0)}]] = F^{(0)} \quad (4.7)$$

Let us first define the Baym-Kadanoff functional for a non-interacting system. Now for any non-interacting system, the action is quadratic therefore the Free Energy can be written as $F = Tr(\log(-G))$. Therefore in the presence of the quadratic Source term, the Free energy F_0 for a non-interacting system is still:

$$F_0 = -Tr(\log(-G_0^{-1} + J)) \quad (4.8)$$

Where G_0 is the non-interacting Green's function. Now as defined above, by taking a derivative w.r.t J , we get $G[J] = 1/(G_0^{-1} - J)$, or equivalently for the non-interacting source term $J_0[G]$

$$J_0[G] = G_0^{-1} - G^{-1} \quad (4.9)$$

But we know from the Dyson equation that for the physical system, the R.H.S of the above equation when evaluated using the interacting Green's function G is equal to the Self Energy Σ of the system. This allows us to identify that $J_0[G] = \Sigma[G]$ for the non-interacting system. Therefore to sum up, for the non-interacting system we have formulated the Baym-Kadanoff functional $\Gamma_0[G]$ given by:

$$\Gamma_0[G] = Tr(\log(-G)) - Tr\Sigma[G]G \quad (4.10)$$

$$\Sigma[G] = G_0^{-1} - G^{-1} \quad (4.11)$$

In general, in the presence of interactions there will be corrections to this functional. We lump together all of these into one term denoted as $\Phi[G]$, also known as the Luttinger Ward Functional. So this new interacting Baym-Kadanoff functional is defined by:

$$\Gamma[G] = \Gamma_0[G] + \Phi[G] \quad (4.12)$$

By using the basic stationarity properties of $\Gamma[G]$, we get

$$\frac{\delta\Gamma[G]}{\delta G} = G^{-1} - G \frac{\delta\Sigma}{\delta G} - \Sigma[G] + \frac{\delta\Phi[G]}{\delta G} = 0 \quad (4.13)$$

where using Eq 4.11, we get

$$\frac{\delta\Phi[G]}{\delta G} = \Sigma[G] \quad (4.14)$$

Now we know from the formulation of the Dyson equation that the self energy contains all one particle irreducible diagrams. As the process of taking a functional derivative w.r.t G can be interpreted as cutting a Green's function line from a diagram, we see that $\Phi[G]$ must contain all

two-particle irreducible "skeleton" diagrams. For a diagrammatic representation of $\phi[G]$, refer to Fig 4.2

$$\begin{aligned} \Phi[G] = & \frac{1}{2} \text{ (loop) } - \text{ (loop with +) } + \frac{1}{2} \text{ (figure-eight) } + \\ & + \frac{1}{4} \text{ (two loops) } + \frac{1}{4} \text{ (circle with cross) } + \dots \end{aligned}$$

Figure 4.2: Diagrammatic representation of the full Luttinger-Ward functional containing all the two-particle irreducible skeleton diagrams

Within this framework, the DMFT can be formulated in an extremely elegant manner: We restrict $\Phi[G]$ to contain only local diagrams, as in all the Green's function propagators G are replaced by the local propagators G_{ii} , where i is the lattice site (for the diagrammatic representation, see Fig 4.3.

$$\Phi^{\text{DMFT}}[G_{ii}] = \frac{1}{2} \text{ (self-energy loop) } - \frac{1}{2} \text{ (self-energy loop with external line) } + \frac{1}{2} \text{ (self-energy loop with two external lines) } +$$

$$+ \frac{1}{4} \text{ (two self-energy loops) } + \frac{1}{4} \text{ (self-energy loop with two internal lines) } + \dots$$

Figure 4.3: Diagrammatic representation of the DMFT approximation to the Luttinger-Ward functional with all propagators being replaced by local propagators

Equivalently we can also claim the following result. :

$$\frac{\delta \Phi^{\text{DMFT}}[G]}{\delta G_{ij}} = \Sigma^{\text{DMFT}} \neq 0 \quad \text{iff} \quad i = j \quad (4.15)$$

where i, j are lattice sites. By using Eq. 4.14, we see that this implies that the self energy is purely local, which was the original DMFT approximation described in the last chapter. Note that that we have made no appeal to any infinite-dimensional limits. All we require for DMFT to work is that that dominant terms in Φ are the local diagrams. In practice we map the problem to an impurity problem by setting $\Gamma^{\text{DMFT}} = \Gamma_{\text{Imp}}$ and assume $G_{\text{local}}^{\text{DMFT}} = G_{\text{imp}}$, which ensures $\Sigma^{\text{DMFT}} = \Sigma_{\text{imp}}$.

4.2 Merging DFT with DMFT

Now that we have expressed the DMFT approximation in terms of the the Baym-Kadanoff functional, we can easily extend the framework to elucidate the DFT+DMFT algorithm. As we have seen, we can express the Free energy of any system as a functional of the Green's function as :

$$\Gamma[G] = \text{Tr}(\log(-G)) - \text{Tr}\Sigma[G]G + \Phi[G] \quad (4.16)$$

Where $\Gamma[G]$ and $\Phi[G]$ are the Baym-Kadanoff and Luttinger-Ward functional respectively. As we saw, the DMFT approximation is obtained by restricting $\Phi[G]$ to only the skeleton diagrams formed by the local Green's function. In order to include DFT within this framework, we need to make Γ a functional of both the Green's function and charge density ρ . We reformulate the equation as:

$$\Gamma[G, \rho] = \text{Tr}(\log(-G)) - \text{Tr}\Sigma[G]G + \Phi[G, \rho] \quad (4.17)$$

where the Luttinger ward functional has now been modified to :

$$\Phi[G, \rho] = \Phi_H[\rho] + \Phi_{XC}[\rho] + \Phi_{DMFT}[G] + \Phi_{DC}[G] \quad (4.18)$$

In the above equation the Luttinger-Ward functional has been decomposed into its Hartree, Exchange correlation, DMFT and "Double Counting" parts. An identical extremization operation as carried out earlier gives us the following relationships-

$$\Sigma - V_{DC} = \frac{\delta\Phi_{DMFT}[G]}{\delta G} - \frac{\delta\Phi_{DC}[G]}{\delta G} \quad (4.19)$$

Where the derivatives are only non-zero for the local Green's function, and-

$$V_H + V_{XC} = \frac{\delta\Phi_H[G]}{\delta\rho} - \frac{\delta\Phi_{XC}[G]}{\delta\rho} \quad (4.20)$$

and the charge density ρ is calculated by summing the Green's function over all frequencies. It is to be noted that the G is the total Green's function. It is only while taking the partial derivatives in Eq. 4.19 that we have terms only where $G = G_{loc}$. So we see that we can use the Hartree and Exchange correlation potentials computed with DFT and the self energy computed within DMFT and merge them in one framework. One of the issues that arises is that we have to take care of the double counting term , which contains the part of the DMFT self energy which is already accounted for in the DFT calculations. This issue has been one of the main talking points in DFT+DMFT research and different groups differ on how exactly to deal with it. [120] [28] . However, recently Haule [47] has proposed an efficient method to compute highly accurate values of V_{DC} .

Within this new formulation, we still use the impurity Green's function as our Local Green's function and the impurity self energy as the self energy of the system. The energy levels of the lattice system are expressed as Kohn sham eigen energies, and then the Green's function of the lattice system is built up by inserting the Self energy and Double counting corrections .

One of the main challenges involved in formulations of DFT+DMFT is how to go from the full-lattice system, for which we solve the DFT equations to obtain the Kohn-sham levels, to the correlated subspace, where we can apply the impurity models from which we obtain the DMFT self energy. In actual material calculations this would involve formulating a method to project our Green's function onto the d or f shell degrees of freedom. Different implementations of DFT+DMFT differ in their methods of identification of these correlated states. Moreover, they also have different methods to project the Green's function on to these localized states (The "Projection" scheme) and in how they embed the impurity self energy back into the lattice Green's function (The "Embedding" Scheme). Various Projection functions such as LMTO's, Nth-order Muffin Tin orbitals, as well as the highly popular Maximally Localized Wannier functions have been used to accomplish these

operations. However possibly the most accurate results are obtained by using quasi-localized atomic orbitals $|\phi^m\rangle$, which are defined as:

$$\langle \mathbf{r} | \phi_m^\mu \rangle = u_l(|r - R_\mu|) Y_{lm}(\widehat{r - R_\mu}) \quad (4.21)$$

where μ is a lattice site index, u_l are the radial solutions to the Schrodinger equation for angular momentum l and Y_{lm} are spherical harmonics. This formulation has the benefit that it allows us to solve the Dyson equation in real space where the correlations are actually very localized and hence the DMFT equations are valid, instead of transforming to an effective Hubbard Model by downfolding to a few Wannier orbitals, which are not typically localized completely on a particular correlated atom. Using this definition we can define the DMFT self consistency condition in the Kohn Sham space as :

$$\sum_{\mathbf{k}, ij} \langle \phi_m^\mu | \psi_{\mathbf{k}i}^{DFT} \rangle \left(i\omega + \mu - \epsilon_{\mathbf{k}} - \overline{\Sigma(\mathbf{k}, \omega)} \right)_{ij}^{-1} \langle \psi_{\mathbf{k}j}^{DFT} | \phi_{m'}^{\mu'} \rangle = \left(\frac{1}{i\omega - E_{imp}^\mu - \Sigma^\mu(i\omega) - \Delta^\mu(i\omega)} \right)_{mm'} \quad (4.22)$$

Where ψ_i^{DFT} are Kohn sham states, \mathbf{k} is a reciprocal state vector, and

$$\overline{\Sigma_{ij}(\mathbf{k}, \omega)} = \sum_{R_\mu} \langle \psi_{\mathbf{k}i}^{DFT} | \phi_m^{\mu'} \rangle (\Sigma_{mm'}^\mu(i\omega) - V_{DC}^\mu) \langle \phi_{m'}^\mu | \psi_{\mathbf{k}j}^{DFT} \rangle \quad (4.23)$$

is how the self energy is embedded into the Kohn-Sham space from the correlated subspace. It is to be noted that the Projection and embedding operators are the same basic operators (or the same tensors), but we just flip the indices to either go from Kohn Sham space to correlated space or vice versa.

With all these steps defined, we now present the entire charge self-consistent DFT+DMFT cycle as implemented in the WienDMFT [52] package, which implements DMFT on top of the Wien2k DFT package [19].

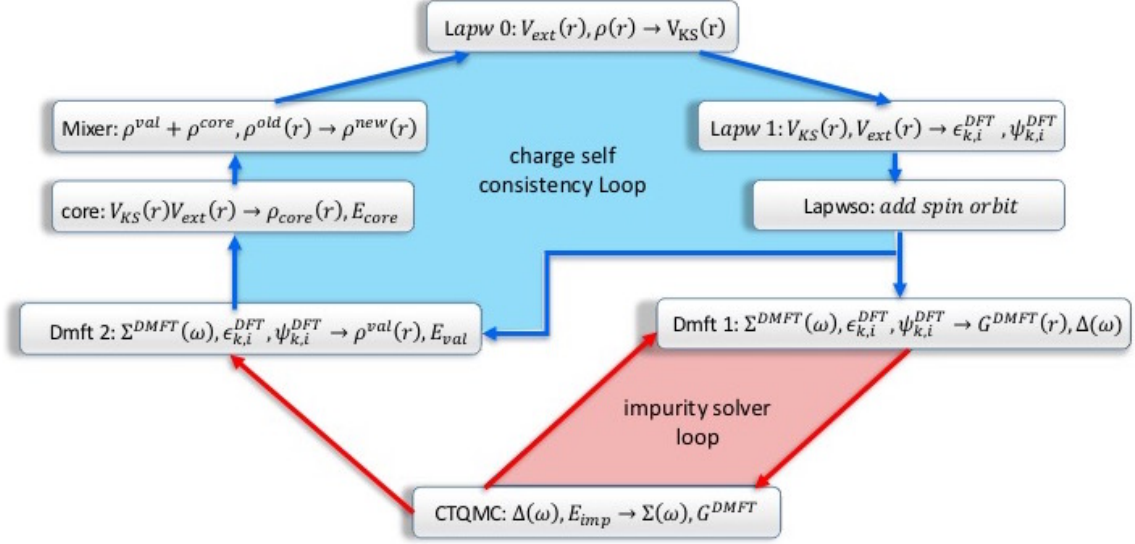


Figure 4.4: The DFT+DMFT loop as implemented in the WienDMFT Package

The subparts which make up the loop are-

- The charge self-consistency cycle
 - Lapw 0: Takes the electronic charge density $\rho(\mathbf{r})$ of the previous cycle (or an initial guess) and the external potential (V_{ext}) to calculate the Kohn Sham potential V_{KS} as defined in Eqn. 2.17
 - Lapw 1: Solves the eigenvalue problem using the calculated V_{KS} (and V_{ext}) to obtain the eigenfunctions and the eigenvalues of the Kohn Sham equations
 - Lapwso: Adds spin-orbit corrections if necessary
 - DMFT 2: We take the Kohn Sham eigenvalues and the current embedded self energy $\bar{\Sigma}$ as constructed by using the embedding operator defined in Eqn.4.23. We then solve the eigenvalue problem to obtain the eigenvalues and eigenfunctions by using

$$(-\nabla^2 + V_{KS} + \bar{\Sigma}(i\omega))|\psi_{k,i\omega_n,i}\rangle = \epsilon_{k,i\omega_n,i}^{DMFT}|\psi_{k,i\omega,i}\rangle \quad (4.24)$$

where i is the band index. We then calculate the chemical potential μ and new valence charge density ρ_{val} by using

$$N_{val} = T \sum_{i\omega_n,k,i} \frac{1}{i\omega_n + \mu - \epsilon_{k,i\omega_n,i}^{DMFT}} \quad (4.25)$$

$$\rho_{val} = \sum_{k,i,j} \psi_{k,i}^{DFT} T \sum_{i\omega_n} \left[\frac{1}{i\omega_n + \mu - \epsilon_k^{DFT} - \bar{\Sigma}(i\omega)} \right]_{ij} \psi_{k,j}^{*DFT} \quad (4.26)$$

- core: Adds in the core charge density
- mixer: Admixes the core and valence charge densities to obtain final electronic charge density $\rho^{new}(\mathbf{r})$
- The Impurity Solver Cycle
 - DMFT 1: Uses the Kohn Sham eigenvalues and eigenfunctions calculated in Lapw 1 above, along with the self energy Σ (or an initial guess) to calculate the local Green's Function, Impurity Levels and Hybridization functions. This is all done by projecting to the local degrees of freedom after constructing the projector as defined in Eqn.4.21 and then using Eqn. 4.22
 - Impurity Solver (CTQMC): In this step we take the Hybridization function and impurity levels calculated by DMFT 1 and use the CTQMC (or some other) impurity solver to get the impurity Green's Function G^{DMFT} and impurity self Energy $\Sigma(i\omega)$. The details of the CTQMC impurity solver are presented in the next chapter.

Note that the Lapw steps are taken directly from the Wien2k package, which is considered the gold standard for DFT calculations in the community. So we see that we now have a completely charge self-consistent method to factor in local electronic correlations in strongly correlated systems. This DFT+DMFT method is what we shall use in this thesis to study the properties of a variety of strongly correlated systems. A much more in-depth review of our implementation can be found in [53], and also on Prof. Haule's Web Page ¹where the reader may also find tutorials to familiarize oneself with the DFT+DMFT method developed by our group.

Note that in this chapter and Chapter 3, we have not mentioned the details of the fundamental part of the DMFT approximation which makes it a computationally tractable method to study strong correlation, which is the impurity solver. In the next chapter, we shall present details of one of the most advanced impurity solvers currently in use, the Continuous Time Quantum Monte Carlo (CTQMC) impurity solver which shall allow us to calculate the impurity Green's Function and Self Energy that is required by the DMFT self consistency conditions.

¹<http://www.http://hauleweb.rutgers.edu/tutorials>

Chapter 5

Continuous Time Quantum Monte Carlo Impurity Solver

5.1 Introduction

In the previous sections we have seen how DMFT becomes a powerful computational tool because it allows us to map the strongly correlated lattice problem to an impurity problem. For this purpose, the impurity model that is used is the Anderson Impurity Model[7]. The Hamiltonian for the model is given by:

$$H = \sum_{\mathbf{k}l\sigma} \epsilon_l(\mathbf{k}) a_{\mathbf{k}l}^{\dagger\sigma} a_{\mathbf{k}l}^{\sigma} + \sum_{\mathbf{k}l\sigma} [V_{l0}(\mathbf{k}) a_{\mathbf{k}l}^{\dagger\sigma} c_0^{\dagger\sigma} + h.c.] + U n_{0\uparrow} n_{0\downarrow} - \mu \sum_{\sigma} c_0^{\dagger\sigma} c_0^{\sigma} \quad (5.1)$$

where $a_{\mathbf{k}l}^{\dagger\sigma}$ are non-interacting conduction electrons at wave number \mathbf{k} that have a dispersion ϵ_l and which hybridize with the interacting impurity electrons $c_0^{\dagger\sigma}$ via the hybridization V_{l0} (Note that we have denoted the impurity site by 0)

One of the most involved and computationally challenging parts of the DMFT algorithm is finding the solution for the impurity Green's function for the Anderson Impurity model(AIM). There has been extensive research in this field and over the years there have been a whole range of analytical and computation methods that have been developed. Some of the important methods commonly in use are scaling methods [8], the numerical renormalization group[124], applications of the Bethe ansatz[9], slave bosons in the context of heavy fermion materials[24] and the Hirsch-Fye quantum Monte Carlo algorithm[61]. However in this paper we describe one of the most powerful computational methods available today Continuous Time Quantum Monte Carlo (CTQMC) and in particular its Hybridization expansion (CTQMC-HYB)[121] [43](An exhaustive introduction to the various CTQMC methods can be found in the review by Gull et al [41]). The advantage of this algorithm is its computational speed and its generality which allows us to sample very low temperatures, especially in the strongly interacting limit of Mott Insulators.

5.2 Details of the Algorithm

The CTQMC-HYB solver (hereafter referred to as CTQMC) relies on expanding the partition function of the AIM around the atomic limit. The ‘continuous time’ part in its name comes from the fact that we do not discretize the imaginary time integral into time slices unlike in Hirsch-Fye QMC algorithm. Neither do we introduce an auxiliary field of spins like we do in the Hirsch-Fye Algorithm.

We begin by separating the AIM Hamiltonian into three parts:

$$H_{imp} = U n_{0\uparrow} n_{0\downarrow} - \mu \sum_{\sigma} c_0^{\dagger\sigma} c_0^{\sigma} \quad (5.2)$$

$$H_{bath} = \sum_{\mathbf{k}p\sigma} \epsilon_p(k) a_{\mathbf{k}}^{\dagger\sigma} a_{\mathbf{k}}^{\sigma} \quad (5.3)$$

$$H_{hyb} = \sum_{\mathbf{k}l\sigma} [V_{l0}(\mathbf{k}) a_{\mathbf{k}l}^{\dagger\sigma} c_0^{\dagger\sigma} + h.c.] \quad (5.4)$$

From now on we shall suppress spin labels and assume implicit summation over spin indices. The quantity we are formally interested in is the partition function of the system which is given by:

$$Z = \int \mathcal{D}[a^{\dagger} a c^{\dagger} c] e^{-S_{imp} - S_{bath} - S_{hyb}} \quad (5.5)$$

In order to express the partition function as terms of the finite impurity degrees of freedom, we first integrate out the bath electrons which gives us

$$Z = Z_{bath} \cdot Z_{imp} \quad (5.6)$$

$$Z_{bath} = \prod_{\nu \mathbf{k} p} \beta(-i\omega_{\nu} + \epsilon_p(\mathbf{k})) \quad (5.7)$$

$$Z_{imp} = \int \mathcal{D}[c^{\dagger} c] e^{-S_{eff}} \quad (5.8)$$

The Z_{bath} terms just includes an irrelevant constant to the expression which we shall ignore. The effective action contains in it all the impurity physics as well as the effect of the retarded interaction of the impurity electrons with the bath and is given by:

$$S_{eff} = S_{imp} + \int_0^{\beta} d\tau \int_0^{\beta} d\tau' c^{\dagger}(\tau) \Delta(\tau - \tau') c(\tau') \quad (5.9)$$

where we denote the hybridization function, as before by

$$\Delta = \sum_{\mathbf{k}p} \frac{V_{0p}^*(\mathbf{k}) V_{0p}(\mathbf{k})}{i\omega + \mu - \epsilon_p(\mathbf{k})} \quad (5.10)$$

The hybridization function encodes in it all the interaction with the bath at different energies. We are pretty much free to choose any convenient Hybridization function like a semi-circle or a lorentzian.

Performing a Taylor expansion of the Hybridization term in the impurity action over the Grassman variables, we get:

$$Z_{imp} = \sum_{k=0}^{\infty} \frac{1}{k!} \int \mathcal{D}[c^\dagger c] e^{-S_{imp}} (-\Delta S)^k \quad (5.11)$$

$$= Z_0 \sum_{k=0}^{\infty} \frac{1}{k!} \int_0^\beta d\tau_1 \cdots d\tau_k \int_0^\beta d\tau'_1 \cdots d\tau'_k \langle T_\tau c(\tau'_1) c^\dagger(\tau_1) \cdots c(\tau'_k) c^\dagger(\tau_k) \rangle_0 \cdot \Delta(\tau_1 - \tau'_1) \cdots \Delta(\tau_k - \tau'_k) \quad (5.12)$$

In this expression we have absorbed the minus sign in ΔS by reordering $-c^\dagger \Delta c$ as $cc^\dagger \Delta$. The normalization Z_0 denotes the impurity Partition function and the averaging $\langle \cdots \rangle_0$ denotes the average over the impurity Green's function.

The current formulation of the integrands in the Hybridization expansion can be both positive and negative. This would lead to inefficient Monte Carlo evaluation because of the infamous sign problem. In order to avoid this, we group together all terms at the perturbation order k in the form of a determinant. To see this we note that at $k=2$ we get a contribution

$$\frac{1}{2!} \int_0^\beta d\tau_1 d\tau_2 \int_0^\beta d\tau'_1 d\tau'_2 \langle T_\tau c(\tau'_1) c^\dagger(\tau_1) c(\tau'_2) c^\dagger(\tau_2) \rangle_0 \cdot \Delta(\tau_1 - \tau'_1) \Delta(\tau_2 - \tau'_2) \quad (5.13)$$

Considering just the unprimed integrals, the idea is to convert the two wedges in the integration times ($W = \tau_1, \tau_2 : \tau_1 > \tau_2$ and vice versa) into just one wedge. However when we do this, the integrand becomes a sum of two terms. When we swap the times in the time order impurity impurity trace, we get a minus sign:

$$\langle T_\tau c(\tau'_1) c^\dagger(\tau'_2) c(\tau'_2) c^\dagger(\tau'_1) \rangle_0 = -\langle T_\tau c(\tau'_1) c^\dagger(\tau'_1) c(\tau'_2) c^\dagger(\tau'_2) \rangle_0 \quad (5.14)$$

This together with the swap in the arguments of the Hybridization function allows us to express the contribution as :

$$\frac{1}{2!} \int_0^\beta d\tau_1 \int_{\tau_1}^\beta d\tau_2 \int_0^\beta d\tau'_1 \int_0^\beta d\tau'_2 \langle T_\tau c(\tau'_1) c^\dagger(\tau'_1) c(\tau'_2) c^\dagger(\tau'_2) \rangle_0 \quad (5.15)$$

$$\cdot \det \begin{pmatrix} \Delta(\tau_1 - \tau'_1) & \Delta(\tau_1 - \tau'_2) \\ \Delta(\tau_2 - \tau'_1) & \Delta(\tau_2 - \tau'_2) \end{pmatrix} \quad (5.16)$$

Finally we absorb the $1/2!$ term by converting the the integral over the primed variables to one over just a single wedge and recognizing that when when we swap τ'_1 and τ'_2 we get a minus sign both in the impurity trace and the determinant of Hybridization function. Therefore our formula at second order is

$$\int_W d\tau_1 d\tau_2 \int_W d\tau'_1 d\tau'_2 \langle T_\tau c(\tau'_1) c^\dagger(\tau'_1) c(\tau'_2) c^\dagger(\tau'_2) \rangle_0 \cdot \det(\Delta(\tau_1, \tau_2)) \quad (5.17)$$

So we can express the full partition function as

$$Z_{imp} = Z_0 \sum_{k=0}^{\infty} \int_W d\tau_1 \cdots d\tau_k \int_W d\tau'_1 \cdots d\tau'_k Z(\tau_1 \cdots \tau_k, \tau'_1 \cdots \tau'_k) \quad (5.18)$$

where the integration is just over the single wedge in imaginary time $W=(\tau_1 \cdots \tau_k : \tau_1 < \cdots \tau_k)$ and the integrand is:

$$Z(\tau_1 \cdots \tau_k, \tau'_1 \cdots \tau'_k) = \langle T_{\tau} c(\tau_1) c^{\dagger}(\tau_1) \cdots c(\tau_k) c^{\dagger}(\tau_k) \rangle_0 \cdot \det(\Delta(\tau_i, \tau_j)) \quad (5.19)$$

We then apply Monte Carlo sampling to sample the integrand. The space we are sampling here is the collection of $2k$ dimensional integral phase spaces. A Monte Carlo configuration here is a particular collection of $2k$ times for the creation and annihilation operators $D_k = \tau_1, \tau_2 \dots \tau_k, \tau'_1, \tau'_2 \dots \tau'_k$. A step in the Monte-Carlo process corresponds to either adding or removing 2 kinks in the interval between 0 and β . By doing an analysis of the relative probabilities of adding or subtracting a pair of operators, we get that

$$A(\mathcal{D}_k \rightarrow \mathcal{D}_{k+1}) = \frac{\beta^2}{(k+1)^2} \min \left(1, \frac{Z(\mathcal{D}_{k+1})}{Z(\mathcal{D}_k)} \right) \quad (5.20)$$

$$A(\mathcal{D}_{k+1} \rightarrow \mathcal{D}_k) = \frac{k^2}{\beta^2} \min \left(1, \frac{Z(\mathcal{D}_{k-1})}{Z(\mathcal{D}_k)} \right) \quad (5.21)$$

where $Z(\mathcal{D}_k)$ is the contribution from the integrand in Eq. 31 for the hybridization expansion and $A(B \rightarrow C)$ indicates the acceptance probability of a move from configuration B to C.

In order to evaluate the Impurity trace, we first explicitly time-order the various creation and annihilation operators (denoted here by F^i).

$$\langle T_{\tau} F_1(\tau_1) \cdots F_k(\tau_k) \rangle_0 = \text{sgn} \mathcal{P} \cdot \langle F_{\mathcal{P}(1)}(\tau_{\mathcal{P}(1)}) \cdots F_{\mathcal{P}(k)}(\tau_{\mathcal{P}(k)}) \rangle_0 \quad (5.22)$$

Where \mathcal{P} denotes the permutation required for time ordering the operators. Now since we have a finite number of degrees of freedom in the impurity, we express the operators in some basis and take the trace. For example we could expand in the basis of Energy Eigenstates $|n\rangle$ and we would get :

$$\langle F_k(\tau_k) \cdots F_1(\tau_1) \rangle_0 = \quad (5.23)$$

$$\sum_{n_1 \cdots n_k} \left[e^{-E_{n_k}(\beta - \tau_k)} F_{n_k, n_{k-1}}^k e^{-E_{n_{k-1}}(\tau_k - \tau_{k-1})} \cdots e^{-E_{n_1}(\tau_2 - \tau_1)} F_{n_1, n_0}^1 e^{-E_{n_0}(\tau_1)} \right] \quad (5.24)$$

where the matrix elements are denoted by $F_{mn}^i = \langle m | F^i | n \rangle$. In practice, the evaluation is made faster by constructing superstates of the atomic states on the basis of conserved quantities and only considering matrix elements for transitions between the members of a particular superstate.

Thus, by this method we can effectively calculate the partition function of the Anderson Impurity model effectively. Note that although we have only used a single impurity and hybridization

bath, the method is easily generalizable to an arbitrary number of baths by simple extensions [43]. Once we know the Partition function for AIM, we can easily calculate the Green's function by noting that the evaluation of the Green's function

$$G(\tau_1 - \tau_2) = -\langle T_\tau c(\tau_1) c^\dagger(\tau_2) \rangle \quad (5.25)$$

is similar to evaluating the impurity trace but with two extra kinks added. So we see how CTQMC gives us an efficient computational way of solving the AIM and getting the impurity Green's function. It not only deals with the notorious fermionic sign problem but due to lack of time discretization, allows us to reach very low temperatures (at least an order of magnitude lower than the Hirsch-Fye Procedure). Thus with the Green's function from this method we can, using the DMFT loop described above, calculate the local Green's function of the lattice problem and investigate the properties of our system. Note that the description given above is one of only a class of general CTQMC methods which are suitable in different interaction strength regimes. As noted earlier, an exhaustive review can be found in [41], while much more details of our particular implementation of the DFT+DMFT loop can be found in [53].

Part II

Applications

Chapter 6

Calculation of Magnetic Spectral function and Dynamic Magnetic Susceptibility for f-shell materials

In this section we shall present calculations of the magnetic properties of f-shell materials. As mentioned earlier, materials with incompletely filled f-shells exhibit strong correlations which make them particularly challenging to understand from a theoretical standpoint. DFT+DMFT is one of the very few methods capable of simulating these systems [109, 83]. Here we concentrate on studies of the magnetic properties of such elements. Our ultimate aim shall be to calculate the Magnetic Spectral Function $S(q, \omega)$, which shall give us complete information about all the magnetic excitations of the system. In order to calculate this quantity, we shall need to calculate the Magnetic form factor $\vec{F}(q)$ and the dynamic magnetic susceptibility $\chi(\omega)$ of these materials. Using these tools, we shall make important claims about two important problems in condensed matter physics

- The volume collapse (or the $\alpha - \gamma$) transition in Cerium
- The valence fluctuating ground state of δ -Plutonium which explains its "missing magnetism"

In the first three sections of this chapter, we describe in some detail the calculation procedure for the various components of $S(q, \omega)$. After that we shall go on to details of the calculations for Cerium and Plutonium respectively.

6.1 Details of theory and calculation techniques

6.1.1 The Magnetic Spectral Function $S(q, \omega)$

The magnetic spectral function $S(q, \omega)$ gives us information about the spectrum of all magnetic excitations of a material. This quantity is especially useful as we can use neutron scattering to determine $S(q, \omega)$. Within the single ion approximation (which amounts to the approximation that the excitations are mostly limited to the ground state multiplet and that we can approximate the magnetic susceptibility as a fairly local quantity which does not fluctuate over the first Brillouin

zone), we can separate out the q and ω dependence of the quantity and express the quantity as:

$$S(q, \omega) = |\vec{F}_M(q)|^2 S(\omega) \quad (6.1)$$

where

$$S(\omega) = \frac{1}{2} \frac{1}{1 - e^{-\beta \hbar \omega}} \text{Im} \chi_{loc}(\omega) \quad (6.2)$$

is the energy dependent magnetic structure factor dependent on the imaginary part of the local dynamic magnetic susceptibility $\chi_{loc}(\omega)$ and

$$\vec{F}_M(q) = \frac{-1}{2\mu_B} \langle M_T(q) \rangle \quad (6.3)$$

is the magnetic form factor which captures the q -dependence of the spectral function. Note that in the equation above $M_T(q)$ is the Fourier transform of the component of the magnetic moment of the material that is transverse to the scattering vector \vec{q} of the incoming neutrons.

6.1.2 The Local dynamic susceptibility $\chi_{loc}(\omega)$

The magnetic susceptibility $\chi(q, \omega)$ of a material encodes information about the magnetic fluctuations of a system. In systems with open f-shells, due to the extremely localized nature of the f-shell electrons which contain the magnetic moment, we can effectively consider the susceptibility to be equivalent to its local component $\chi_{loc}(\omega)$. We will be especially interested in the imaginary part of this quantity, whose peaks give us the energy scales for magnetic dissipation in the system which, as we shall see later, provides us with important insights regarding the physics of these compounds.

Within our DFT+DMFT scheme, we approximate χ_{loc} of the lattice system to be equal to the χ_{Imp} of the impurity. The CTQMC impurity solver gives us direct access to χ_{Imp} (or more accurately its z-z component) because we can calculate:

$$\chi_{zz}(i\omega) = \int_0^\beta e^{i\omega\tau} \langle M_z(\tau) M_z(0) \rangle \quad (6.4)$$

directly by Monte Carlo sampling as long as the Magnetic Moment M_z is a good quantum number for the impurity. Note that for f-shell materials there is significant spin-orbit coupling which means that instead of S_z , we use J_z as our observable as it is good quantum number.

However CTQMC gives us $\chi_{loc}(i\omega)$ on the imaginary (matsubara axis). In order to get $\chi_{loc}(\omega)$, we have to perform analytic continuation to the real frequency axis. This is accomplished using the Maximum Entropy analytic continuation method [69]. Further, in order to check the correctness of the analytic continuation algorithm we use the following well known sum rule for M_z .

$$\frac{1}{\pi} \int d(\omega) n(\omega) (\text{Im} \chi(\omega)) = \langle M_z^2 \rangle \quad (6.5)$$

where $n(\omega)$ is the Bose-Einstein distribution function. This is useful because we can calculate $\langle M_z^2 \rangle$ directly from the Monte Carlo probabilities of the various impurity states. Therefore the integral gives us a way to check the veracity of the analytic continuation. It is to be noted that CTQMC calculations for elements with a large number of f-shell electrons can be extremely hard to converge. For example, the calculations for δ -Pu required the use of roughly 1 Million computer hours on the Titan supercomputer at ORNL, although it is to be noted that $\chi_{loc}(\omega)$ seems to converge quicker than the self energy for these simulations.

6.1.3 The Magnetic form factor $\vec{F}_M(\vec{q})$

We shall now give details of the Magnetic form factor calculation. The formula for the neutron form factor is given by

$$\vec{F}_M(\vec{q}) = \frac{-1}{2\mu_B} \langle M_T(\vec{q}) \rangle \quad (6.6)$$

where $M_T(q) = M_T^{spin}(q) + M_T^{orb}(q)$ is the transverse component of the magnetization density (relative to the incident neutrons) and \vec{q} is the scattering wave vector of the incident neutrons. This expression can also be written as:

$$\vec{F}_M(\vec{q}) = \frac{-1}{2\mu_B} \hat{q} \times \int_{unit\ cell} (\langle M(\vec{r}) \rangle e^{-i\vec{q} \cdot \vec{r}} d\vec{r} \times \hat{q}) \quad (6.7)$$

We can express this magnetization density (after making the gauge choice for the transverse current density that $\vec{J}(\vec{r}) = c\nabla \times M_T(\vec{r})$) in terms of the current densities as:

$$M_T(q) = -\frac{i}{c} \vec{q} \times \frac{\vec{J}(\vec{q})}{q^2} \quad (6.8)$$

where:

$$\vec{J}_{orb}(\vec{q}) = \frac{e}{2m} \sum_j \vec{p}_j e^{-i\vec{q} \cdot \vec{r}} + e^{-i\vec{q} \cdot \vec{r}} \vec{p}_j \quad (6.9)$$

and

$$\vec{J}_{spin}(\vec{q}) = -2i\mu_B c \vec{q} \times \sum_j \vec{s}_j e^{-i\vec{q} \cdot \vec{r}} \quad (6.10)$$

are the orbital and spin current densities ¹, which leads us to:

$$\vec{F}_M(\vec{q}) = \left\langle \sum_j \left\{ \hat{q} \times (\vec{s}_j \times \hat{q}) + \frac{i}{\hbar q} (\vec{p}_j \times \hat{q}) \right\} e^{-i\vec{q} \cdot \vec{r}_j} \right\rangle_{unit\ cell} \quad (6.13)$$

In the calculations carried out in this section for Cerium and Plutonium, we only have one atom per unit cell. However in general we shall have multiple atoms in the unit cell (which might be enlarged due to magnetic order). So in general we can decompose the exponential as

$$e^{-i\vec{q} \cdot \vec{r}_j} = e^{-i\vec{q} \cdot (\vec{R}_j + \vec{r})} \quad (6.14)$$

where \vec{R}_j is the vector to the center of the j^{th} magnetized atom and \vec{r} is the vector from the center to a point within the atomic sphere centered around the magnetized atom. We now resort to the traditional dipole approximation for ease of computation and interpretation. In order to do so, we first express the exponential in 6.13 as:

$$e^{-i\vec{q} \cdot \vec{r}} = \sum_{k=0}^{\infty} (2k+1)(-i)^k j_k(qr) P_k(\hat{q} \cdot \hat{r}) \quad (6.15)$$

Now from traditional selection rules for angular momentum, we can derive that for the orbital angular momentum part, we only need to keep the odd terms in the expansion, while for the spin part we need the even terms. Further we also know that for Bessel functions, we can use the identity

$$j_k(x) = \frac{x}{2k+1} (j_{k-1}(x) + j_{k+1}(x)) \quad (6.16)$$

to recast odd Bessel functions in terms of even Bessel functions. Finally under the dipole approximation, we only retain terms up to dipole order in the expansion. Under these assumptions, we can derive

$$\vec{F}_M(q) = \left\langle \sum_j e^{i\vec{q} \cdot \vec{R}_j} \left(\hat{q} \times (\vec{s}_j \times \hat{q}) j_0(qr) + e^{i\vec{q} \cdot \vec{R}_j} \left(\hat{q} \times (\vec{l}_j \times \hat{q}) \right) \{j_0(qr) + j_2(qr)\} \right) \right\rangle_{unit\ cell} \quad (6.17)$$

Now within our implementation LDA+DMFT we use the LAPW basis set (a comprehensive review of which can be found in [111]) so within the atomic spheres we can write the Kohn-Sham states as solutions to atomic-like Schrodinger Equations:

$$\psi_{k\sigma}(\vec{R}) = \sum_{\vec{L}\kappa m} A_{i\vec{L}\sigma}^{\kappa}(\vec{k}) u_{\vec{L}}^{\kappa}(R) Y_{\vec{L}}^m(\hat{R}) \quad (6.18)$$

¹These two equations come from the Fourier transforms of

$$\vec{J}_{orb}(\vec{r}) = \frac{e}{2m} \sum_j \vec{p}_j \delta(\vec{r} - \vec{r}_j) + \delta(\vec{r} - \vec{r}_j) \vec{p}_j \quad (6.11)$$

and

$$\vec{J}_{spin}(\vec{r}) = -2\mu_B c \vec{\nabla} \times \sum_j \vec{s}_j \delta(\vec{r} - \vec{r}_j) \quad (6.12)$$

(here $\kappa = 0$ corresponds to the solution of the Schrodinger equation u_l for a given linearization energy, $\kappa = 1$ corresponds to the energy derivative, and higher values correspond to the different localized orbitals) while $Y_m^{\mathcal{L}}$ represent the spherical harmonics

Moreover within the DMFT framework, any single-particle operator can be expressed as:

$$\langle O \rangle = Tr \left\langle \hat{n}^{DMFT} \hat{O} \right\rangle \quad (6.19)$$

where the density matrix is defined by:

$$\hat{n}_{\alpha\beta}^{DMFT} = T \sum_{\iota\omega} \left(\frac{1}{\iota\omega + \mu - \epsilon_k - \bar{\Sigma}} \right)_{\alpha\beta} \quad (6.20)$$

where $\bar{\Sigma}$ is the self energy after it has been embedded into the Kohn Sham space following the procedure developed in Chapter 4 in 4.23.

Now we can write the expression for the form factor as:

$$\vec{F}_M(q) = \sum_{\mathcal{L}' \kappa' \sigma' \mathcal{L} \kappa \sigma} \hat{n}_{\mathcal{L}' \kappa' \sigma' \mathcal{L} \kappa \sigma}^{DMFT} \langle \mathcal{L}' \kappa' \sigma' | \sum_j e^{-i\vec{q} \cdot \vec{R}_j} \hat{q} \times (l_z^j \{j_0(qr) + j_2(qr)\} + s_z^j j_0(qr) | \mathcal{L} \kappa \sigma) \rangle \times \hat{q} \quad (6.21)$$

where

$$\hat{n}_{\mathcal{L}' \kappa' \sigma' \mathcal{L} \kappa \sigma}^{DMFT} = \sum_{\alpha\beta} n_{\alpha\beta}^{DMFT} A_{\alpha\mathcal{L}' \sigma'}^{*\kappa'}(\vec{k}) A_{\beta\mathcal{L} \sigma}^{\kappa}(\vec{k}) \quad (6.22)$$

There explicitly writing out the expression for the form factor we get:

$$\begin{aligned} \vec{F}_M(q) = & \sum_j e^{-i\vec{q} \cdot \vec{R}_j} \sum_{k\alpha\beta \mathcal{L}' \kappa' \mathcal{L} \kappa} n_{\alpha\beta}^{DMFT} A_{\alpha\mathcal{L}' \sigma'}^{*\kappa'}(\vec{k}) A_{\beta\mathcal{L} \sigma}^{\kappa}(\vec{k}) \int d\vec{r} u_{\mathcal{L}'}^{*\kappa'}(r) u_{\mathcal{L}}^{\kappa}(r) \\ & \times \hat{q} \times \left(\langle \mathcal{L}' | l_z^j | \mathcal{L} \rangle \{j_0(qr) + j_2(qr)\} + \sum_{\sigma' \sigma} \langle \sigma' | s_z^j | \sigma \rangle j_0(qr) \right) \times \hat{q} \end{aligned} \quad (6.23)$$

where $|\mathcal{L} \rangle$ denotes the Y_L^m part of the basis and $|\sigma \rangle$ denotes the spin state. The next approximation which is applied is with regard to the experimental setup which again simplifies the formula. We assume (following the most common experimental setup) that an external B field has resulted in the complete polarization of \vec{l} and \vec{s} in the \hat{z} direction so it is sufficient to only calculate l_z and s_z and also that the scattering vector \vec{q} is perpendicular to the to this polarization axis.

Under these assumptions, the form factor (which we no longer treat as a vector) simplifies to:

$$\begin{aligned} F_M(q) = & \sum_j e^{-i\vec{q} \cdot \vec{R}_j} \sum_{k\alpha\beta \mathcal{L}' \kappa' \mathcal{L} \kappa} n_{\alpha\beta}^{DMFT} A_{\alpha\mathcal{L}' \sigma'}^{*\kappa'}(\vec{k}) A_{\beta\mathcal{L} \sigma}^{\kappa}(\vec{k}) \int d\vec{r} u_{\mathcal{L}'}^{*\kappa'}(r) u_{\mathcal{L}}^{\kappa}(r) \\ & \times \left(\langle \mathcal{L}' | l_z^j | \mathcal{L} \rangle \{j_0(qr) + j_2(qr)\} + \sum_{\sigma' \sigma} \langle \sigma' | s_z^j | \sigma \rangle j_0(qr) \right) \end{aligned} \quad (6.24)$$

This is the final expression we use to calculate our form factor within DMFT.

It is also to be noted that a common tool used to analyze the form factor within the dipole approximation involves recasting it into the form.

$$F_M = \frac{M}{2\mu_B} (\langle j_0 \rangle + C_2 \langle j_0 + j_2 \rangle) \quad (6.25)$$

where $\langle j_k \rangle$ is the spatial average of the spherical Bessel function $J_k(qr)$ over the radial solution of the LAPW basis state wave function $u(r)$ as defined in 6.24, $M = -(\vec{M}_S + \vec{M}_L)$ is the (negative) total (spin plus orbital) magnetic moment, and $C_2 = \vec{M}_L/(\vec{M}_S + \vec{M}_L)$.

An important implementation detail is that, as stated above, we compute the form factor in the presence of a magnetic field which results in the polarization of the magnetic moment of the atom. It is important to note that the B-field is included at the level of the impurity. We also assume during our calculation of the form factor that the orbital and spin angular momenta are completely aligned in the direction of the B-field. To ensure that this is the case, we need to choose a large B-field. Also, the required B-field should become higher with increasing temperature as we need to ensure that the effect of the Zeeman term is high enough to negate thermal fluctuations which might end up de-aligning the spin/orbital moments. After a large enough B-field has been chosen, the effect of the B-field is included in the impurity solver by adding a term to the Hamiltonian:

$$H_B = H - \mu_B B(l_z + 2s_z) \quad (6.26)$$

where the old assumption that the B-field is in the \hat{z} direction is used again. Now, in the presence of spin-orbit coupling this might lead to a non-diagonal H_B . If the off-diagonal terms can be safely ignored (as is the case in Cerium because the $j = \frac{7}{2}$ states can be assumed to be unoccupied) then we can still use CTQMC as our impurity solver and can include the effect of the B-field as a shift in the double counting energy (E_{DC}). However in δ -Pu we cannot afford such luxuries and we really do have to take the entire non-diagonal Hamiltonian with transitions between the $j = \frac{7}{2}$ and $j = \frac{5}{2}$ multiplets as allowed by Hamiltonian. In that case, we can no longer use CTQMC as it would have a horrible sign problem with off-diagonal terms, so we resort to other impurity solvers like NCA and OCA [53]. These solvers would give us the whole (off-diagonal included) self energy and Green's functions which we can then use in Eq 6.24.

Note that in either case, the calculation of the additional piece of the Hamiltonian would involve the use of Clebsch Gordon Coefficients as we have to go from the j, m_j, l, s basis to the l, m_l, s, m_s basis to evaluate the $(l + 2s)$ term

This concludes our review of the theoretical steps required to calculate $S(q, \omega)$. It is very important to note that this method is exceedingly accurate only when we can accurately approximate

$\chi(q, \omega)$ to be a truly local quantity as then the factorization into $\vec{F}_M^2(q)Im\chi_{loc}(\omega)$ is valid. In case such an approximation cannot be made, as in the case of most non f-shell systems, we have to resort to a true calculation of $\chi(q, \omega)$ using the Bethe Saltpeter equation.:

$$\chi^{-1}(q, \omega) = \chi_0^{-1}(q, \omega) - \Gamma \quad (6.27)$$

where $\chi_0^{-1}(q, \omega)$ is the "Bubble" Polarization contribution which is a convolution of the Interacting Green's function, given by:

$$\chi_0^{-1}(q, \omega) = -T \sum_{Q, \Omega} G(Q, \Omega) G(q + Q, \omega + \Omega) \quad (6.28)$$

and Γ is the irreducible two particle vertex. Our current implementation of DMFT allows to calculate the two particle vertex on the matsubara axis, however analytic continuation of Γ is a challenging task. However some attempts have been made to use this form to get a more accurate description of response functions, including in the next section where we study the volume collapse transition in Cerium, as well as by Yin et.al[126].

6.2 Applications to Real Materials

6.2.1 Analyzing the Volume Collapse transition in Cerium

Introduction

In this section we shall present the study performed by us on the volume collapse transition in Cerium, which shall follow very closely the work published in [21], with very minor additions. The physical mechanism driving the α - γ phase transition has puzzled physicists for many years [76]. Similar to other elements, the temperature versus pressure phase diagram of cerium shows multiple structural transitions, where the symmetry of the structure changes across the phase transition (see Fig. 6.1). The α - γ transition is exceptional because it is isostructural, i.e. the atoms retain their ordering in an *fcc* structure while the volume collapses by 15% from γ to α phase upon increasing pressure (see Fig. 6.2). Moreover, the α - γ transition is accompanied by a dramatic change in the magnetic susceptibility: the α phase shows Pauli-like susceptibility, while the γ phase has Curie-like susceptibility. Therefore, most of the theoretical work has focused on the hypothesis that electronic effects are responsible for the transition.

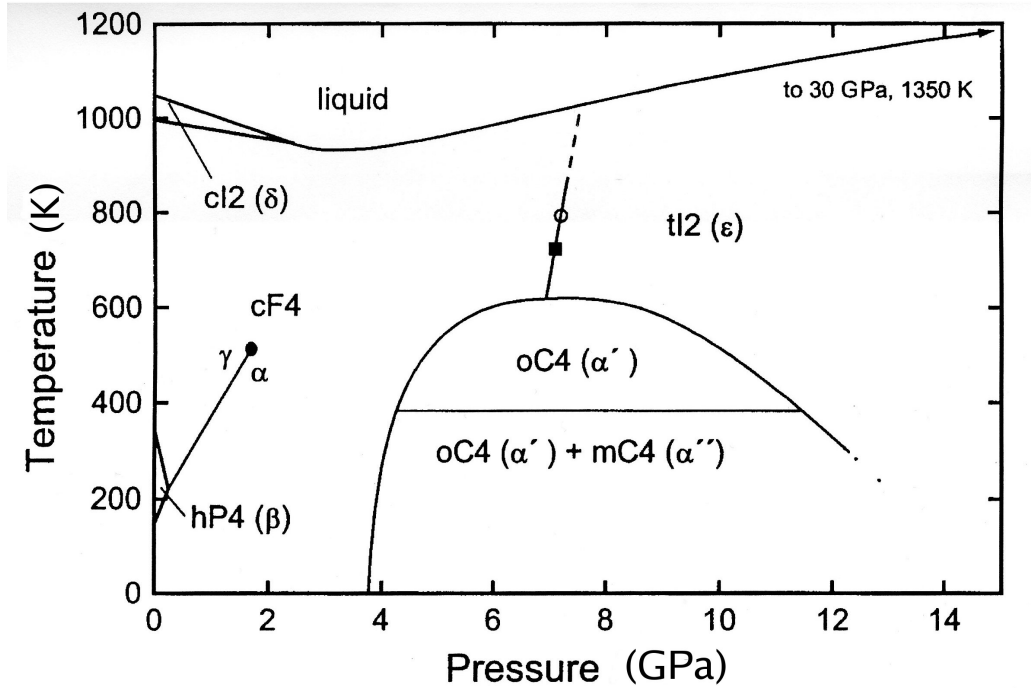


Figure 6.1: The Temperature vs Pressure Phase diagram for Cerium showing the multiple phases of the material. We shall be concentrating on the volume collapse transition between α -Ce and γ -Ce

Numerous theoretical models were proposed to explain the isostructural transition in Ce. For

example, in the promotional model [25], the $4f$ electrons are localized in the γ phase, and are promoted to the spd conduction band in the α phase. However photoemission spectroscopy shows little change in the number of the conduction electrons at the transition. Johansson proposed [70] that the $\alpha - \gamma$ transition is an example of a Mott transition. Here the $4f$ electrons undergo a Mott transition, from a non-bonding localized state in the γ phase to a narrow $4f$ band in the α phase, which participates in bonding. The spd electrons remain bystanders during the transition. Upon increasing pressure, a $4f$ localization-delocalization transition occurs with a subsequent loss of moment and decrease of volume. In this model, the $4f$ electron number remains almost unchanged with pressure, so this feature is consistent with photoemission results. A different scenario was proposed by Lavagna et al. [81] and Allen [3], dubbed the Kondo volume collapse theory. Here the spd electrons are not bystanders as in the Mott scenario. Instead the transition is connected to the change in the effective hybridization (and thus the Kondo scale) of the spd electrons with the $4f$ electrons and so there is a decrease in volume due to the increase of the Kondo temperature T_K .

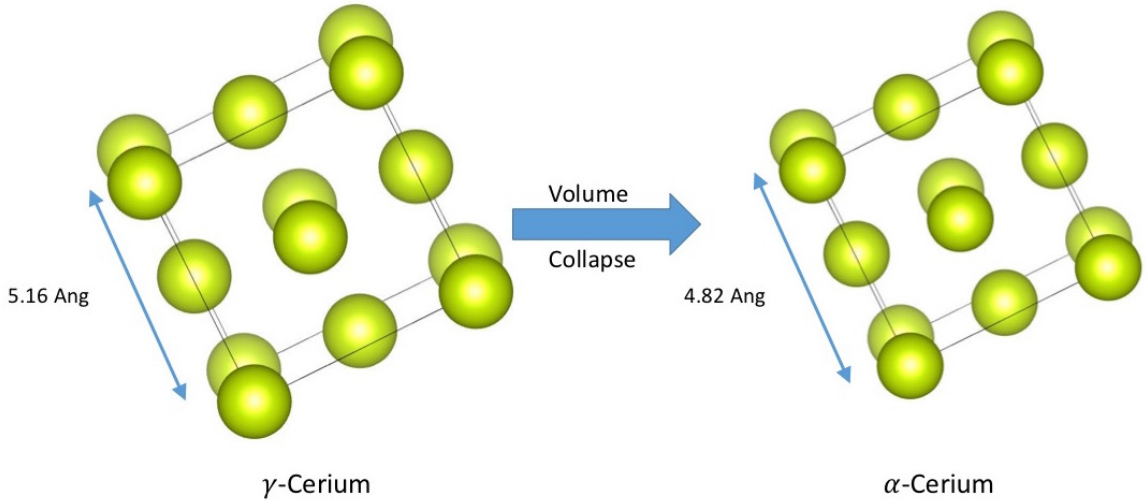


Figure 6.2: Diagram showing the Volume collapse transition between α -Ce and γ -Ce, where the FCC lattice is retained but unit cell volume decreases

DFT+DMFT allows one to consider structural effects, electronic effects and the physics of strong correlations from first-principles. It brings the physics of f-electron delocalization and f- spd hybridization into a unified framework. As a result of many studies over several years, different aspects of the $\alpha - \gamma$ transition have been considered, including changes in the density of states [130, 59, 86], in the optical conductivity [50], and in the thermodynamic properties [4].

From the theoretical point of view, the magnetic properties of the volume collapse transition

have not been adequately addressed so far. Here we shall revisit the $\alpha - \gamma$ transition from the point of view of magnetic properties by computing the magnetic form factor $F_M(q)$, the local dynamic susceptibility $\chi(\omega)$ and the magnetic spectral response $S(q, \omega)$. We shall show that the magnetic form factor shows free ion behavior in both phases, indicating that from the point of view of magnetic properties, the $4f$ electrons are strongly correlated both in the α and γ phases. The dynamic magnetic susceptibility of the two phases is very different. It shows a sharp low energy peak at the characteristic energy, which scales with the coherence temperature of each phase. Since the coherence scale is directly connected with the strength of hybridization, this suggests that the hybridization plays a central role in the $\alpha - \gamma$ transition in cerium.

Details of method

In this study, we have performed DMFT+DFT calculations in a charge self-consistent implementation [51]. For the Kohn-Sham potential, we used the GGA functional as implemented in Wien2k package [19], and continuous-time quantum Monte Carlo (CTQMC) method to solve the auxiliary impurity problem [44]. We used Hubbard repulsion $U = 6.0\text{eV}$, Hund's coupling $J = 0.7\text{eV}$, and temperature $T = 116\text{K}$. The lattice constants of the fcc unit cell are $a \approx 4.82\text{\AA}$ and $a \approx 5.16\text{\AA}$ for the α and γ phases respectively.

Magnetic Form Factor

As mentioned earlier, the magnetic form factor $F_M(q)$ is the Fourier transform of the spatial distribution of the electronic magnetic moment, here mostly contributed by $4f$ electrons. Thus it is an ideal observable for determining the nature of the $4f$ electrons. In particular, the magnetic form factor can determine whether $4f$ electrons are localized or itinerant, as suggested in Ref.[62]. The idea is the following: band formation results in the quenching of the $4f$ magnetic moment, especially the orbital component relative to the spin component. Thus, if the volume collapse is due to a localization-to-delocalisation transition, there should be a dramatic change between the shape of the magnetic form factor between the α and γ phases. For γ cerium, the measured magnetic form factor has free ion behavior, which is in good agreement with the computed ionic Ce^{3+} magnetic form factor [113]. On the other hand, for the α cerium, electronic structure calculations predict metal-like behavior for the magnetic form factor [62]. However, these calculations are in striking contrast with recent high-energy neutron inelastic measurements by Murani et al. [90], which show free ion behavior for the magnetic form factor of α cerium as well.

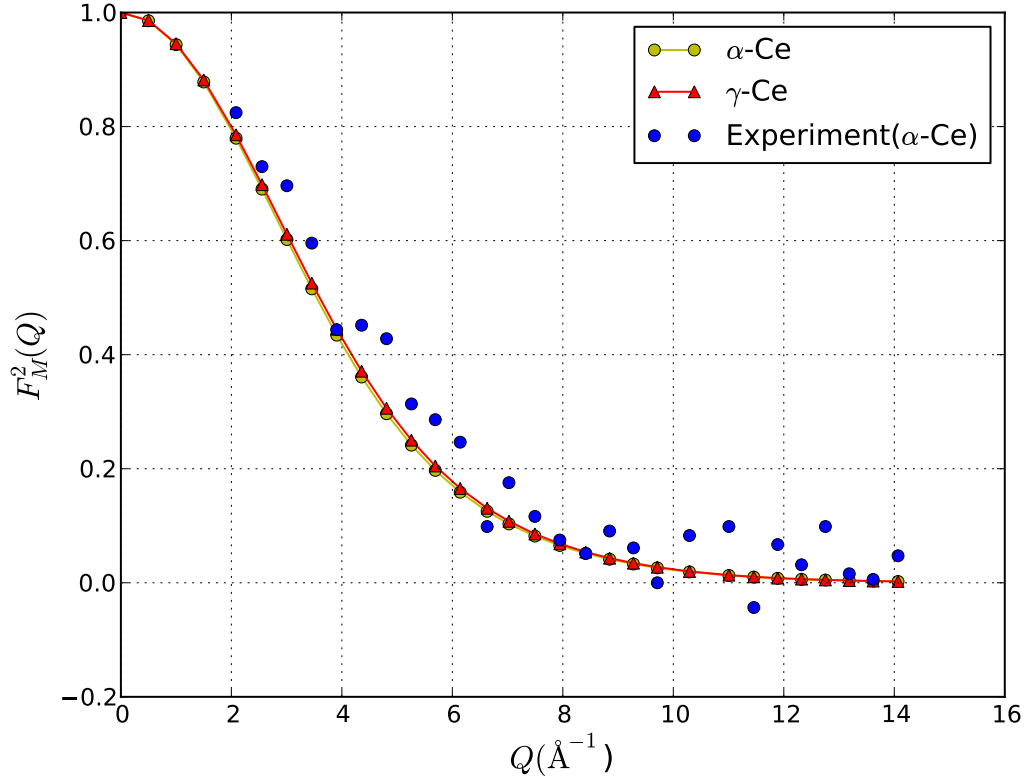


Figure 6.3: Momentum transfer dependence of the normalised magnetic form factor $F_M^2(Q)$ of α -Ce and γ -Ce. Blue circles show experimental data taken from Ref.[90].

| | α -Ce | γ -Ce |
|---------|--------------------------|--------------|
| μ_s | -2.3079×10^{-3} | -0.03468 |
| μ_L | 9.3668×10^{-3} | 0.13841 |
| C_2 | 1.327 | 1.334 |

Table 6.1: Values of the orbital (μ_L) and spin (μ_S) magnetic moment as obtained in our DFT+DMFT calculations under a magnetic field of 10T. The coefficient $C_2 = \mu_L/(\mu_L + \mu_S)$ determines the shape of the form factor in the dipole approximation and has similar value in both phases.

Following the formalism described in Ref.[99], we compute the magnetic form factor within the DFT+DMFT framework. Figure 6.3 shows the magnetic form factor squared $F_M^2(q)$ in presence of an external magnetic field for both α and γ cerium. The curves are close to each other and display free ion behavior, typical of a correlated state. This is a consequence of the electron-electron Coulomb repulsion, and cannot be captured solely by electronic band structure effects. Our results

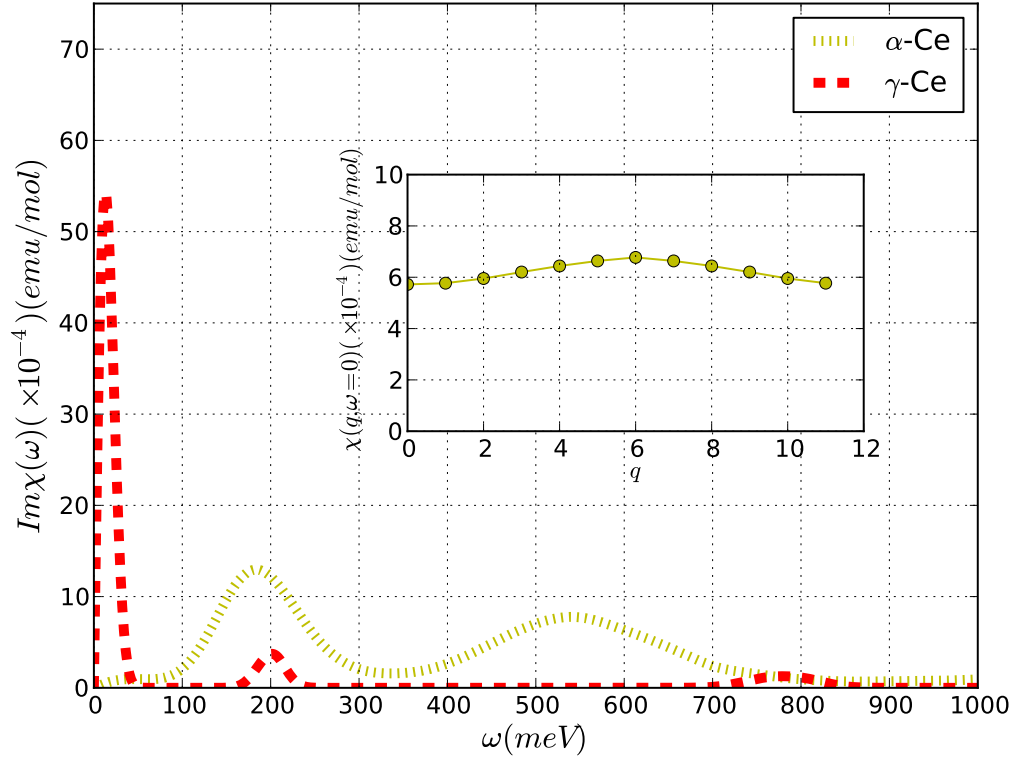


Figure 6.4: Imaginary part of the local dynamic magnetic susceptibility, $\text{Im}\chi(\omega)$, for α and γ cerium (yellow dotted and red dashed lines respectively). The inset shows the static susceptibility $\chi(q, \omega = 0)$ of α cerium as a function of q in the first Brillouin zone. Note that the q goes from the points (0,0,0) to (1,1,-1) in 12 uniform steps.

are in good agreement with the measured magnetic form factor of α cerium of Ref. [90], and show that electronic structure calculations, when combined with the dynamical mean-field theory, have the predictive power to capture the magnetic response of the $4f$ electrons, and therefore to reconcile theory and neutron scattering experiment.

To gain a deeper understanding of these results, we resort to dipole approximation, $F_M = \mu(\langle j_0 \rangle + C_2 \langle j_2 \rangle)$, where $\langle j_k \rangle = \int dr u(r) J_k(qr)$ is the spatial average of the spherical Bessel function $J_k(qr)$ over the atomic cerium wave function $u(r)$, $\mu = \mu_S + \mu_L$ is the total (spin plus orbital) magnetic moment, and $C_2 = \mu_L / (\mu_S + \mu_L)$. As shown in Table 6.1, μ_L and μ_S have opposite sign because of third atomic Hund's rule (that is because of spin-orbit coupling and $n_f < 1$), and $\mu_L > \mu_S$, thus $C_2 > 0$. The coefficient C_2 determines the shape of $F_M(q)$ and remains basically unchanged across the $\alpha - \gamma$ transition. It is close to the one expected for a free Ce^{3+} ion, implying that there is a localized $4f$ electronic density for both α and γ cerium.

Dynamic Magnetic Susceptibility

The magnetic form factor indicates that both α and γ phase are strongly correlated phases, which is compatible with both Mott and Kondo volume collapse scenarios, but eliminates the promotional model. In the Mott scenario, the two phases are correlated because they lie on slightly opposite sides of the delocalisation-localisation transition, while in the Kondo volume collapse picture, the two phases are correlated because the $4f$ electron moment remains stable across the transition. However, the Kondo volume collapse scenario differs from the Mott scenario because it does not consider the *spd* electrons to be mere bystanders, but emphasizes their role in the screening of the local magnetic moments, via the Kondo effect. Therefore, the dynamic magnetic susceptibility, which measures the spatial and temporal distribution of the magnetic fluctuations, can indicate whether the hybridization plays a key role at the transition.

In our calculations, we used the CTQMC impurity solver to obtain the local dynamic susceptibility $\chi(i\omega_n)$ of α and γ cerium as a function of Matsubara frequencies. We then analytically continued the data using maximum entropy method to obtain $\text{Im } \chi(\omega)$ along the real frequency axis. In Figure 6.4 we show $\text{Im } \chi(\omega)$ for both phases. At small frequencies, $\text{Im } \chi(\omega)$ for γ cerium shows a narrow and intense magnetic peak centered at approximately 10 meV. This feature has to be expected from the local moment character of electrons in γ cerium. The position of this peak gives a measure of the Kondo temperature T_K . For α cerium, this peak shifts to higher frequency, around 180 meV. Thus, in going from γ to α phase, there is a shift of magnetic intensity from low to high energy, signaling a change (precisely, an increase) in T_K . This is one of the central results of our work. We emphasize that, at large frequencies, the overall intensity of $\text{Im } \chi(\omega)$ in the α phase is larger than in the γ phase, reflecting the increased hybridization of electrons in the former phase.

In order to ascertain the nature of the different peaks in the dynamic susceptibility of α cerium, we performed simulations of the α phase with different values of spin-orbit coupling (not shown). Upon increasing spin-orbit coupling, the peak at low frequency (≈ 180 meV) moves towards $\omega = 0$. This is a feature of the fact that by increasing the spin-orbit coupling, the effective Kondo temperature of the system is reduced. Hence this peak is a feature of the Kondo coherence energy of the system. This trend has to be expected because of the hybridization between the conduction electrons and the f electrons. By increasing the spin orbit coupling, the energy splitting between the $5/2$ and $7/2$ states increases, therefore fluctuations are hampered and $7/2$ states are less occupied. It follows that the hybridization with conduction electrons decreases as well. The importance of the spin-orbit coupling has also been emphasized in the cerium compounds $\text{CeIn}_{3-x}\text{Sn}_x$ and CePd_3 [92, 91, 18].

The second peak (≈ 600 meV) however does not show sensitivity to the spin-orbit coupling. To

further ascertain the origin of the second peak, we performed simulations with altered values of Hund's Coupling J (not shown). The second peak is always roughly centered at $\omega = J$ indicating that it represents an excitation of the f-electrons in the (non-zero) doubly occupied sector of f-electron occupancy.

Notice that to crosscheck the validity of our analytic continuation procedure, we benchmarked our results against a well-known sum rule for $\text{Im}\chi(\omega)$. It is known that $\frac{1}{\pi} \int_{-\infty}^{\infty} n(\omega) \text{Im}\chi(\omega) d\omega = \langle \mu_z^2 \rangle$ where $n(\omega)$ is the Bose distribution function and μ_z is the magnetic moment along the z axis, which can be independently extracted in our simulation without need of analytic continuation. A good quantitative agreement is obtained in both phases.

In addition, we have verified that the local dynamical susceptibility $\chi(\omega)$ is a good representative of the behavior of the susceptibility $\chi(q, \omega)$ within the first Brillouin zone. This is important, because it verifies the so-called "single-ion form factor dependence" often used to analyze experimental data [90], where the dynamical structure $S(q, \omega)$ is factorized into momentum dependent form factor $F_M(q)^2$, and energy dependent structure factor $S(\omega) = \frac{1}{2} \frac{1}{1 - e^{-\beta\hbar\omega}} \text{Im}\chi(\omega)$, i.e, $S(q, \omega) = F_M(q)^2 S(\omega)$. To verify the quality of this approximation, we have computed the static susceptibility $\chi(q, \omega = 0)$ of α cerium within the first Brillouin zone using a two particle vertex method, developed in Ref.[98]. We calculate $\chi(q)$ using the Bethe-Salpeter equation $\chi(q) = (\chi_0^{-1}(q) - \Gamma)^{-1}$, where Γ is the two particle irreducible vertex, which we sample within DMFT, and χ_0 is the RPA susceptibility, which we compute using the full k-dependent LDA+DMFT green's function. Note that within DMFT, the two particle irreducible vertex Γ is local. The inset of Figure 6.4 shows $\chi(q, \omega = 0)$. We can see that there is no significant variation in the static susceptibility within the first Brillouin zone, which validates the "single-ion form factor formula".

Magnetic spectral Function $S(q, \omega)$

We then use this formula to compute frequency dependent $S(q, \omega)$ of both phases. Figure 6.5 shows the difference between the α and γ magnetic spectral response ($S_\alpha(q, \omega) - S_\gamma(q, \omega)$). In the lower panel we show the experimental spectrum [90]. There is a good agreement between the two, particularly in the position of the broad peak assigned to the Kondo screening in the α -phase. Note that the spectrum displayed in Fig. 6.5 becomes negative in the low energy region where γ -Ce susceptibility has sharp peak due to local moment character (see Fig. 6.4). This region has been left out of theoretical (as well as experimental) plot so as to enable better visualization of the other features.

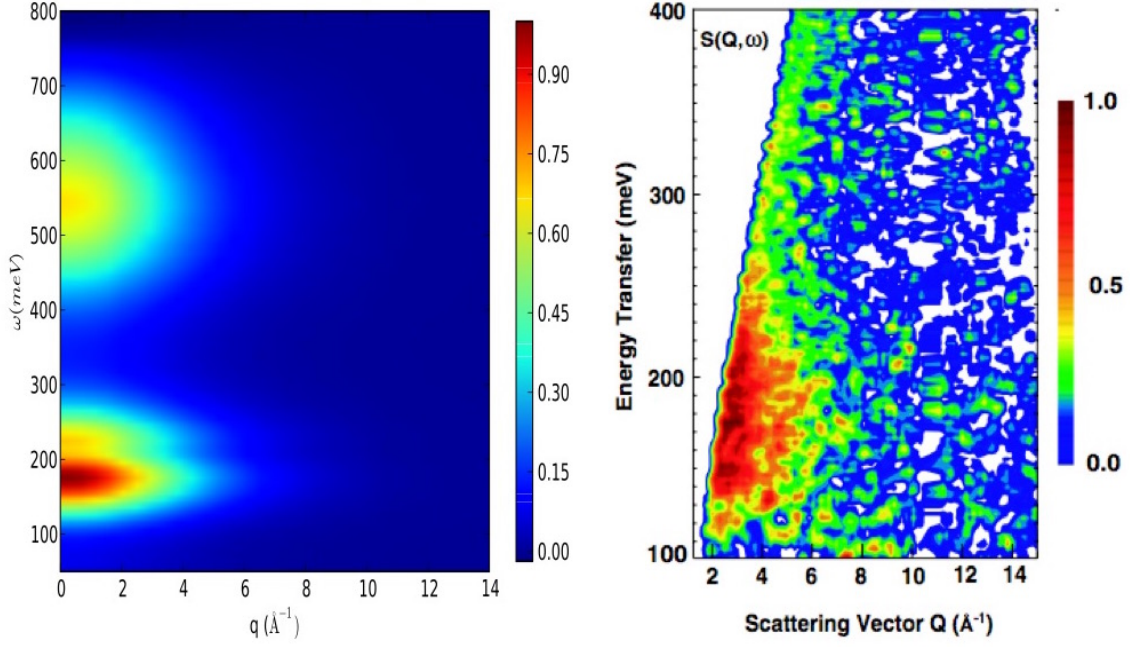


Figure 6.5: Difference of $S(q, \omega)$ between α and γ phase : Left panel shows DFT+DMFT results. Right panel shows high energy neutron inelastic measurements, taken from Ref [90].

Conclusions

In summary, we showed theoretically that the neutron magnetic form factor $F_M(q)$ has a free ion behavior in both phases, indicating that the $4f$ electrons remain strongly correlated across the α - γ transition. On the other hand, the local dynamical susceptibility $\chi(\omega)$ and the magnetic spectrum $S(q, \omega)$ show dramatic changes across the transition, with an energy shift from lower to higher frequencies, a direct consequence of the increase of the Kondo temperature T_K in the α cerium. Therefore, our data shows that the physics of the volume collapse α - γ transition in cerium is controlled by the hybridization between the localized $4f$ and the spd electrons and also establishes the importance of using different probes and observables to understand different aspects of the volume collapse transition in cerium.

6.2.2 The valence fluctuating ground state of Plutonium

Introduction

Plutonium (Pu) is well-known due to the radioactive instability of its nucleus which makes it an important material for nuclear fission. However, the electronic properties of Pu have also attracted a lot of attention due to the presence of multiple degenerate configurations due to its position in the periodic table. Pu is an actinide and therefore has an incomplete 5f electronic shell. Among the first few members of the actinide series, there is a volume contraction which is observed with increasing atomic number, due to the excess screening provided by the comparatively delocalized nature of the 5f electrons being added. However in the last few members of the actinide series, one observes an increase in atomic volume with increasing Z because at this point the 5f electrons are highly localized and do not screen the nuclear charge. Plutonium sits at the cusp of these two different subgroups of Actinides and therefore has an exceedingly complex electronic structure due to the complex interplay between localized and itinerant electronic degrees of freedom. This has resulted in this element being the subject of intense study for more than six decades. This complexity also manifests itself in the highly complex phase diagram exhibited by Pu, with six competing allotropic phases with unusually large volume differences between them of up to 25% accompanied by large variation in mechanical properties (see Fig 6.6 (a)). In this particular study we shall study the properties of the delta phase (δ -Pu), following closely the study published in [68], with very few additions.

The face centered cubic (fcc) δ -Pu (see Fig 6.6 (b)) displays Pauli-like magnetic susceptibility (like α -Ce) as well as an anomalously high Sommerfeld coefficient of the specific heat due to its unique combination of itinerant and localized electronic states [80, 101, 125]. This, coupled with its uses in nuclear technology makes it an extremely interesting problem to study in strongly correlated materials, as it is far away from the well understood limits of completely itinerant or localized electronic structures. This inability to describe the exact electronic structure properties has resulted in a lot of disagreement between theory and experiment, with theories that can accurately predict the volume and structural fluctuations concurrent with the phase transitions exhibited by Pu being completely unable to reproduce the lack of a static magnetic moment, as is required by the Pauli-like susceptibility shown by δ -Pu, and confirmed by experiments [56]. This is known as the missing magnetism problem of δ -Pu which is what we shall aim to address in this study.

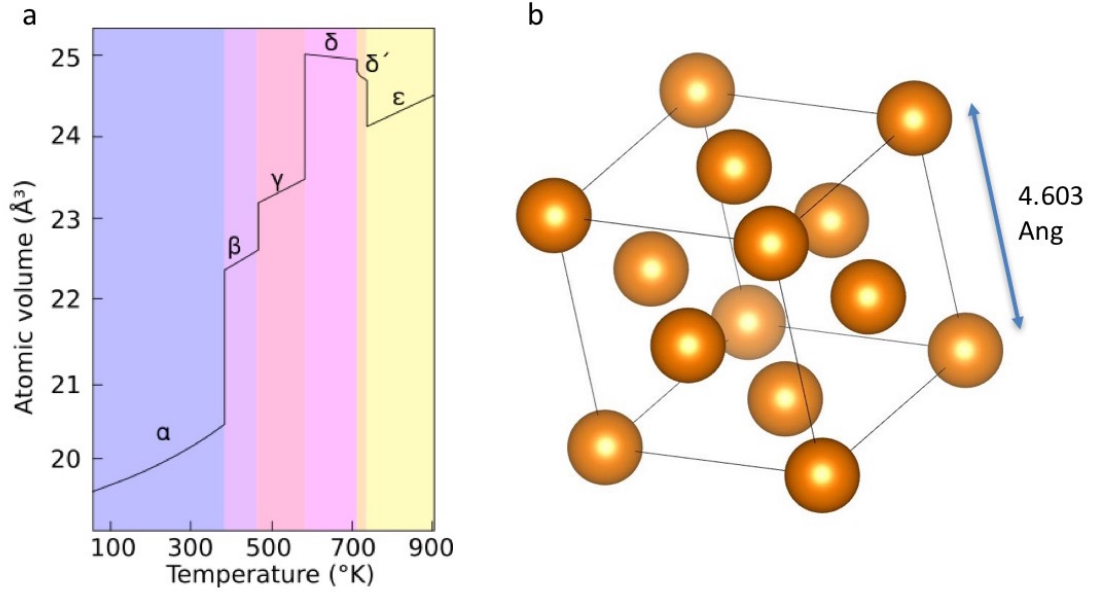


Figure 6.6: a) The Volume vs Temperature Phase diagram for Plutonium showing the multiple phases of the material. b) The FCC unit cell of δ -Pu

However, this kind of electronic structure problem where there is an interplay between localization/delocalization is exactly the domain where DFT+DMFT comes into its own. In order to correctly capture the physics of this material, we need to preserve the quantum mechanical fluctuations present, which result in the material fluctuating between multiple different atomic valency states, with the main ones being $5f^4$ (Pu 4+), $5f^5$ (Pu 3+), and $5f^6$ (Pu 2+). Since we preserve all local quantum fluctuations in DFT+DMFT, we can accurately model these virtual valence fluctuations. An extremely sensitive and important tool to capture this effect is the magnetic spectral function $S(q, \omega)$, because the magnetic form factor $\vec{F}_M(q)$ displayed by δ -Pu is markedly different than the one displayed by any calculations which neglect valence fluctuations. In addition, any accurate simulation of $S(q, \omega)$ would also have to display a susceptibility without a strong peak at very low frequencies, in order to rule out a static magnetic moment. In addition neutron scattering experiments, similar to Cerium, would provide an experimental verification of our theoretical predictions. Plutonium being a radioactive element, performing experiments on it can be extremely difficult. However recently experiments were performed at Los Alamos National Labs which have verified our calculations and which were published in Ref [68]. We shall present the results below but for more details the reader should refer to the reference. However it is to be noted that our theoretical results preceded the experiment, thereby showing the predictive power of DMFT when it comes

to properties of strongly correlated systems which cannot be simulated by most other methods.

Details of Method

In our calculations, we performed DFT+DMFT calculations with a Hubbard U of 4.5 eV and a Hund's J 0.512 eV. All calculations were performed at an electronic temperature of 232 Kelvin. As noted earlier for calculations of the magnetic form factor we have to use the NCA impurity solver due to the sign problem faced by CTQMC in the presence of off-diagonal hybridization introduced by the magnetic field used in form factor calculations. For calculations of the magnetic susceptibility, we used CTQMC. In order to obtain highly converged results, simulations were performed on the Titan supercomputer at Oak Ridge National Lab. Of the order of 500 DFT and 30 DMFT cycles (totaling 10 million core hours) were used for high quality runs, which can be analytically continued to real frequencies using maximum entropy. Spin orbit corrections were incorporated in all the simulations since spin-orbit corrections are very important in 5f materials.

Magnetic form factor

The magnetic form factor obtained by us is shown in Fig 6.7 (taken from our published paper [68]). The figure also provides the experimentally obtained form factor and the form factors that would have been obtained by considering a pure $5f^4$ or $5f^5$ valence, as well as a admixture of the two that is empirically close to the experimental results. Our DMFT simulations also predict significant mixed valence being present, with a resulting n_f being predicted which is in good agreement with core-hole photo-emission spectroscopy results [117] (refer to Table 6.2).

| δ -Pu 5f state | f^4 | f^5 | f^6 | Total n_f |
|-----------------------|-------|-------|-------|-------------|
| CHPES (%) | 6 | 66 | 28 | 5.21 |
| DMFT (%) | 12 | 66 | 21 | 5.12 |

Table 6.2: Comparison of the probabilities of different occupations of the 5f orbital predicted by CHPES and DMFT

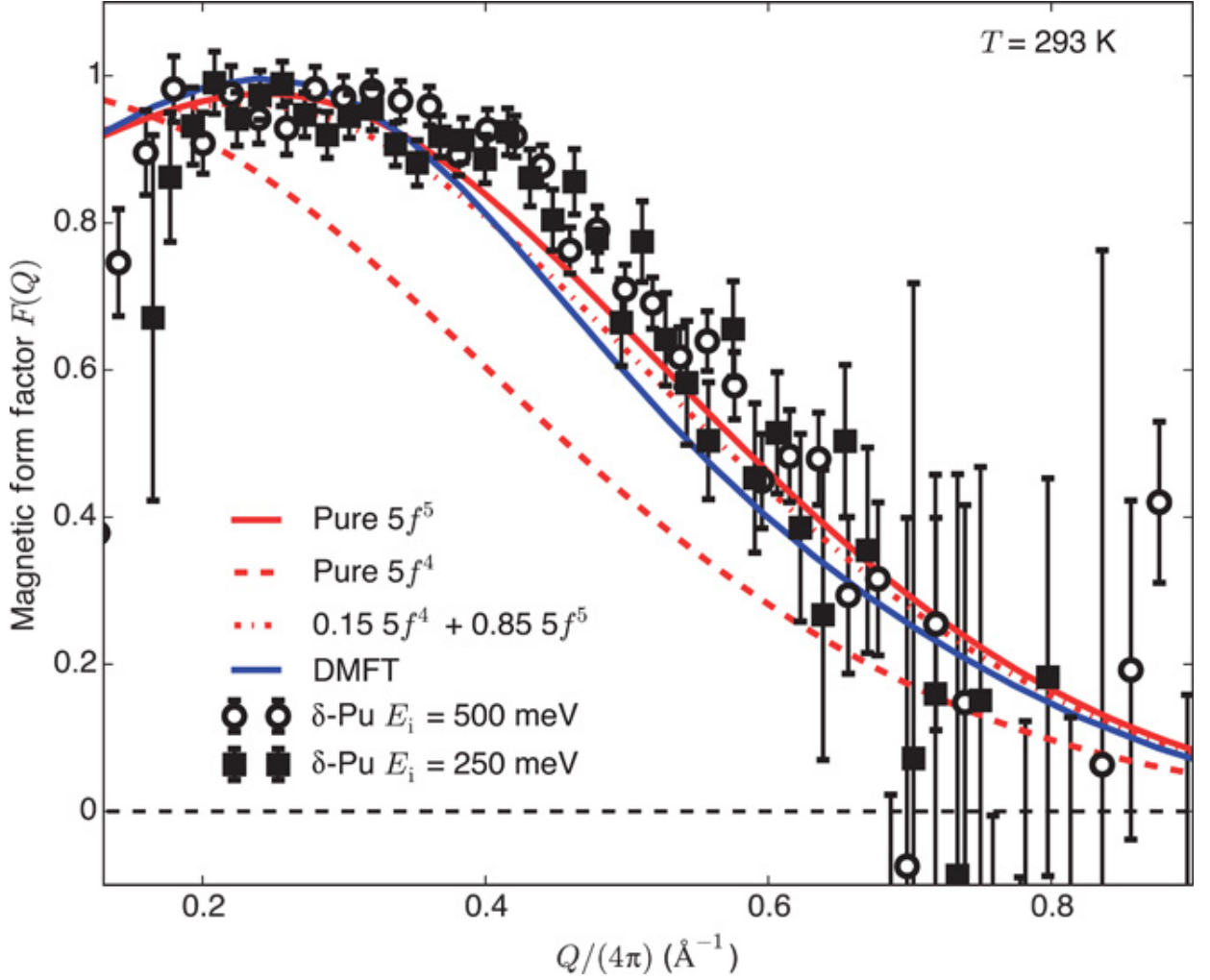


Figure 6.7: The DMFT form factor obtained by our simulations for δ -Pu, together with neutron scattering results at 250 and 500 meV incident neutron energies and the form factors that would have been obtained by considering a pure $5f^4$ or $5f^5$ valence, as well as a admixture of the two

As we see, DMFT is successful in capturing the correct form of the form factor. We see that the $5f^5$ form factor is also a reasonable fit with experiment. However a pure $5f^5$ state would have a magnetic moment and is hence not suitable to reproduce the Pauli-like susceptibility we observe. It is to be noted that at low Q , the experimental errors are very large due to experimental limitations. Therefore the discrepancies with experiment are not considered very relevant. However we clearly see that DFT+DMFT is successful in capturing the correct spatial dependence of $S(q, \omega)$ through the magnetic form factor.

Dynamic Susceptibility and $S(q, \omega)$

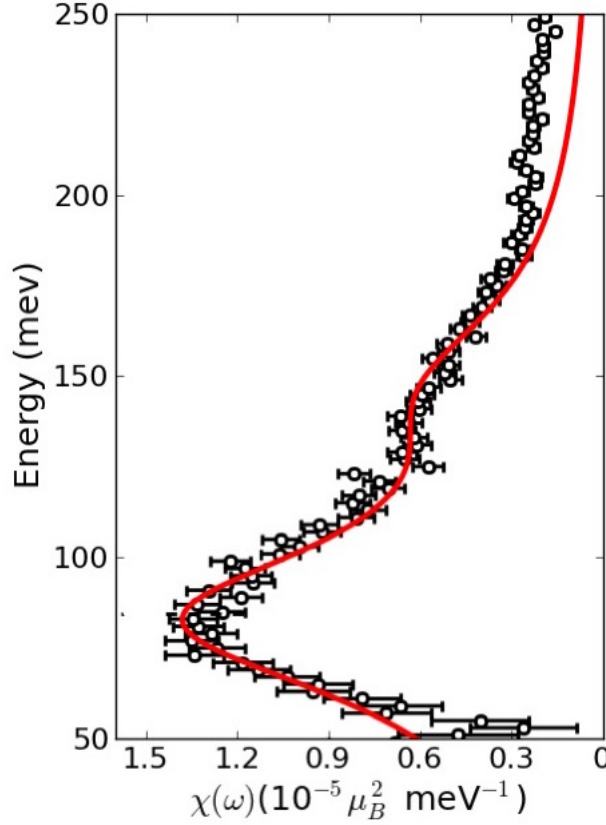


Figure 6.8: The imaginary part of the local dynamic susceptibility for δ -Pu compared to neutron scattering experiment [68]

The dynamic magnetic susceptibility calculated for δ -Pu is given in Fig 6.7. In the figure, we also see the experimental results from [68] (the actual reference contains multiple experimental results omitted here for clarity). As we see, DMFT is able to capture the correct location of the peak in the dynamic susceptibility at 84 meV, which gives us the relevant scale for spin excitations. It is to be noted that these results predict a Kondo Temperature of ~ 800 K (in agreement with results obtained by Haule et. al [109]) which explains why at room temperature the moment of the 5f state is screened by the Kondo screening cloud of antiparallely aligned conduction electrons , which screen the magnetic moment (see Fig. 6.9). This is central to the resolving the problem of missing magnetism and is perhaps the most important result in the paper. By using the sum rule in Eq. 6.5 we obtain a fluctuating moment of $\sim 0.8 \mu_B$ per atom which is also in good agreement with experiment [68]. Finally we note that for any static local moment phase, we would have seen a

Curie-like susceptibility which is characterized by a peak in the imaginary part of $\chi(\omega)$ at very low frequencies, analogous to γ -Cerium. However no such peak is observed. Therefore we can see that we have no local moment behavior in this material, further strengthening our claims.

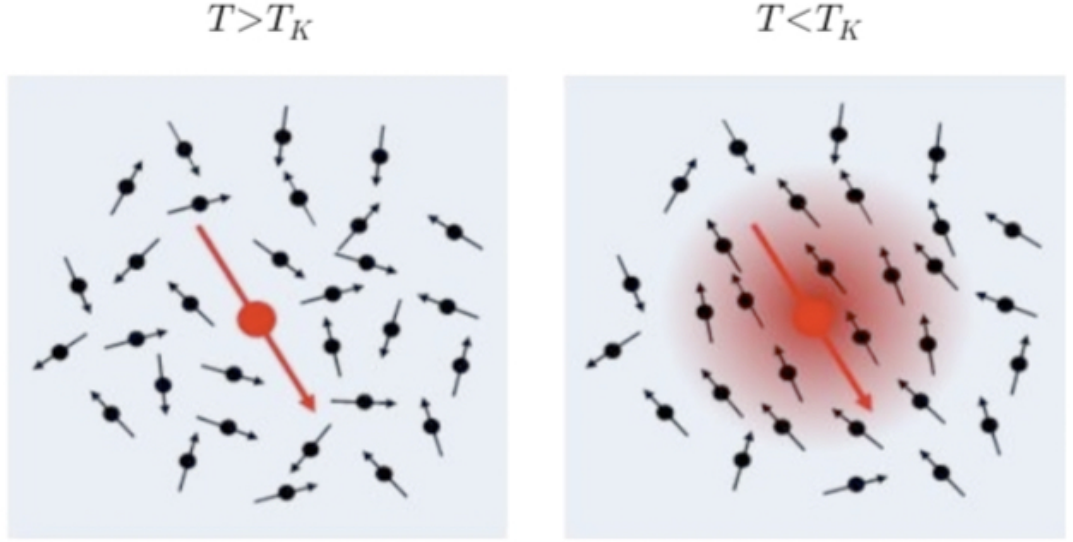


Figure 6.9: Illustrative figure showing how the magnetic moment is screened by the Kondo screening cloud below the Kondo temperature T_K . Taken from [68]

Finally we show in Fig 6.8 the $S(q, \omega)$ for δ -Pu using DFT+DMFT as well as by neutron scattering. As we can see (and as can be expected from the fact that both the form factor and the susceptibility are in good agreement with experiment) we can very good agreement between theory and experiment. Therefore we can claim that using DFT+DMFT, we can obtain an exceedingly accurate description of the magnetic spectrum of δ -Pu and get very important clues which shall help us in understanding the true nature of this compound.

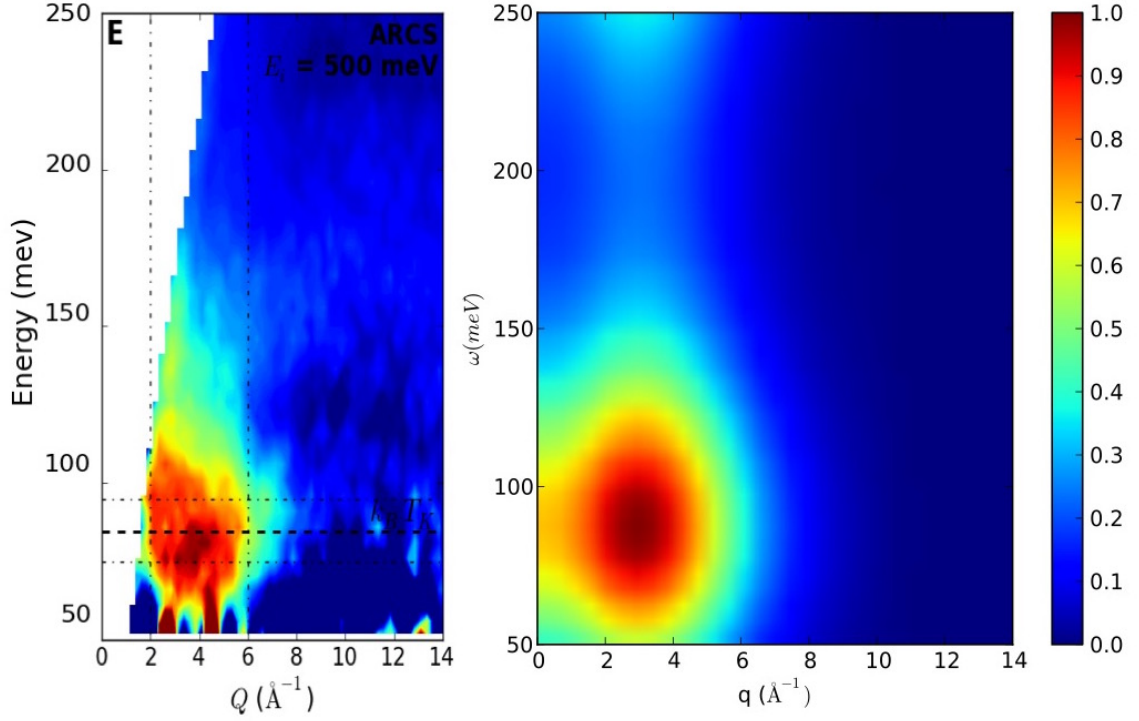


Figure 6.10: The Magnetic Spectral Function $S(q, \omega)$ for δ -Pu compared to neutron scattering experiment [68]. The dashed lines on the experimental figure denote the Q and ω values used to obtain the form factor and the susceptibility. The peak position corresponding to $k_B T_K$ is also marked

Therefore in conclusion, we have shown that we have developed a robust method to calculate the magnetic spectrum of correlated systems. We have used our method to understand the magnetic structure of both Cerium and Plutonium and have obtained very accurate experimentally verifiable results. Therefore we believe that in the future we can use our method to understand the magnetic properties of a large class of strongly correlated systems.

Chapter 7

Spin State Transition in LaCoO_3

7.1 Introduction

The spin state transition in LaCoO_3 has been the subject of intensive investigation for decades.[57, 93, 102]. At low temperature, this compound is known to be a narrow bandgap insulator with Pauli-like magnetic susceptibility. However between 90-150 K, it transitions to a local moment phase with a Curie-Weiss like susceptibility which reaches its peak around 150K. It also undergoes a gradual closing of the insulating gap and is known to be metallic above 600K [17, 31, 106].

There is considerable debate regarding the mechanism of this transition, mainly due to the uncertainty regarding the multiplet of the Co^{3+} ion which characterizes the excited state of the compound. The cobalt ion in LaCoO_3 is commonly considered to have a formal valence of 3+ and to be in the d^6 state. The scale of the crystal field splitting is comparable to the Hunds coupling energy scale. As a result, one would expect that as temperature is increased, there would be an entropy-driven transition from the low spin (LS) $S = 0$ state with a fully filled t_{2g} shell(t^6e^0) to an $S = 2$ high spin (HS) state (t^4e^2)[102]. Indeed there is experimental evidence to support such a scenario. Electron spin resonance[105], neutron scattering [100], X-ray absorption spectroscopy and magnetic circular dichroism experiments[55] point towards a transition to an HS state. In addition, no inequivalent Co-O bond is found in EXAFS experiments, which also supports the formation of an HS state due to the HS state not being strongly Jahn-Teller active [115]. However, it has been noted that in order to explain the XAS experimental data, one would have to assume that the crystal field grows with temperature, which is counter-intuitive.[30, 55] This led to some authors suggesting that there is an LS-HS alternating structure, which forms as a result of breathing distortions in the lattice [16] [102] and interatomic repulsion between the HS atoms.[79, 30]

A competing explanation, whereby the excited state is the $S = 1$ intermediate spin (IS) state (t^5e^1), has also become popular[57, 103], mainly because of LDA+U results which show that the IS state is lower in energy compared to the HS state.[75, 97, 94] The stability of the IS state has been justified by the large hybridization of the Co 3d electrons with neighboring O 2p electrons. This causes charge transfer between the ions resulting in the Co ion having a d^7 structure according

to the Zaanen-Sawatzky-Allen scheme,[127] which in turn would cause stabilization of the IS state. The intermediate spin state hypothesis also seems to explain experimental findings such as Raman Spectroscopy, X-Ray photoemission, other XAS and EELS spectroscopies, as well as susceptibility and thermal expansion measurements. [106, 1, 85, 73, 129, 39, 84, 119].

To summarize, there has been significant debate regarding the true nature of the spin state transition in LaCoO_3 (see Fig 7.1). Interest in this compound has also been enhanced in light of recent discoveries of ferromagnetism induced by Sr (hole) doping [78, 67, 15, 95], as well as experiments reporting strain induced magnetism in epitaxially grown thin films.[35, 33, 104, 32, 34, 60, 64]. Additionally, there have been reports of the emergence of a striped phase in thin films with alternating LS and HS/IS regions.[22] Low temperature ferromagnetism has also been reported in experiments on LaCoO_3 nanoparticles[29]. Hence, there is great interest in understanding the true behavior of this material.

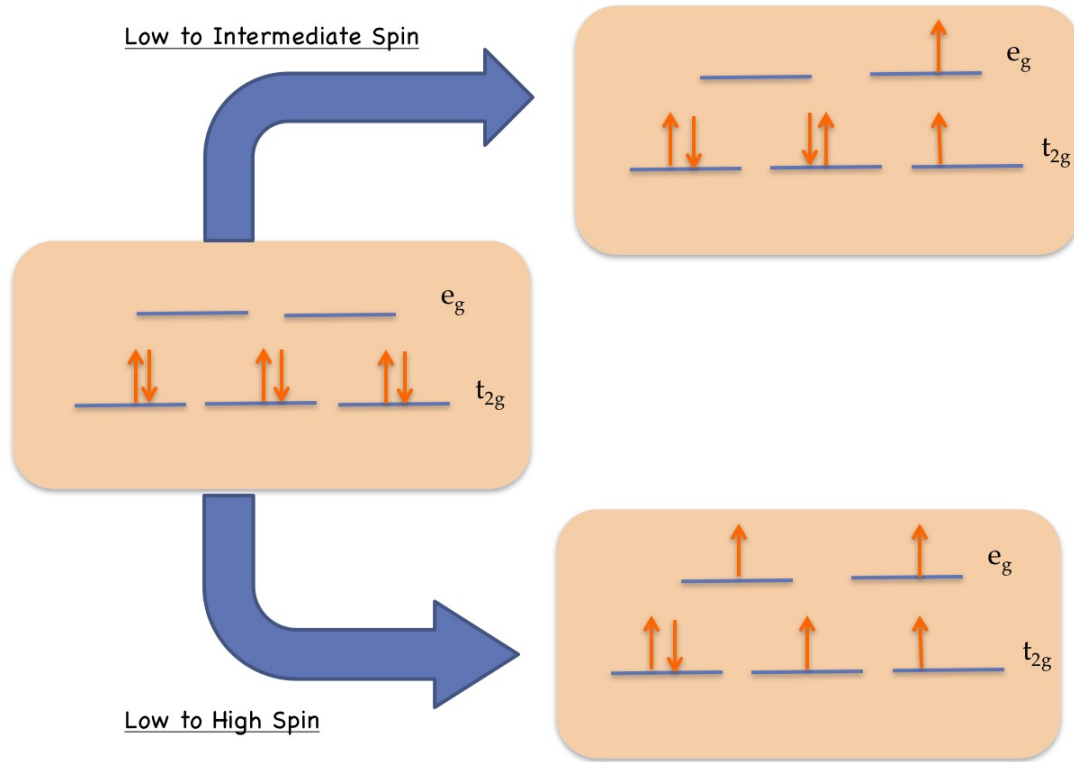


Figure 7.1: Schematic illustration of the two different scenarios for the the spin state transition in LaCoO_3

In this chapter (which has been submitted for peer-review and whose prperint can be found on

arxiv [20]), we use Density Functional Theory + Dynamical Mean Field Theory (DFT+DMFT) to analyze the spin state transition of bulk LaCoO_3 . As mentioned earlier in the methods section, Our implementation extremizes the DFT+DMFT functional in real space, thereby avoiding the downfolding approximation and uses the numerically exact CTQMC impurity solver[54, 45]. Even though there are multiple recent studies that use DFT+DMFT on this compound [27, 128, 72], to our knowledge none of them provide a comprehensive analysis of all of the factors governing the transition such as octahedral rotations and electronic entropy. We show that i) LaCoO_3 has large charge fluctuations and it is not possible to explain the spin state with a single multiplet at any temperature, ii) The crystal field splitting very sensitively depends on the details of the crystal structure, and taking into account not only the thermal expansion but also the oxygen octahedral rotations is very important, and iii) It is possible to stabilize an insulating phase (without orbital order) at intermediate temperatures where local moments are present, thereby showing that the metal-insulator transition is distinct from the spin state transition in this compound. We also show that iv) Electronic entropy difference between the high and low temperature states is necessary for the stabilization of the different spin states, which is a fact overlooked in various first principle studies so far.

7.2 Crystal Structure of LaCoO_3

LaCoO_3 is a perovskite, which has the rare earth La on the A-site and Co on the B-site, which corresponds to the center of the oxygen octahedron (see Fig 7.2). However, like most of the perovskites, LaCoO_3 has oxygen octahedral rotations (Fig. 7.3) which involves the oxygen octahedra rotating out-of-phase around the $[111]$ axes of the undistorted cubic highsymmetry structure. The rotation pattern in Glazer notation is $a^-a^-a^-$, which corresponds to the space group $R\bar{3}c$ (#167).

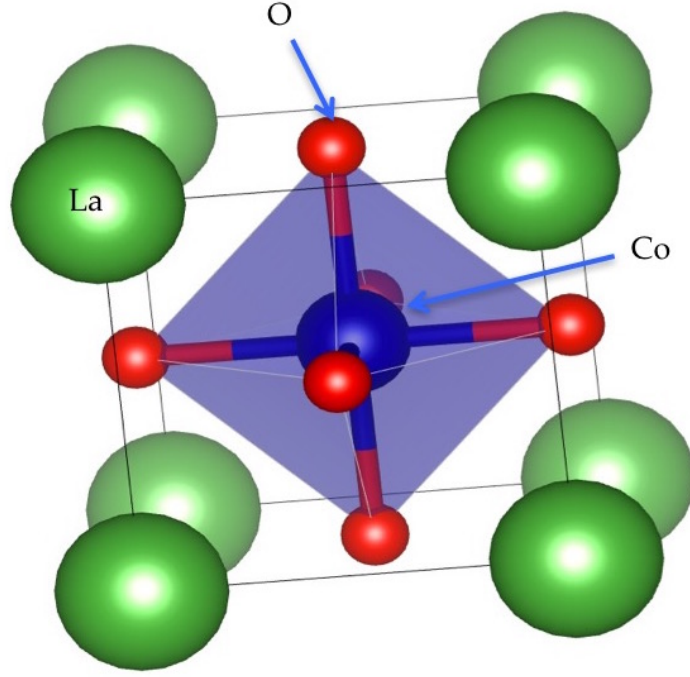


Figure 7.2: Conventional cell for a perovskite with no octahedral rotations ($a^0a^0a^0$ structure). In LaCoO_3 , the green atoms would be La, the red atoms O and the blue atom Co. The figure also shows the octahedra formed by the oxygen atoms around the Co atom

As noted by Thornton et. al. [116], LaCoO_3 has large thermal expansion and the octahedral rotation angle also changes with temperature. In our study, we used four different crystal structures to isolate and study the effect of different lattice parameters on the spin state transition. We used the two different experimental structures observed at 1143K and 4K, which we denote by HTa^- and LTa^- . Comparing the electronic structure for these two crystal structures provides a means to study the temperature evolution of the electronic structure. In addition to these two, we also built two crystal structures with the same strain state (unit cell vectors) as them, but with no octahedral rotations. These structures, denoted by HTa^0 and LTa^0 , enabled us to isolate the effect of oxygen octahedral rotations on the strain state of LaCoO_3 .

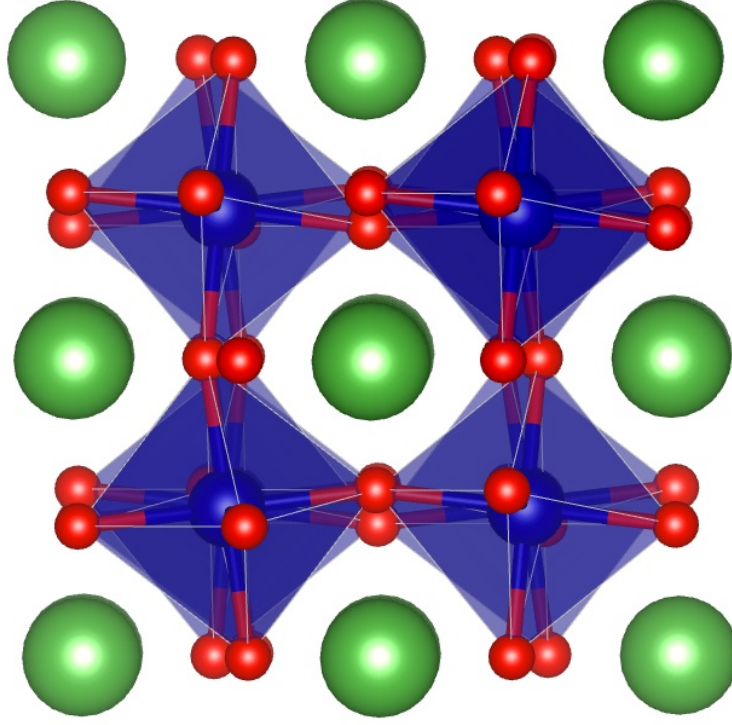


Figure 7.3: A depiction of the pattern of octahedral rotations that is present in LaCoO_3 . Each of the oxygen octahedra rotates in opposite direction to all nearest neighbour octahedra by the same amount relative to all three coordinate axes ($a^-a^-a^-$ structure).

7.3 Density of States

In Fig 7.4 we show the density of states for all 4 structures, calculated at both low temperature and high temperature (116K and 1160K) using DFT+DMFT. Unlike DFT, which always predicts a metallic state, our calculations correctly reproduce an insulating ground state at low temperature for all the structures. The t_{2g} orbitals are below the fermi level whereas the e_g orbitals are above the fermi level.

The charge gap closes continuously with increasing temperature, and as a result, there is a large overlap in energy between the t_{2g} and e_g orbitals at high temperatures. This overlap, however, is much smaller if the structures without rotations are simulated. (See Fig. 2b).

The HTa^0 structure shows some overlap at high temperatures, and the LTa^0 structure almost remains an insulator for the entire range of temperature studied, with a small overlap developing above 900K.

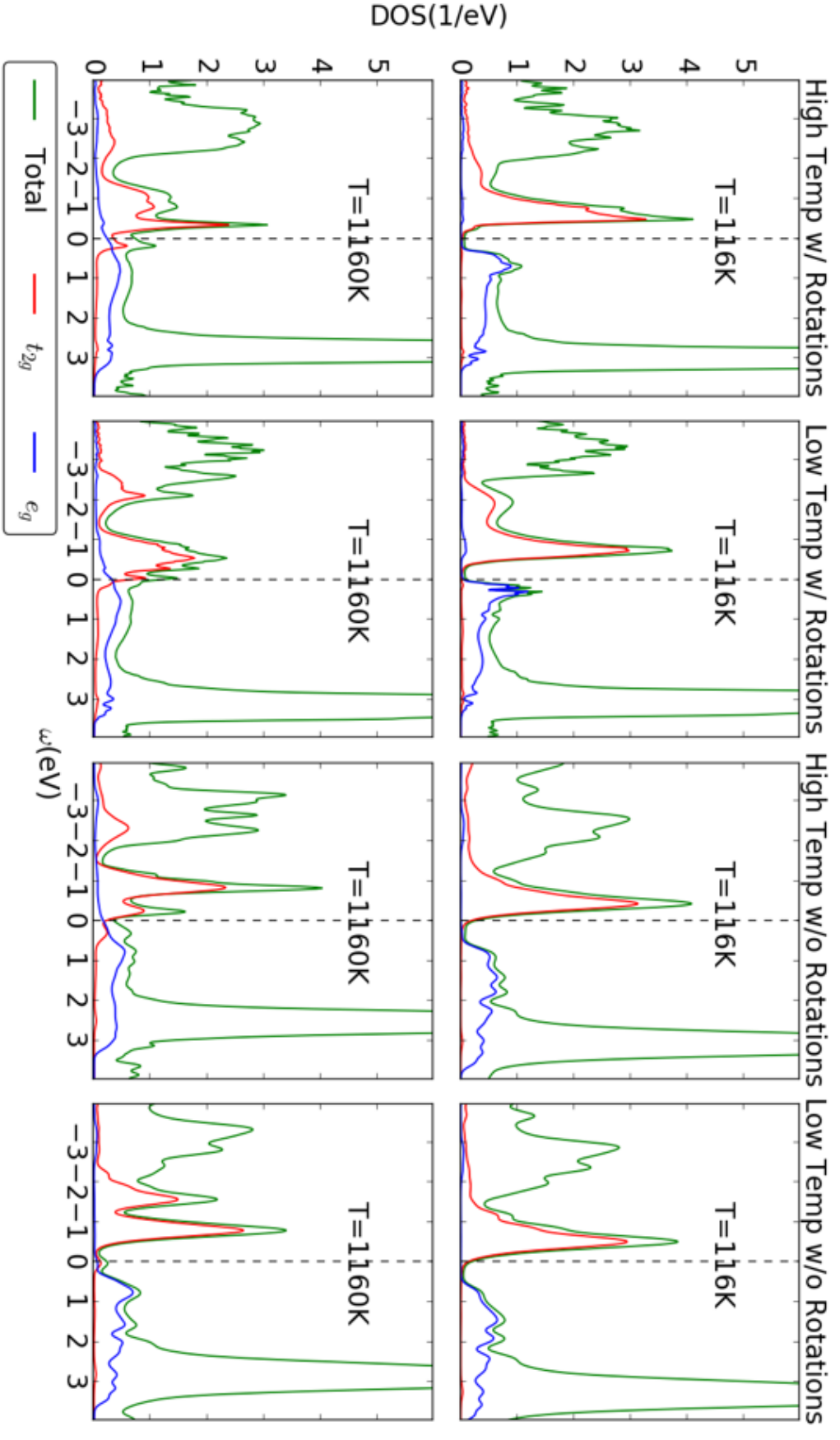


Figure 7.4: Density of states (t_{2g}, e_g and total including all atoms) for all four structures at 116K and 1160K

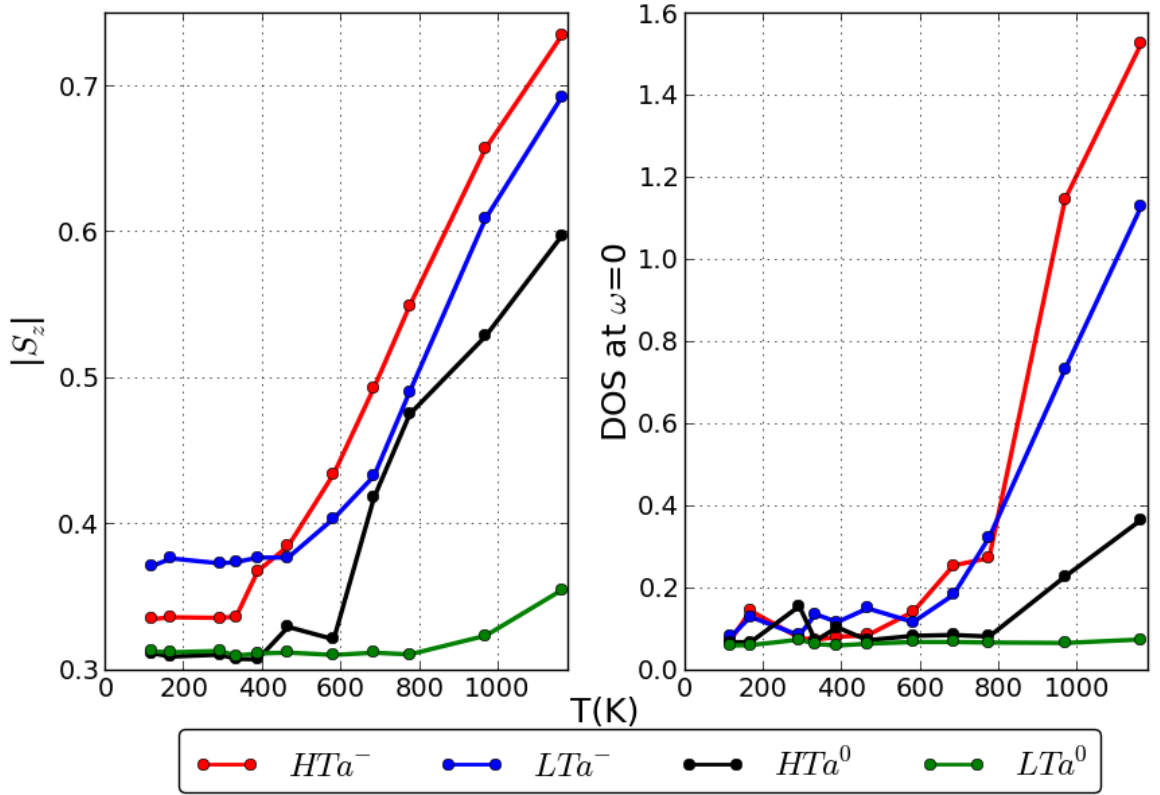


Figure 7.5: (a) Evolution of $|S_z|$ with temperature for all four structures. (b) Evolution of Density of states at fermi level with temperature for all four structures.

This shows clearly that octahedral rotations play a large role in decreasing the strength of the crystal field splitting. This can be explained by a combination of factors. The rotation of the oxygen octahedra causes misalignment of the crystal field of the O atoms with that of the La atoms, which normally reinforce each other in a perovskite with no octahedral rotations. This leads to an overall reduction of the effective crystal field which reduces the charge gap between the t_{2g} and e_g orbitals. In addition, this trigonal distortion also leads to a splitting of the t_{2g} orbitals into 2+1 orbitals, thereby again reducing the gap with the e_g orbitals (Note that in Fig 7.4 we have clubbed together all of the 2+1 orbitals into one single " t_{2g} " group because the splitting is small compared to the $t_{2g} - e_g$ splitting and doing so makes the figure clearer). The combination of these two effects seems to overcome the expected decrease in the bandwidth of the e_g orbitals caused by the bending of the Co-O-Co bond. Finally, note that there is a considerable overlap in energy of the O 2p orbitals with the Co 3d orbitals, which is very important in producing charge fluctuations on the Co ion, making it highly mixed-valent.

7.4 The spin state transition

In order to focus on the spin state of the Co ion, we calculate the expectation value of the magnitude of z-component of the spin $\langle |S_z| \rangle$. Note that all our calculations are in the paramagnetic state and hence the value of $\langle S_z \rangle = 0$. The results are presented in Fig. 7.5(a) as a function of temperature. Note that the quantitative value of the transition temperature is overestimated in our calculations. This can be explained by the fact that DMFT does not take into account finite wavelength fluctuations, and as a result, has a tendency to overestimate order like many other mean field methods. The largest value of $|S_z|$ at 1160K is seen for the HTa^- structure, followed by the LTa^- structure. This is in line with the stronger crystal field in the LTa^- structure due to the smaller lattice constant. We also observe that the spin state transition starts at a higher temperature for the LTa^- structure (~ 580 K) compared to the HTa^- (~ 380 K). This is also consistent with the low temperature structure having higher stability for the LS state. The structures without rotations consistently show lower buildup of higher spin states than the ones with rotations. The HTa^0 structure displays a spin state transition, but with an eventual high temperature value of $|S_z|$ that is lower. On the other hand, the LTa^0 structure shows almost no transition. This shows that the role that the octahedral rotations play in the reduction of the crystal field is essential for the spin state transition.

Figures 7.5(a) and 7.5(b) also show that the spin state transition and the charge gap closing occur at different temperatures, which is a trend that has been observed in experiment but has not been captured in earlier DMFT simulations. For example, Fig 7.5(b) shows that both the HTa^- and the LTa^- structures show a complete closure of the charge gap at ~ 600 K whereas Fig 7.5(a) shows that the spin state transition in the two structures occur at very different temperatures.

Note that while calculating the density of states(DOS) at $\omega = 0$ for the different structures at different temperatures, we ensured that their Fermi energies were adjusted such that the energy levels for the oxygen densities of states lay at the same energy values. This was required because there was an ambiguity in the value of the chemical potential at temperatures where the structure gave rise to an insulating band-gap and we believe an accurate comparison can only be made if some features of the DOS are held fixed. This procedure required a shift in the chemical potential of some of the simulations of the order of 0.1 eV. The results we plot in Fig 7.5(b) are obtained after these shifts are put in. Figure 1 on the other hand plots the densities of states before any such post-processing has been done. This leads to small differences between the two figures. Instead of fixing the Oxygen levels, we also tried fixing the Lanthanum f levels and this gave rise to very similar results. We firmly believe that our results displayed in figure 7.5(b) are robust and it is merely the relevant magnitudes of the y-axis values at high temperatures that fluctuate by a small

amount (depending on which features are held fixed) and not the actual temperature at which the charge-gap closure takes place. We also do not plot the DOS at $\omega = 0$ but the average of the DOS at five points around $\omega = 0$ as this takes care of some of the numerical noise that creeps into our calculation due to both Monte Carlo noise and the errors in analytic continuation. We also tested our results by averaging over different number of points and no significant changes take place that would affect our claims.

7.5 Nature of the excited spin state

Because of the large hybridization between Co and O, the d orbitals of Co have large charge fluctuations and all the four structures have an effective d-shell occupation of $n_d \sim 6.6$. Therefore any analysis of the spin states in terms of the LS, IS and HS states of the d^6 configuration of the Co ion is necessarily inadequate. In fact, our calculations show that the d^7 configuration has a higher occupation probability than d^6 ($\sim 47\%$ vs $\sim 42\%$), and there are also significant probabilities for d^5 and d^8

Fig. 7.6 shows the evolution of the occupation probabilities for the different values of $|S_z|$ with temperature. Even at high temperatures, $|S_z| = 0$ and $|S_z| = 0.5$ (the LS states for the even and odd occupancy sectors of the d orbital) remain the states with the highest probability. However, with the increase of temperature, the weight of the higher spin states increases. At the onset of the transition, the initial change in the value of the spin state is predominantly caused by the excitation of the $|S_z| = 2$ and the $|S_z| = 1.5$ multiplets. The $|S_z| = 1$ multiplet sees an increase in probability at higher temperatures (above 500K) and also follows a similar trend for all the structures except the LTa^0 structure, where all changes are very small. Therefore, the initial signature of the transition is best seen in the behavior of the $|S_z| = 2.0$ and $|S_z| = 1.5$ multiplets, which can be said to be the HS multiplets for the d^6 and d^7 occupancies respectively.

In Fig. 7.7, we show the occupancy histograms below and above the transition (at 116K and 1160K). (CTQMC gives us access to the state space probability for each of the 1024 states of the d orbital. However, in order to aid visualization, we only show states which have an occupation probability above 0.001 in any of the structures at any temperature.) This figure displays clearly how the transition is marked by the excitation of states in the higher spin multiplets. We see that the low temperature state for all of the structures is marked by the presence of a few states with large probability (mainly corresponding to the $|S_z| = 0$ and $|S_z| = 0.5$ states).

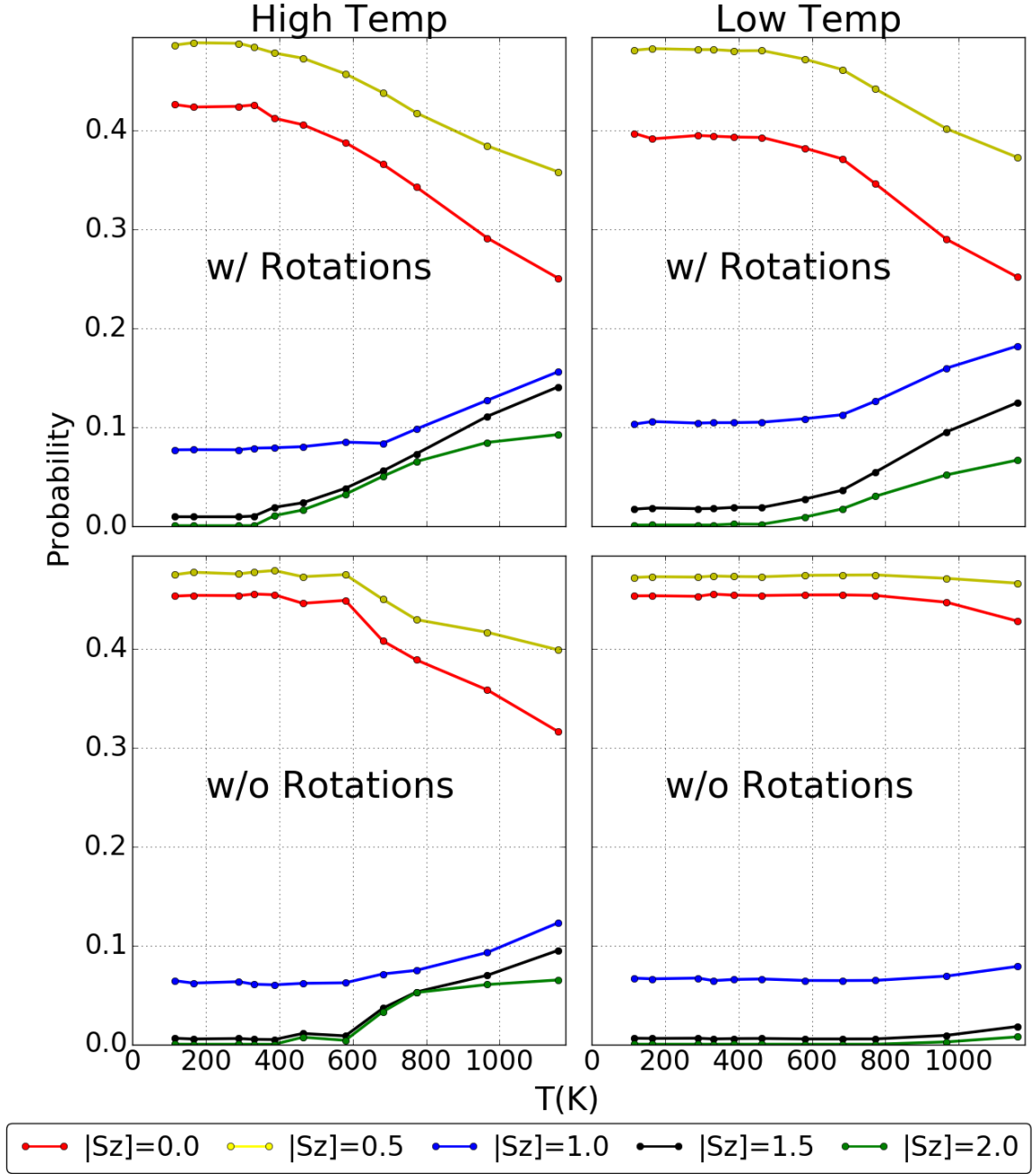


Figure 7.6: Evolution of occupation probabilities for all the spin states for the four structures with temperature.

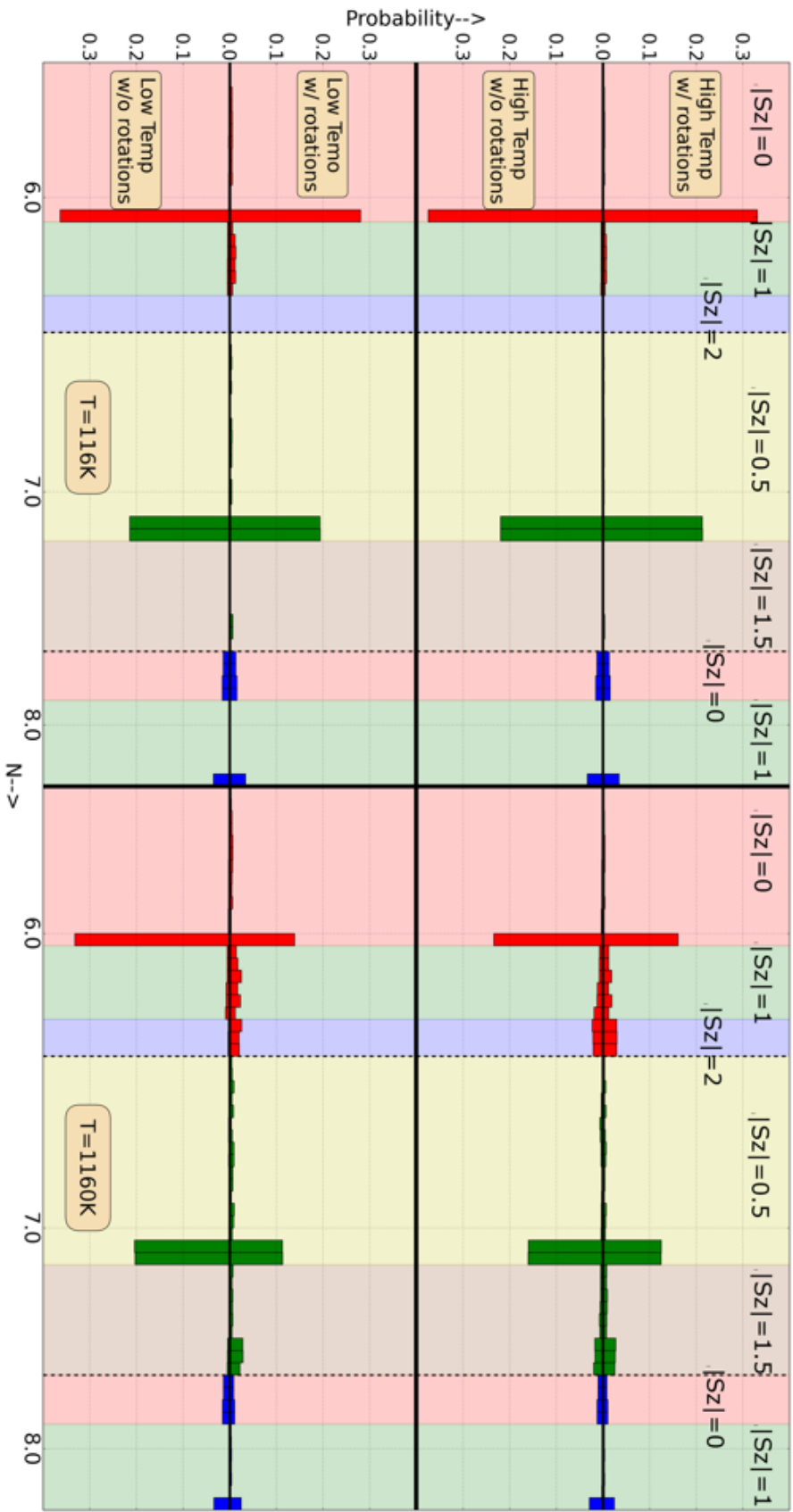


Fig 7.7 Occupancy histogram showing the occupancy Probability for the different atomic states for the d orbital of the Co atom for all the four structures at two different temperatures. The different background colors mark the areas reserved for different spin sectors. The lower x axis ticks as well as the color of the histogram bars denote the different occupancies of the d orbital. Note that odd occupancies only allow half integer values of $|S_z|$ while even ones allow integer values

As the spin state transition sets in, a large number of higher spin states get excited and the LS spin states lose weight. Note that the high spin states are highly degenerate so there is no one large peak for the high spin states, but a multitude of lower peaks. This supports the idea that the transition is primarily an entropy driven transition. We can also get a good idea of the relative strengths of the transition for the different structures: The largest change occurs in the HTa^- structure, and the smallest one happens in the LTa^0 .

7.6 Contribution of Electronic Entropy

According to the entropy driven transition scenario, which is supported by calorimetric measurements[114], $LaCoO_3$ favors higher spin multiplets at elevated temperatures because of the associated gain in electronic entropy as a result of the high degeneracy of these high spin states - a point missed by first principles calculations at the level of DFT. Access to higher spin states is also made easier by a larger lattice constant due to the reduced crystal field, so the gain in electronic entropy could also be a driving factor for the large thermal expansion seen in this material.

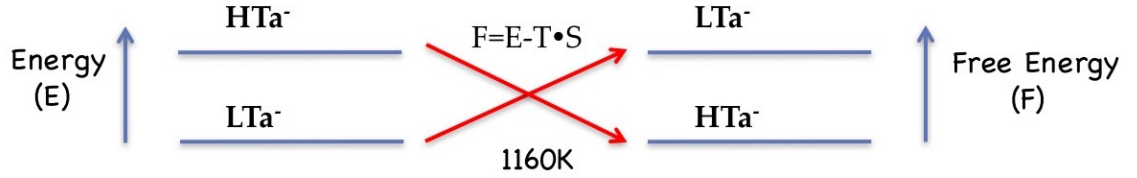


Figure 7.8: A depiction of the switch in stability between the LTa^- and HTa^- structures due to the impact of electronic entropy.

We calculated the contribution of the electronic entropy to the free energy using our state of the art DFT+DMFT implementation[48]. In particular, we evaluated the Free Energy and the Electronic Entropy for both the 4K and 1143K structures (LTa^- and HTa^-) at 1160K to predict if the structural changes make a considerable difference. The HTa^- structure is indeed much higher in electronic entropy compared to the LTa^- structure at 1160K; the difference in $T \cdot S$ between these two structures is ~ 110 meV per formula unit. This unusually large difference emphasizes the importance of electronic entropy to the transition. We also calculate the energy difference between the

HTa^- and LTa^- structures to be $\sim 70\text{meV}$ at 1160K with the LTa^- being lower in energy. Thus we see that when the entropy is taken into account and the Free Energy ($F=E-TS$) is calculated, the high temperature structure HTa^- becomes more stable purely due to the contribution of electronic entropy (see Fig 7.8). This result therefore confirms the structural phase transition that is observed as a function of temperature. So, we can conclude that the electronic entropy, which has been ignored in many first-principles studies of this material, is a leading factor in creating an anomalously large thermal expansion and driving the material to a high spin state.

7.7 Summary

We studied the spin state transition of LaCoO_3 using state of the art fully charge self consistent DFT+DMFT. By using different experimental and hypothetical crystal structures, we disentangled the effect of different components of the crystal structure and showed that both the thermal expansion and the presence of oxygen octahedral rotations have tremendous effect on the spin state transition of LaCoO_3 . Our single site DMFT approach reproduced not only the spin state transition but also the intermediate phase which has nonzero magnetic moment but is insulating. This shows that the spin state and the metal-insulator transitions occur at different temperature scales and that the magnetic-insulating phase can be reproduced without necessarily involving cell doubling via mechanisms such as breathing distortions of spatially inhomogenous mixed spin states. Our results emphasize the importance of charge fluctuations on the Co ion due to hybridization with the O anions, and thus point to the inadequacy of a simple spin state picture with only one formal valence. While the spin state transition is concurrent with a sudden change in occupation in the high spin multiplets, low and intermediate spin states also have significant occupation in the whole temperature range. Finally, our work is the first calculation of the electronic entropy of LaCoO_3 and it points to the fact that the difference of the contribution of entropy to the free energy is significant and is large enough to drive the spin state transition in this material.

Chapter 8

Investigation into the inadequacy of cRPA in reproducing screening in strongly correlated systems

8.1 Introduction

As we have seen in earlier chapters, achieving a truly *ab initio* description of materials with strongly correlated electrons is one of the prime objectives of condensed matter physics today. To recap, these compounds attract interest as they often have very complicated phase diagrams displaying a variety of interesting phenomena such as metal-Mott insulating transition(MIT), unconventional superconductivity, non-trivial magnetic order, charge/spin density waves etc[66]. These phenomena cannot be explained by free electron-based approximations and often lie beyond the scope of density functional theory(DFT),the workhorse for predicting properties of solids from first principles[71]. As we know, Dynamical Mean Field Theory (DMFT) seeks to overcome some of the difficulties of studying these systems by mapping the lattice problem to a numerically tractable auxiliary impurity problem coupled to a bath which is determined self-consistently. Various implementations of DFT+DMFT are currently available[11, 82, 5, 52, 2, 49],which mainly differ in i)the choice of how to project to the localized impurity degrees of freedom and ii)the energy window used while embedding the impurity self-energy into the DFT lattice eigensystem .Though the relative merits of a particular scheme might be dependent on the problem at hand, a common issue facing all of them is the determination of the material-specific effective interaction parameters like the Hubbard U and Hunds J for the correlated subspace. The lack of a reliable prediction procedure is one of the primary reasons this method cannot yet be considered truly *ab initio*, even though in the previous chapters we have been referring to it as such.

This well-known problem was pointed out soon after the introduction of the Hubbard model and early attempts to estimate the Hubbard U in real materials were made by Cox et.al [26]. Subsequent advances led to development of a method based on the Local Density Approximation(LDA) called cLDA (constrained LDA), in which the Hubbard U is calculated from the energy difference between different occupations of the localized orbitals after cutting off all hopping from the correlated orbitals to the itinerant states[87, 65, 10]. However, this method tends to overestimate U since a lot of

physical screening channels are eliminated when the hoppings are cut off (Note that there have been recent attempts to improve cLDA by incorporating linear response [23]). Recently, another approach based on the Random Phase Approximation(RPA) called constrained RPA (cRPA)[112, 13] has gained popularity as it is material-specific and provides a clear picture of the physical screening channels which are taken into account. cRPA has been applied to a variety of strongly correlated systems such as transition metals and their oxides[14, 88, 118, 108, 107], early lanthanides[96, 6] and high-Tc superconductors[89, 123]. However, the Hubbard U predicted by cRPA is generally not in good agreement with the value required by DMFT impurity solvers to achieve agreement with experiment. One notable example [6] is elemental Cerium for which the U predicted by cRPA is about 1eV, which is far smaller than the value of around 6eV used in practice, and which was used by us to obtain excellent experimentally verified results in chapter 6. This is not surprising since the Ce f orbital is more localized than the transition elements' d orbital and cRPA (due to its use of RPA-like screening processes) is suspected to be inadequate for such strongly correlated systems. In spite of this, there has been little theoretical investigation into exactly why cRPA fails in the strongly correlated regime. Instead most of the recent research on cRPA has focused on the energy window to be used in the cRPA procedure and the definition of the many-body model using the effective U predicted by cRPA [107, 89]. In view of the above, we firmly believe that further investigation is required into the root causes of the failure of this method when strong correlations are present.

In this chapter (which shall soon be submitted for publication in an almost identical form), we investigate the accuracy of cRPA using a class of model Hamiltonians based on models used to study strongly correlated materials. This allows us to study the fundamental causes for the failure of cRPA in strongly correlated systems in general, instead of merely making predictions about a specific compound. In all of our models, we include strong hybridization between localized and itinerant bands as the accuracy of cRPA is particularly questionable in such systems. Our models are two dimensional and we retain all density-density Hubbard interactions, reminiscent of the models used to study typical transitional metal oxides. We use DMFT to compute the spectra and quasiparticle residues of both the full multi-orbital model as well the effective one-orbital model using parameters obtained from cRPA. We show that i) cRPA has a tendency to systematically overestimate screening in the system. ii) We also find that for a large range of parameters, inter-orbital and weakly correlated orbitals' U parameters have little effect on the spectrum, thus negating the fundamental screening mechanisms used in cRPA. iii) Instead, we study a far more accurate form of W and U using the DMFT local Polarization bubble which exactly includes all local interactions. Using this new method, we show that the true screening is far less than predicted by cRPA/RPA and that the actual U predicted by this method has little frequency dependence. iv) We also study

the fully screened interaction(W) evaluated using RPA and our new method and show that the RPA W is unable to capture the Mott transition and also shows no signatures of local screening processes, which are present in the W evaluated using our new method. Since local interactions are treated exactly in DMFT, this success of the local Polarization method clearly shows that DMFT takes into account all the predominant screening processes in strongly correlated systems which are missing from RPA-based approaches.

8.2 Models and Methods

8.2.1 Model Hamiltonians

We start by introducing the two models, which we name dp model (for the two-band model) and dps model(for the three-band model). For the dp model, we parameterize the tight-binding part of our Hamiltonian using a two-component field $\psi_{\mathbf{k}\sigma}^\dagger = [d_\sigma^\dagger(\mathbf{k}), p_\sigma^\dagger(\mathbf{k})]$ in which $d_\sigma^\dagger(\mathbf{k})$ [$p_\sigma^\dagger(\mathbf{k})$] creates a d (p) electron with spin σ and wave vector \mathbf{k} . The Hamiltonian is given by :

$$H_0^{dp} = \sum_{\mathbf{k}\sigma} \psi_{\mathbf{k}\sigma}^\dagger \begin{pmatrix} \epsilon_d(\mathbf{k}) - \mu & t_{dp}(\mathbf{k}) \\ t_{dp}(\mathbf{k}) & \epsilon_p(\mathbf{k}) - \mu \end{pmatrix} \psi_{\mathbf{k}\sigma} \quad (8.1)$$

where

$$\begin{aligned} \epsilon_m(\mathbf{k}) &= E_m + t_{mm}(\cos(k_x) + \cos(k_y)) \quad m \in \{p, d\} \\ t_{dp}(\mathbf{k}) &= t_{dp}(\sin(k_x) + \sin(k_y)) \end{aligned}$$

This parameterization is motivated by recent research [42] investigating the significance of U_{dp} on the opening of the gap for the undoped cuprates and it describes electrons hopping on a two-dimensional lattice with two orbitals per site. The band dispersion and the one-electron thermal non-interacting Green's function matrix are given by:

$$E_\pm(\mathbf{k}) = \epsilon_+(\mathbf{k}) \pm \sqrt{\epsilon_-^2(\mathbf{k}) + t_{dp}^2(\mathbf{k})} - \mu \quad (8.2)$$

$$\hat{G}(k) = \frac{[i\omega_n + \mu - \epsilon_+(\mathbf{k})]\hat{1} + t_{dp}(\mathbf{k})\hat{\tau}_1 + \epsilon_-(\mathbf{k})\hat{\tau}_3}{[i\omega_n - E_-(\mathbf{k})][i\omega_n - E_+(\mathbf{k})]} \quad (8.3)$$

where $\hat{\tau}_i$ denotes Pauli matrices and $\epsilon_\pm(\mathbf{k}) = (\epsilon_d(\mathbf{k}) \pm \epsilon_p(\mathbf{k}))/2$.

In Fig. 8.1(a) and (c) we show the non-interacting density of states(DOS) and band structure of the model with the parameters $E_p = -2.0, E_d = 0.0, t_{dp} = 1.0, t_{dd} = 0.2$ (in units of t_{pp}). Unless specified otherwise, all the calculations in this chapter have been performed at a fixed total electron number per site $n = 3$ and at an inverse temperature of $\beta = 100$. We note that there are several Van-Hove singularities in the DOS due to the extrema in the energy spectrum. We can also see from

the from the orbital-resolved DOS that there is some mixture of d and p states around the chemical potential.

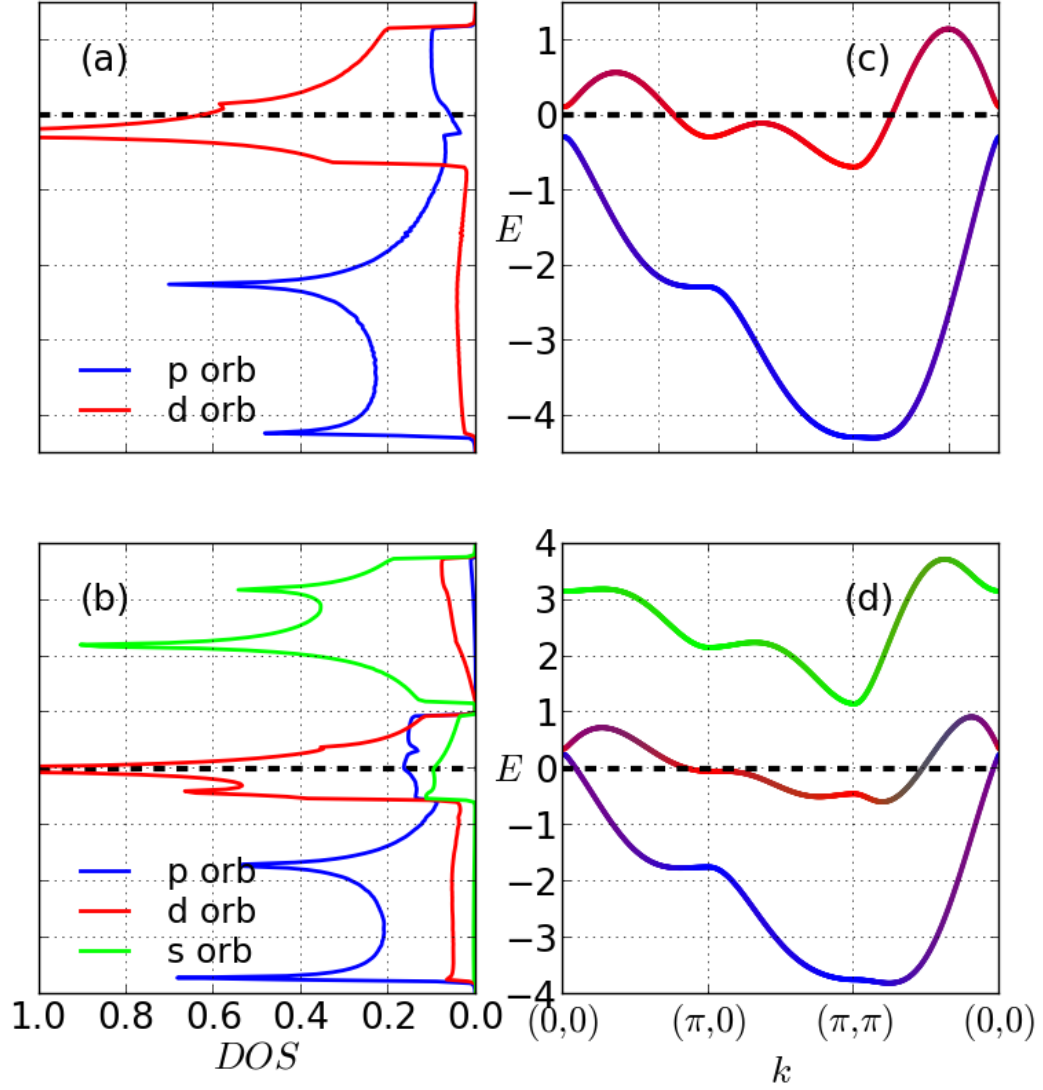


Figure 8.1: (a)-(b):orbital-resolved dos of dp model with $\mu = 0.28, n_p = 1.78, n_d = 1.22$ and dps model with $\mu = 0.038, n_p = 1.70, n_s = 0.14$ and $n_d = 1.16$.(c)-(d):band structure showing orbital characters of dp model and dps model. The dashed line denotes the chemical potential μ .

Next we turn to the dps model, in which we add a third band to the dp model with the aim of enhancing the particle-hole screening excitations in the system. The tight-binding part of the dps

model could be written using a three-component field $\phi_{\mathbf{k}\sigma}^\dagger = [d_\sigma^\dagger(\mathbf{k}), p_\sigma^\dagger(\mathbf{k}), s_\sigma^\dagger(\mathbf{k})]$:

$$H_0^{dps} = \sum_{\mathbf{k}\sigma} \phi_{\mathbf{k}\sigma}^\dagger \begin{pmatrix} \epsilon_d(\mathbf{k}) - \mu & t_{dp}(\mathbf{k}) & t_{ds}(\mathbf{k}) \\ t_{dp}(\mathbf{k}) & \epsilon_p(\mathbf{k}) - \mu & 0 \\ t_{ds}(\mathbf{k}) & 0 & \epsilon_s(\mathbf{k}) - \mu \end{pmatrix} \phi_{\mathbf{k}\sigma} \quad (8.4)$$

For simplicity, the parameterization used is similar to dp model

$$\begin{aligned} \epsilon_\alpha(\mathbf{k}) &= E_\alpha + t_{\alpha\alpha}(\cos(k_x) + \cos(k_y)) \quad \alpha \in \{p, d, s\}, \\ t_{dp}(\mathbf{k}) &= t_{ds}(\mathbf{k}) = t_{dp}(\sin(k_x) + \sin(k_y)). \end{aligned}$$

Here we choose $t_{ps}(\mathbf{k}) = 0$ with two considerations in mind: i) Physically, it is reasonable to take it to be zero as these two bands are well-separated in energy; ii) It is helpful in reducing the sign problem in our CTQMC impurity solver used while solving the DMFT equations, which are discussed in detail in section 8.2.3.

Fig. 8.1 (b) and (d) show the calculated DOS and band structure of the dps model with $E_p = -1.7$, $E_d = 0.0$, $E_s = 2.2$, $t_{dd} = 0.2$, $t_{ss} = 0.5$, $t_{dp} = 1.0$ (in units of t_{pp}). The basic structure of DOS resembles that of dp model except that there are more Van-Hove singularities in the dps model and more appreciable mixture of d and p,s states around the chemical potential.

For the interacting part of the Hamiltonian, we only retain all possible on-site density-density interactions and ignore exchange interactions such as Hunds Coupling. The interaction Hamiltonian is given by:

$$H_U^{dp(s)} = \sum_i \left(\sum_m U_{mm} \hat{n}_{im\uparrow} \hat{n}_{im\downarrow} + \frac{1}{2} \sum_{m \neq o} U_{mo} \hat{n}_{im} \hat{n}_{io} \right) \quad (8.5)$$

Here i labels the lattice site, $m, o \in \{p, d, (s)\}$, $\{U_{dd}, U_{pp}, U_{ss}\}$ represent the intra-orbital interaction strengths and $\{U_{dp}, U_{ds}, U_{ps}\}$ the inter-orbital interaction strengths. As the d band is taken to be the most correlated one, we place the added constraint that U_{dd} is the greatest of all the U parameters.

8.2.2 constrained Random Phase Approximation(cRPA)

In this section, we describe the cRPA scheme used in this paper. In cRPA[13], the Hubbard u^{cRPA} of the effective model is obtained by factoring in screening by the degrees of freedom involving the itinerant bands in an RPA-like fashion. We rewrite the total polarization function P as $P = P_r + P_d$, where P_d is the polarization function within the d subspace and P_r contains all other terms. Using this definition, the effective u^{cRPA} can be written as:

$$u^{cRPA}(q) = V(1 - P_r(q)V)^{-1} \quad (8.6)$$

with P_r approximated by only the particle-hole(RPA)“bubble” diagrams. The fully screened interaction W^{RPA} can be also evaluated using RPA by factoring in the screening effect of P_d on u

$$W^{RPA}(q) = u^{cRPA}(q)(1 - P_d(q)u^{cRPA}(q))^{-1} \quad (8.7)$$

The Feynman diagrammatic illustration for the summation procedure of the bubble diagrams used to calculate W^{RPA} or u^{cRPA} is shown in Figs. 8.3 and 8.2.

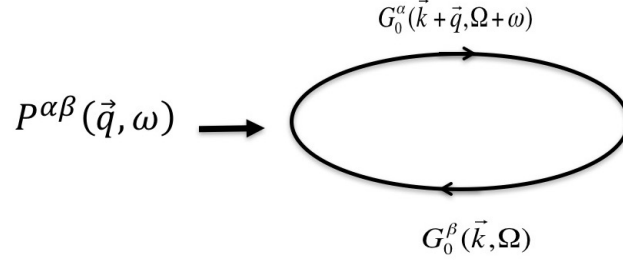


Figure 8.2: The Polarization bubble used in the RPA approximation. Note that the variables \vec{k} and Ω are summed over as per usual Einstein summation convention.

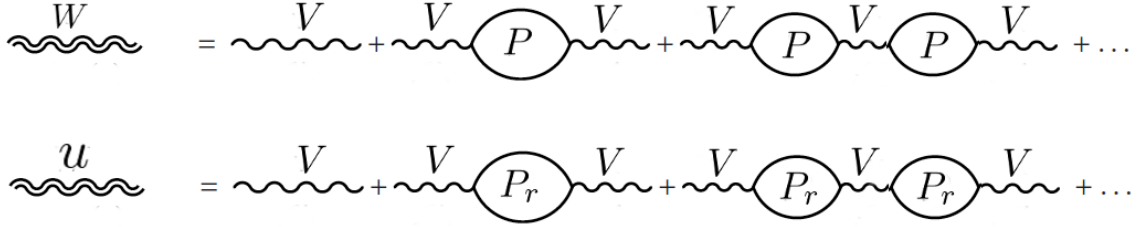


Figure 8.3: a) Figure showing the RPA screening process to obtain the fully screened interaction W from the unscreened interaction V . b) Figure showing the cRPA process to obtain the partially screened u from the unscreened interaction V .

Since we keep only density-density interactions in the model, the polarization function P in orbital basis depends on two orbital indices instead of four in general. The bubble polarization function is given by

$$P_{mn}(\mathbf{q}, \omega) = \sum_{\mathbf{k}, \lambda, \beta} a_{\lambda, \mathbf{k}}^{m*} a_{\lambda, \mathbf{k}}^n a_{\beta, \mathbf{k}-\mathbf{q}}^m a_{\beta, \mathbf{k}-\mathbf{q}}^{n*} \frac{f(E_{\beta, \mathbf{k}-\mathbf{q}}) - f(E_{\lambda, \mathbf{k}})}{\omega + E_{\beta, \mathbf{k}-\mathbf{q}} - E_{\lambda, \mathbf{k}} + i\delta} \quad (8.8)$$

and interaction matrix V in the two models are given by $(V)_{mn} = U_{mn}$ defined in Eq. [8.5], where $m, n \in \{p, d, (s)\}$ and wavefunction $a_{\lambda, \mathbf{k}}^n$ in λ band is $\langle n, \mathbf{k} | \lambda, \mathbf{k} \rangle$.

8.2.3 DMFT calculations

In order to solve our lattice models, we employ the DMFT method which maps them onto an impurity problem subject to the following self-consistency condition[37]:

$$\sum_{\mathbf{k}} (i\omega \mathbf{1} - h_0(\mathbf{k}) + \Sigma_{DC} - \Sigma(i\omega))^{-1} = (i\omega \mathbf{1} - E_{imp} - \Sigma(i\omega) - \Delta(i\omega))^{-1} \quad (8.9)$$

Here $h_0(\mathbf{k})$ is the kernel of the two tight-binding models $H_0^{dp(s)}$, Δ is the frequency-dependent hybridization of the impurity with the bath and Σ is the impurity Self Energy, which is approximated within DMFT to be equal to the (local) Self Energy of the system. The double counting(DC) term Σ_{DC} is needed to subtract the part of the correlation that is overcounted in our tight-binding models and the DMFT solution. We used the form for the DC term given in Eq. [8.10] which generalizes the standard DC correction to multi-band systems with interorbital interactions[12]. Note that the orbital occupancies used in the equation are obtained from the solution of the non-interacting model as that accurately gives us the Hartree shifts already taken into account by our model before DMFT corrections are put in. This is also in the spirit of the Double Counting corrections usually used in LDA+DMFT calculations where the atomic occupancies are used to calculate the Double Counting.

$$\Sigma_{DC}^m = \sum_{o \neq m} U_{mo} n_o + U_{mm} \frac{n_m}{2} \quad (8.10)$$

The quantum impurity model is solved using the numerically exact continuous-time quantum Monte Carlo method[122, 46]. CTQMC is known to have a sign-problem when large off-diagonal terms exist in Δ or Σ . However, for the dp and dps models considered here it can be proved that most off-diagonal terms in Σ terms vanish. We prove this using Eq. [8.9]. In the case of dp model, the off-diagonal hybridization function $\Delta_{pd} \propto \sum_{\mathbf{k}} \frac{t_{dp}(\mathbf{k})}{\det(i\omega - h_0(\mathbf{k}) + \Sigma_{DC})}$ in the first iteration by setting $\Sigma = 0$ in Eq. [8.9]. This turns out to be zero because $t_{dp}(\mathbf{k})$ is odd in \mathbf{k} and the determinant is even in \mathbf{k} . This says that Δ is diagonal in the first iteration. After solving the impurity model using diagonal Δ , the impurity self energy is also diagonal. Utilizing Eq. [8.9] again, one finds that Δ remains diagonal for nonzero but diagonal self energy. Similar analysis of dps model leads to Eq. [8.11]:

$$\Sigma = \begin{pmatrix} \Sigma_{dd} & 0 & 0 \\ 0 & \Sigma_{pp} & \Sigma_{ps} \\ 0 & \Sigma_{ps} & \Sigma_{ss} \end{pmatrix} \quad (8.11)$$

The lattice self-energy and Green's function are obtained by iterating our equations to self-consistency. As noted earlier, the chemical potential in all our simulations is adjusted such that the total electron occupancy is 3. As our DMFT scheme provides us with quantities on the imaginary (matsubara) axis, in order to obtain physical quantities on real frequency axis we use the maximum-entropy

analytical continuation method[69]. Additionally, in order to estimate the degree of correlations present in our model in different simulations, we calculate the quasiparticle residue which (within the of DMFT approximation) is given by:

$$Z_m = \left(1 - \frac{\text{Im}\Sigma_m(i\omega)}{\omega}\bigg|_{\omega \rightarrow 0}\right)^{-1} \quad (8.12)$$

where m is the orbital index.

8.3 Results

8.3.1 Density of states

In this section, we compare the densities of states(DOS) obtained for three different scenarios near the Metal-Mott insulator transition (MIT) for both the dp and the dps models using DMFT. The three scenarios we study are: 1) Full two-orbital(dp) or three-orbital(dps) DMFT with all on-site interactions factored in, which we dub the “2-orb/3-orb” scenario, 2)one orbital DMFT where we fix the value of the effective u_{dd} to the same value as full model (thereby neglecting any screening), which we name the “1-orb bare” scenario and 3)one orbital DMFT with an effective u_{dd} on the correlated orbital calculated using cRPA, dubbed the “1-orb cRPA” scenario. We emphasize here that the number of bands are the same in all three scenarios considered and the differences lie in the choice of correlated orbitals and value of the interaction in these subspace. The values for the interaction parameters used in our simulations are summarized in Table 8.1 These parameters give appreciable screening by cRPA and are therefore suitable to investigate its accuracy. With these sets of U , we find that in “2-orb/3-orb” scenario the critical U for the MIT for the dp model is $U_{dd}^{MIT} \sim 3.2$, while for the dps model $U_{dd}^{MIT} \sim 4.5$. For the “2-orb/3-orb” scenario, though there exist Hubbard-like interaction terms in the p or s orbitals, the self energies in these orbitals are normally negligible compared to that in the d orbital, as shown in Fig. 8.4 for dp model with $U_{dd} = 4.5$ and dps model with $U_{dd} = 6.0$. This clearly shows that an effective one orbital model can be defined which reproduces the physics of the full model in both cases.

| 2-orbital (dp) model | 3-orbital (dp) model |
|----------------------|--|
| $U_{pp} = 0.2U_{dd}$ | $U_{pp} = U_{ss} = U_{ps} = 0.1U_{dd}$ |
| $U_{pd} = 0.8U_{dd}$ | $U_{pd} = 0.6U_{dd}$ |
| | $U_{ds} = 0.3U_{dd}$ |

Table 8.1: Table containing interaction parameters used for the two different Hamiltonians in use in our simulations

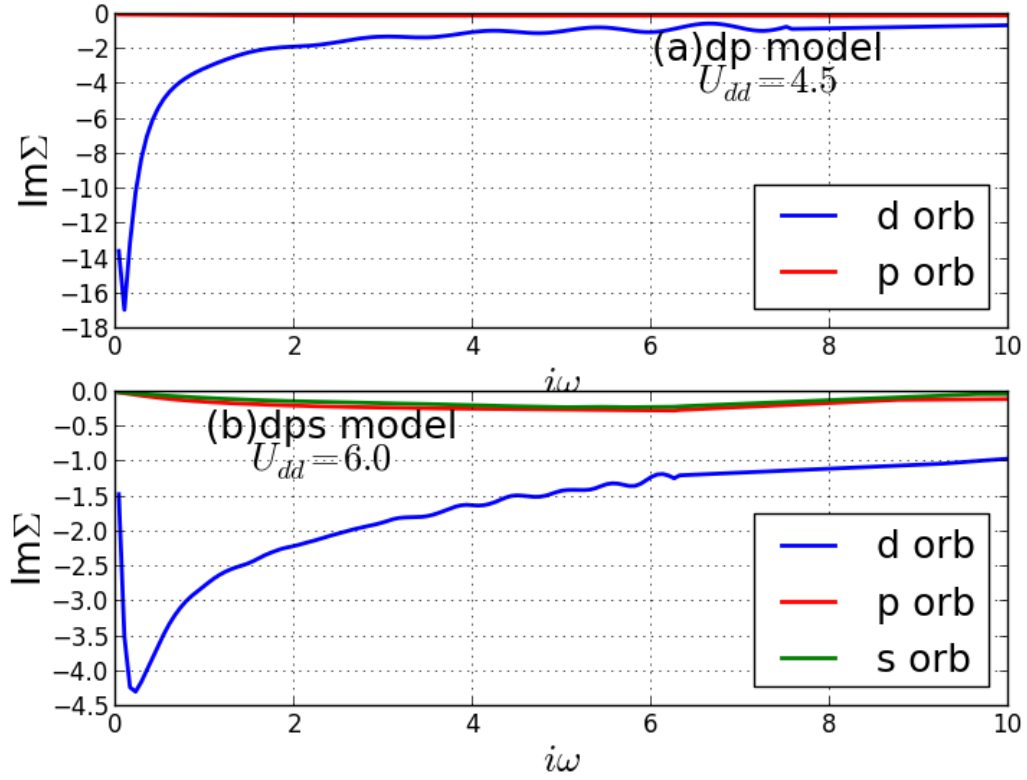


Figure 8.4: Comparison of $\text{Im}\Sigma$ in all orbital channels in “2-orb/3-orb” scenario for (a) dp model with $U_{dd} = 4.5$ and (b) dps model with $U_{dd} = 6.0$.

In order to calculate the effective interaction parameters predicted by cRPA, we obtained the screened frequency-dependent u and W for the critical values of U_{dd} for the two models given earlier. As shown in Fig. 8.5, cRPA predicts a static value of $u_{dd}^{cRPA}(\omega = 0) = 2.91$ for the dp model and $u_{dd}^{cRPA}(\omega = 0) = 3.26$ for the dps model. These correspond to about 35.3% and 45.7% screening for the dp and dps models respectively. We also note that within an energy window $0 - 3\text{eV}$, u is almost flat in both models, which means effective u will be very close to the static value even if one adopts a scheme accounting for frequency dependent u within a finite energy window. Therefore we believe that our static u based DMFT is more than adequate for these calculations.

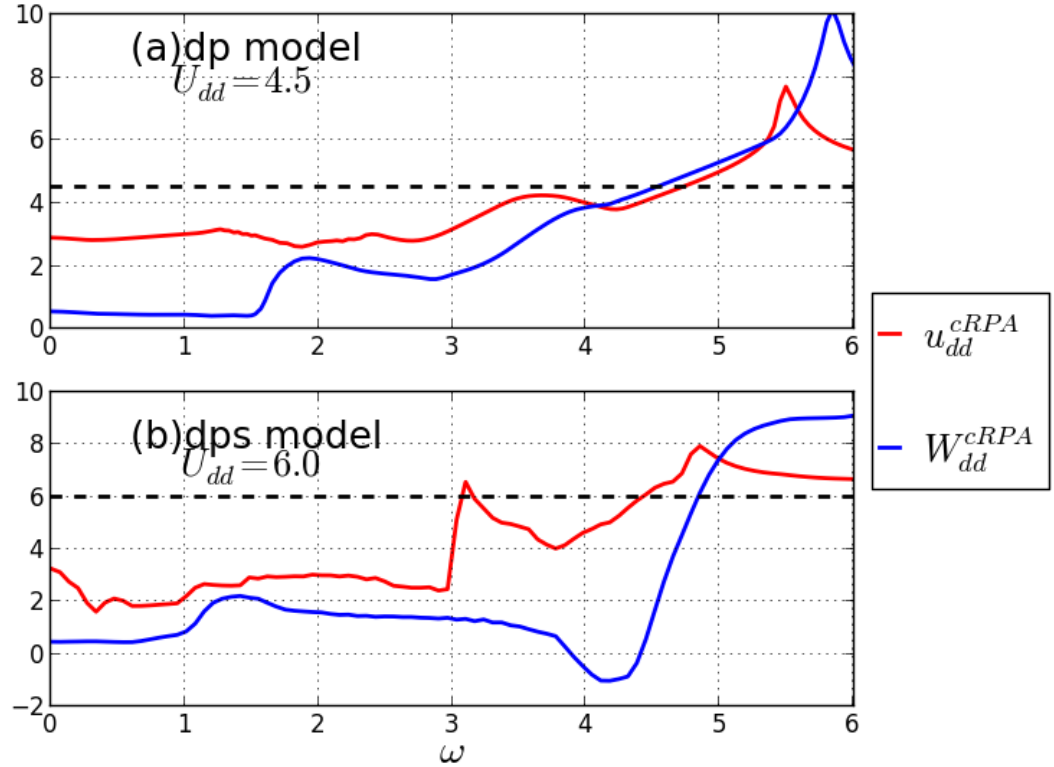


Figure 8.5: u_{dd}^{cRPA} and W_{dd}^{cRPA} of the dp(dps) model predicted by (c)RPA is shown in red (blue). The dark dashed horizontal line denotes the bare value of U_{dd} used in dp and dps model. Note that both u_{dd}^{cRPA} and W_{dd}^{cRPA} approach the bare value in the limit of high frequency as expected (not shown here).

Next we present the central result in this section: comparing the spectral functions of the three scenarios for both models. We compare only the d-orbital DOS as the dos of other orbitals share similar trend. As shown in Fig. 8.6, we find that for both dp and dps models with the critical parameters defined above, the “1-orb cRPA” scenario is metallic, in sharp contrast to the Mott-insulating “2-orb/3-orb” and “1-orb bare” scenarios. This shows that in the models we considered the bare scenario is a much better approximation to the original many-orbital model compared to cRPA. cRPA grossly overestimates the amount of screening that is present in these models near MIT. The fact that the “1-orb bare” scenario accurately reproduces the spectra also shows that U_{dp} and U_{pp} treated dynamically have very little effect on the system, which further negates the fundamental screening mechanisms used in cRPA.

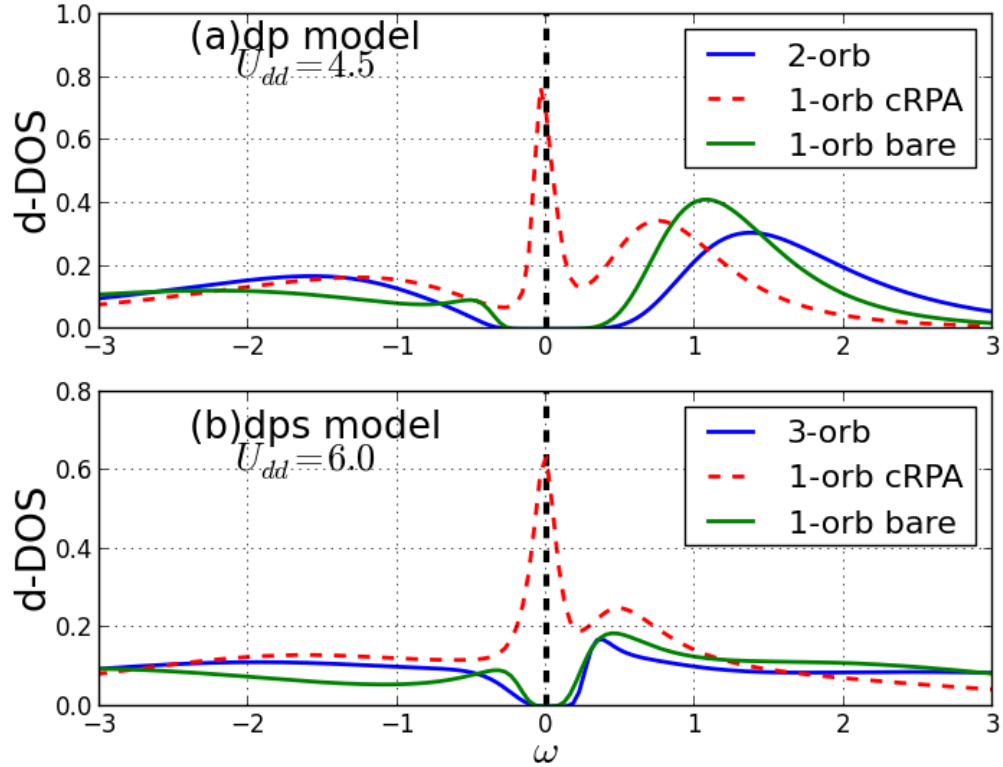


Figure 8.6: Comparison of dos of d orbital (d-DOS) within three scenarios for (a) dp model with $U_{dd} = 4.5$ and (b) dps model with $U_{dd} = 6.0$.

8.3.2 Quasiparticle Residue

In order to further illustrate the inaccuracy of cRPA, we shall now show how the “1-orb cRPA” scenario deviates from the other two for a broad range of U_{dd} by comparing the quasiparticle residue Z_d of the d-band (calculated using Eq. [8.12]) in the three scenarios for both models. Z_d gives us the extent of the correlations present in the correlated band and (within the DMFT approximation) is the inverse of the effective mass of the quasiparticle excitations. So a value of 1 would denote lack of correlation, whereas $Z_d \sim 0$ would signal proximity to an insulating solution with Z_d becoming zero at the critical U . From the results shown in Fig. 8.7, we see that cRPA always overestimates screening, with the discrepancy getting more pronounced as the U_{dd} approaches the critical value for the MIT.

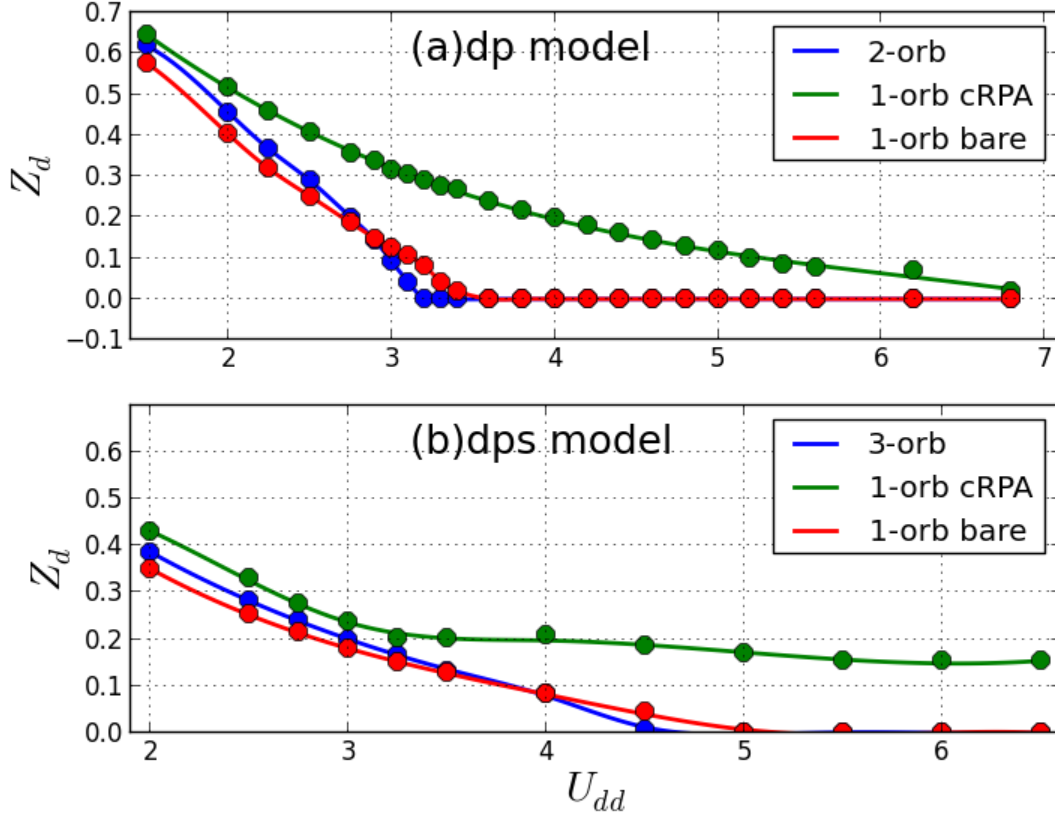


Figure 8.7: Comparison of the quasiparticle residue of the three scenarios varying U_{dd} in (a) dp model with $U_{pp} = 0.2U_{dd}$, $U_{pd} = 0.8U_{dd}$ and (b) dps model with $U_{pp} = U_{ss} = U_{ps} = 0.1U_{dd}$, $U_{pd} = 0.6U_{dd}$, $U_{ds} = 0.3U_{dd}$.

We also notice that “1-orb bare” is closer to the “2-orb/3-orb” scenario than the “1-orb cRPA” scenario, and in the range $U_{dd} \sim 2.7 - 3.4\text{eV}$, we observe dubious antiscreening effect in “2-orb” scenario if it is compared to “1-orb bare” scenario in dp model. We claim that this comparison is not physical in strict sense because low energy physics is not the same in these two scenarios. To demonstrate this, we investigated the behavior of occupancy of d orbital n_d in these two scenarios as shown in Fig. 8.8. One notices that there is a tiny difference of n_d in these two scenarios, showing that low-energy physics in d orbital channel is not the same. Besides, the onset point of “antiscreening” is concurrent with the crossing point in Fig. 8.8 where n_d in “1-orb bare” starts to outweigh that in “2-orb” scenario. From this we claim that the dubious “antiscreening” effect is caused by the difference in n_d and thus it is not a true effect here. However, these results establish the fact there is little screening on the most correlated orbital by the remaining orbitals in the dp and dps model and that it could be more accurate to factor in no screening at all rather than use cRPA as a predictive

mechanism. These results are also in agreement with those in Sec. 8.3.1 and suggest that in the strongly correlated regime with large hybridization between bands, the RPA bubble diagrams are not the most relevant ones when one is describing screening by non-correlated bands. It also suggests that in such cases, we should go beyond cRPA and consider a different screening mechanism, which is discussed in Sec. 8.3.3.

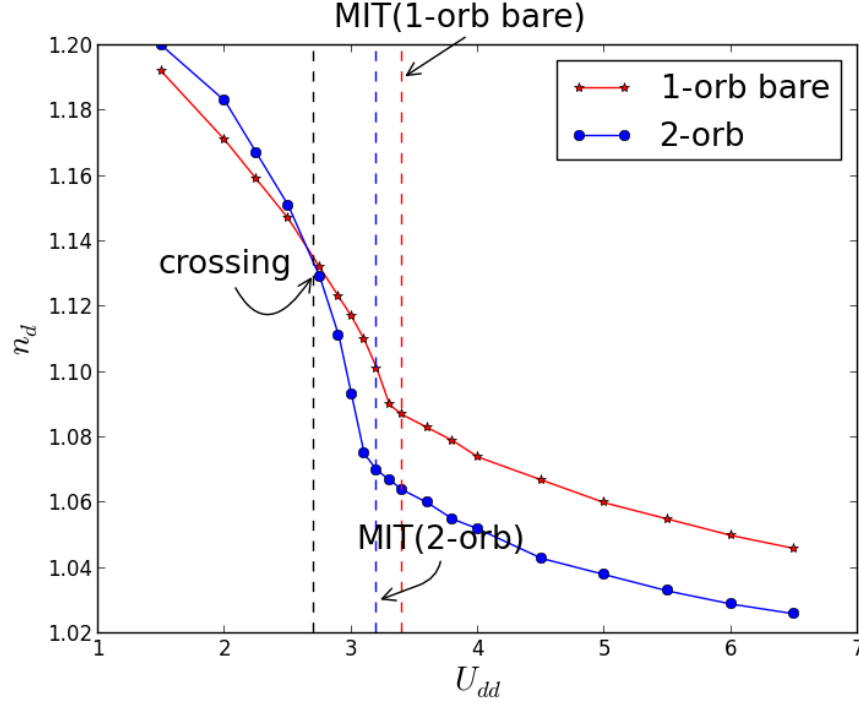


Figure 8.8: Occupation of d orbital (n_d) in dp model varying U_{dd} with $U_{pp} = 0.2U_{dd}$, $U_{pd} = 0.8U_{dd}$ of 1-orb bare and 2-orb scenario. MIT(1-orb bare) and MIT(2-orb) are transition points inferred from the quasiparticle residue results.

8.3.3 Estimation of Screening using Local Polarization

We shall now explain a new formulation for estimating the screening in strongly correlated systems. As we have shown, RPA-like non-interacting bubble diagrams are inadequate in explaining the screening present in these systems. In an effort to modify this formalism and yet preserve the mathematical simplicity of the method, we shall replace the non-interacting Polarization bubble used in RPA/cRPA with the full local Polarization bubble within DMFT approximation P^{Loc} . Similar to cRPA, we shall also define $P^{Loc} = P_d^{Loc} + P_r^{Loc}$, where P_d^{Loc} is the localized polarization in the d-subspace. We shall use this local Polarization to calculate the effective interaction in dp

model using the following equations

$$u^{cLoc} = V^{Loc}(\mathbf{1} - P_r^{Loc}V^{Loc})^{-1} \quad (8.13)$$

$$W^{Loc} = u^{cLoc}(\mathbf{1} - P_d^{Loc}u^{cLoc})^{-1} \quad (8.14)$$

The local polarization bubbles P^{Loc} here are constructed from the local two-band impurity charge and spin susceptibilities which are easily calculated using the CTQMC impurity solver [21]. These polarization inclusions include all the local interactions exactly and thus go far beyond the RPA-like prescription (For details on the exact procedure please refer to Appendix A). Note that this new procedure also obeys the Pauli exclusion principle, which is known to be a major failing of the cRPA method. [110]. Also note that u^{cLoc} and W^{Loc} give us the screened interaction parameters in all the orbital and spin channels separately. However as our major interest here is the interaction between electrons with opposite spins in the correlated (d) orbital, we shall concentrate only on this particular channel. Using this new procedure we estimate the new screened interaction parameters W^{Loc} and u^{cLoc} for two sets of parameters, one in the correlated metallic regime with $U_{dd} = 3.0$ and one in the Mott insulating regime with $U_{dd} = 4.5$. The results are shown in Fig. 8.9. The comparison between the static values of u_{dd}^{cRPA} and u_{dd}^{cLoc} is given in Table 8.2. As we can see, cRPA predicts vastly larger screening compared to our method (3 times larger in the metallic case and 52 times larger in the insulating case). We performed single orbital DMFT runs using the values predicted by our new method. We see that for $U_{dd} = 3.0$, our method still predicts slightly too much screening as evidenced by the enhanced metallicity of the "1-orb cLoc" run compared to the full 2-orb run. However the result is a large improvement on the cRPA result. For the insulating case, our method successfully reproduces the Mott transition, which cRPA fails completely in achieving. Our method yields a value of screened u_{dd} which is almost identical to the bare U_{dd} , again showing that there is very little inter-orbital screening near the MIT. We see that u_{dd}^{cLoc} has very little frequency dependence, which also negates the need for inclusion of more complicated frequency dependent u in our impurity solvers.

| bare U | u_{dd}^{cRPA} | screening($ 1 - \frac{u}{U} $) | u_{dd}^{cLoc} | screening |
|----------|-----------------|----------------------------------|-----------------|-----------|
| 3.00 | 2.25 | 25.0% | 2.76 | 8.00% |
| 4.50 | 2.91 | 35.3% | 4.47 | 0.67% |

Table 8.2: Comparison between static values of u_{dd}^{cRPA} and u_{dd}^{cLoc} for different values of bare U in the dp model.

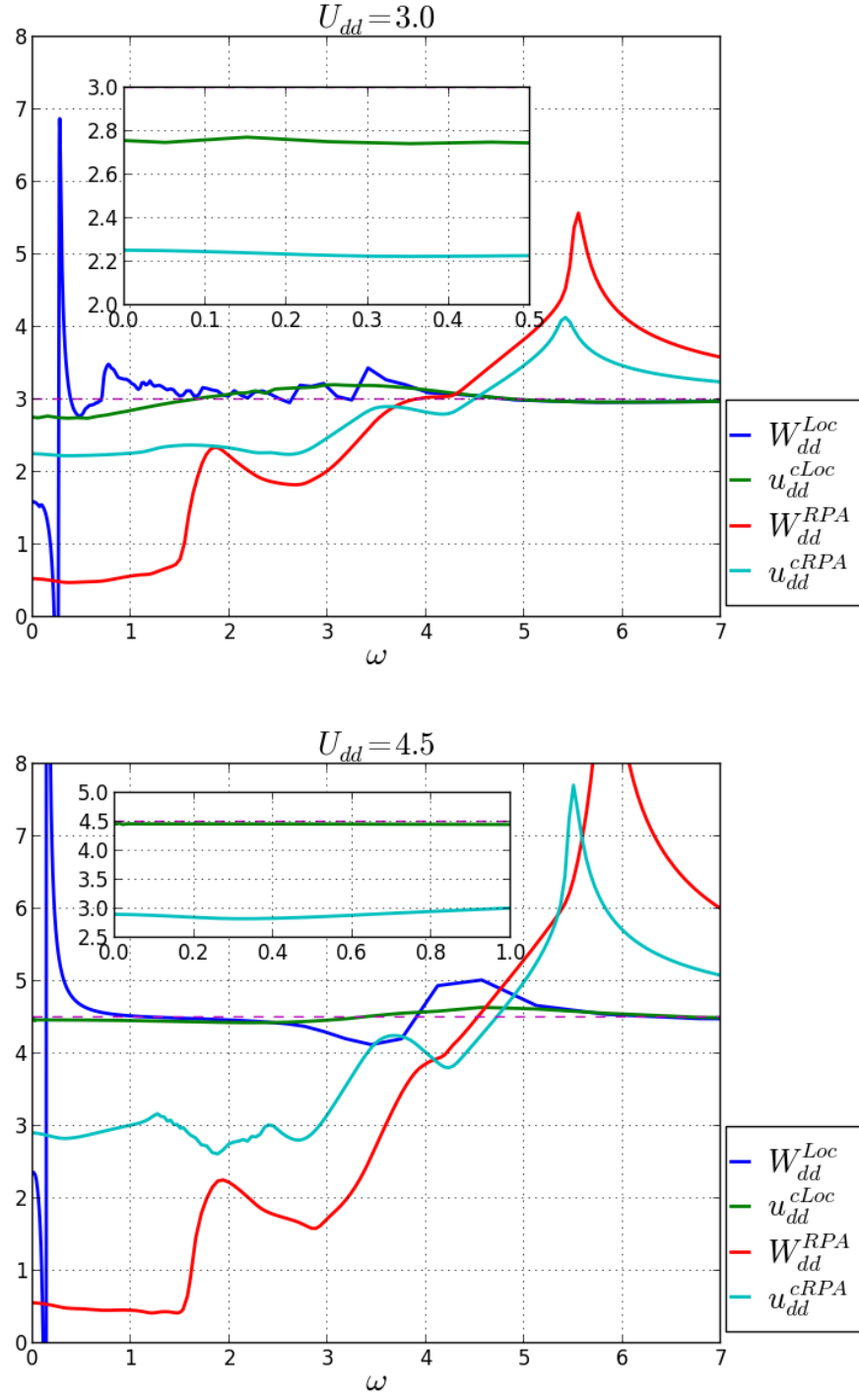


Figure 8.9: Plot showing the u^{cLoc} and W^{Loc} for $U_{dd} = 2.5$ (top) and $U_{dd} = 4.5$ (bottom) using the Local Polarization method. The RPA W^{RPA} and cRPA u^{cRPA} for both sets of parameters is also shown for comparison. Note: For both runs $U_{pp} = 0.2U_{dd}$; $U_{dp} = 0.8U_{dd}$. Inset shows a magnified portion of the plot for u^{cRPA} and u^{cLoc} near $\omega \rightarrow 0$.

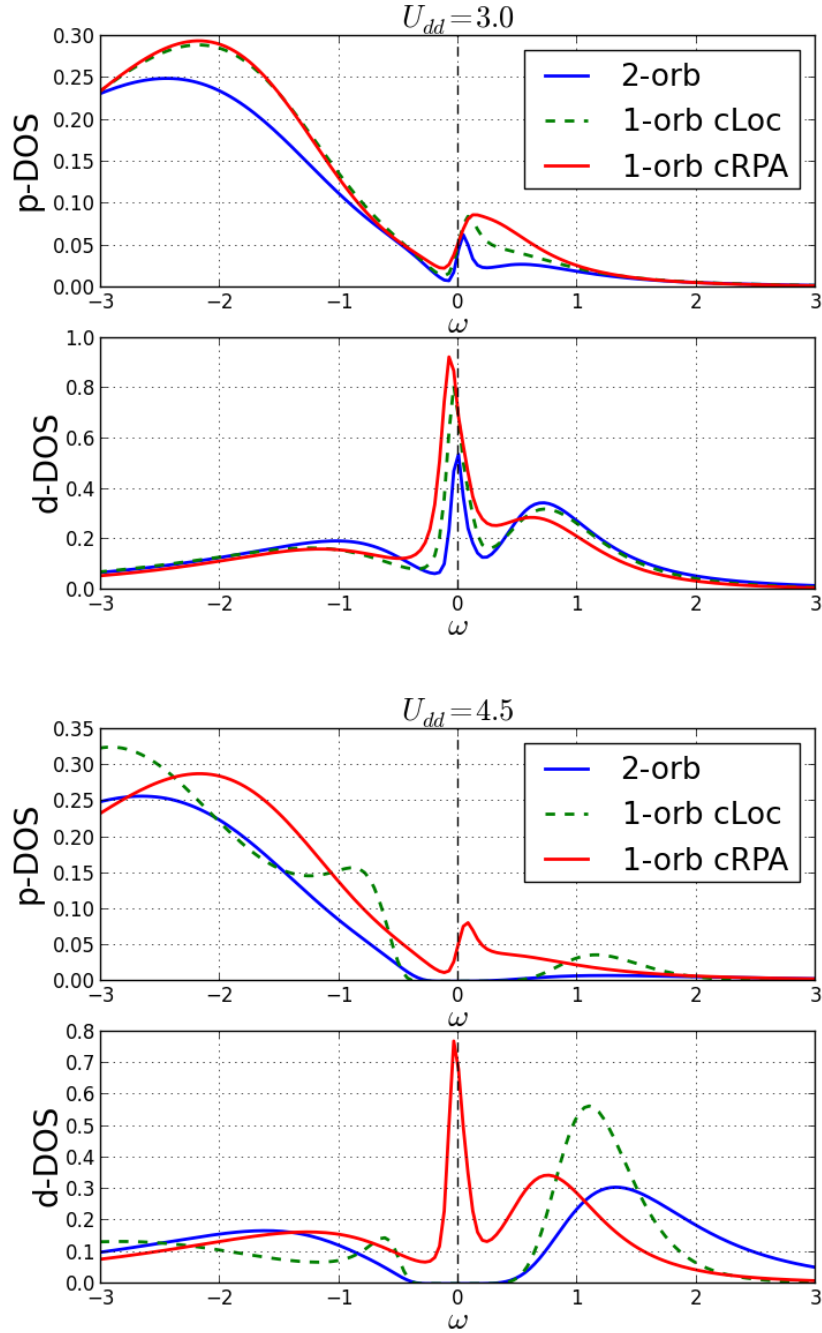


Figure 8.10: Plot showing the p orbital and d-orbital density of states using two-orbital DMFT (“2-orb”) and effective one-orbital DMFT using the Local Polarization method (“1-orb cLoc”) and cRPA (“1-orb cRPA”). The top two figures are for $U_{dd} = 2.5$ whereas the bottom two are for $U_{dd} = 4.5$.

The results for the fully screened W show that RPA had predicts a very small $W \sim 0.5$ for both the metallic and insulating cases, while our new method yields a static W_{dd}^{Loc} around 2.0, thus

showing much reduced screening in all channels . We also see that as we go to the insulating case, W_{dd}^{Loc} displays sharper features at very low energies and has a larger static value. This pronounced low-frequency behavior is characteristic of local Kondo-like screening processes which are seen for example in the magnetic susceptibility of γ Cerium [21]. Thus we see that our new prescription not only allows us to obtain values of u which are much more accurate in reproducing the spectra in strongly correlated regime when using effective one-orbital models but also show clearly that local screening is by far the most dominant contribution to screening processes in these systems. It is to be noted however that our method cannot be used for prediction of effective one-orbital parameters as we would need to perform multi-orbital DMFT in order to obtain the required susceptibilities to construct the local polarization. However, this procedure clearly shows that the physics of these systems is very different from RPA and that the local inclusions to the Polarization negate some of the overscreening inherent in cRPA. Therefore we believe that any predictive method should include some treatment of local processes in order to be successful and that by calculating more accurate Polarization functions, we may be able to successfully account for screening in strongly correlated systems.

8.4 Discussion and Conclusion

In this paper, we investigate the validity of cRPA as a method for predicting the Hubbard U for strongly correlated systems. To this end we study two different models, each of which have one strongly correlated band strongly hybridized with other weakly correlated band/s. We compare three scenarios derivable from the original lattice models and show that the full and the “1-orb bare” scenarios have very similar spectral functions for a wide region of interaction parameters. On the other hand, the cRPA “1-orb cRPA” scenario with an effective on-site Hubbard U calculated using cRPA has the tendency of being more metallic. We also compare the quasiparticle residue Z_d of the three scenarios and show that cRPA gets progressively worse as the on-site U_{dd} of the correlated band increases. These results together clearly show that cRPA has a pathological tendency to overestimate screening in strongly correlated systems. This, we believe, is simply due to the fact that the RPA-like bubble diagrams are not the exclusive leading order terms in the screening of local Coulomb repulsion. This systematic overscreening adds to other known deficiencies of cRPA, such as its violation of Pauli principle (note recent attempts to address this by Shinaoka et. al [110]). The extent of over-screening produced by cRPA is also hard to estimate and seems to depend on the exact dispersion of the system in question. This leads us to believe that such a mechanism is not suitable for predicting the effective screened Hubbard U for DMFT impurity solvers, except

as a lower bound for any other method. In addition, we show that in our models the interorbital interaction parameters such as U_{dp} and U_{pp} have very little screening effect in our model and that it is possible to stabilize a Mott Insulating phase without necessarily having large inter-orbital interactions. This is not compatible with the result obtained by Hansmann et. al [42] in which they find a finite U_{dp} is necessary to have a stable charge-transfer insulating phase. Our results seem to predict that $\epsilon_p - \epsilon_d$ and U_{dd} are the important parameters which define the physics of such systems, instead of U_{dp} . Though our models have a different dispersion from theirs, it would be interesting to see whether treating U_{dp} dynamically in their models would change their predictions. Finally we propose a new way to account for screening by using the local Polarization instead of the non-interacting Polarization bubble. We show that our new method predicts values of Hubbard U which are more accurate in reproducing the spectra of the full model, especially near the Mott Transition. Moreover the new W^{Loc} also shows reduced screening compared to RPA and also indicates that highly localized Kondo-like screening in the correlated orbital is the dominant screening process, while the W_{RPA} calculated using RPA fails as expected in capturing any such signatures.

Chapter 9

Conclusion

In this thesis we have studied various aspects of strongly correlated systems using DFT+DMFT. We started the thesis with a details of the theoretical building blocks of the DFT+DMFT method, namely Density functional Theory (DFT), Dynamical Mean Field Theory (DMFT) and the procedure to combine them into one comprehensive algorithm (DFT+DMFT). We then looked at some details of the impurity solver used in most of the DMFT simulations, the Continuous Time Quantum Monte Carlo (CTQMC) impurity solver. After building up the framework to be used in our simulations, we moved on to specific applications which have been the subject of my graduate research.

We start off in Chapter 6 by describing the simulations of the magnetic spectral function $S(q, \omega)$ for strongly correlated f-shell materials. We first outlined the theory for the calculation by describing the method to calculate the magnetic form factor and the dynamic magnetic susceptibility (which contain the q -dependence and the ω -dependence respectively) and to combine them into $S(q, \omega)$ under the single ion approximation.

We then used this computational machinery to study two important problems in condensed matter. We first studied the volume collapse transition in Cerium between α -Ce and γ -Ce. By confirming that the magnetic form factor $F_M(q)$ is identical across the transition, we confirmed that the f-electrons remain correlated in both phases, ruling out the promotional scenario for the transition. We then showed that the dynamic magnetic susceptibility shows an increase in the Kondo Temperature as we go across the transition into the α -phase. This showed that the hybridization and increase in Kondo temperature are important drivers for this transition. Finally we combined these two pieces to get the $S(q, \omega)$ for the transition which showed excellent agreement with neutron scattering experiments performed by Murani et. al [90].

Next we used the same technique to study the valence fluctuations in δ -Pu. The magnetic form factor obtained by us for the material not only achieved good agreement with experiments but also showed that we can understand the ground state of δ -Pu as a quantum mechanical mixture of different valence states. We then showed using the dynamic susceptibility that the compound does not show local moment behavior thus addressing the problem of missing magnetism in δ -Pu. We obtained a Kondo Temperature of $\sim 800\text{K}$ which explains how the moment in δ -Pu gets screened

the by Kondo screening cloud at low temperature. Finally we again obtained $S(q, \omega)$ which is in good agreement with neutron scattering experiments performed by Janoschek et al at Los Alamos National Lab.

The next problem we address in this dissertation is the decades-old problem of explaining the spin state transition in LaCoO_3 . In this system there has been a long debate about whether the Intermediate Spin ($S=1$) or the High Spin ($S=2$) state is dominant at high temperatures after the spin state transition has set in. In addition, there is also a non-concurrent metal-insulator transition that occurs in the compound at a different temperature scale. In our simulations, we used four different crystal structures (two physically present structures and two hypothetical structures) to isolate and study the effect of the (abnormally large) lattice thermal expansion and octahedral rotations in driving the spin state transition. Our simulations were successful in obtaining a spin state transition as a function of increasing temperature in the system. In addition we also obtained the non-concurrent metal-insulator transition at a completely different temperature than the spin state transition. By studying the four different structures, we ascertained that both thermal expansion and octahedral rotations aid the spin state transition by reducing the crystal field splitting in the compound. By using the spin state probabilities given to us by CTQMC, we showed that the high-temperature is a mixture of both the Intermediate and High spin states with both states gaining in probability as temperature is increased. We also showed that there are large valence fluctuations in the compound which make any description in the terms of spin states of the d^6 state inadequate. However we also see importantly that at the onset of the spin state transition, we see a jump in the occupation probability of the High spin multiplet. Interestingly we also noted that the metal-insulator transition is rather insensitive to the lattice parameters and happens at almost the same temperature for all four structures. Finally we used our state of the art Free Energy calculation algorithm to show that the electronic entropy gained by the spin state transition is enough to stabilize the Higher Spin state structure at high temperatures.

In chapter 8, we study the validity of the constrained Random Phase Approximation (cRPA) in estimating the screening of Hubbard U in strongly correlated systems with large hybridization between correlated and non-correlated orbitals. We showed, using simple yet general two and three orbital model hamiltonians that cRPA systematically underestimates screening in these systems, which can lead to pathological misrepresentation of the amount of correlations present. By comparing the simulations of the spectra and the quasiparticle residues of the full model and effective one orbital models with zero screening and screening estimated by cRPA, we showed that it is often more accurate to factor in no screening at all rather than the RPA-like screening used by cRPA. This showed that the RPA diagrams which are relevant in the $q \rightarrow 0$ limit, are not the most important

diagrams in local screening. In addition we show that the interorbital repulsion parameters which are fundamental to the screening diagrams in cRPA, have very little effect on the spectra thereby further calling into question the cRPA method, which seems to incorporate these parameters to overestimate screening to an unpredictable degree. Finally we address some of these concerns by postulating a new method to estimate screening which involves the full local polarization bubble (constructed using the local spin and charge susceptibilities) instead of the RPA polarization. Using this local polarization, which includes a much larger class of diagrams, we estimate the screening much more accurately than cRPA and are much more successful in reproducing spectra and the Mott-like metal-insulator transition in these models. The screened repulsion calculated using this method also shows very little frequency dependence, which seems to suggest that factoring in the frequency dependence of U is not very important in describing the physics of these systems.

Therefore in this dissertation, we have studied different aspects of the physics of strongly correlated systems using DFT+DMFT. We firmly believe that we have built up a robust framework which shall serve as an invaluable tool in studying the properties of real strongly correlated materials in time to come. It is hoped that by harnessing the full power of techniques like DMFT, we shall soon have the power to fully understand the physics of these notoriously difficult materials, which in turn will open up new horizons for mankind in engineering and technology.

Bibliography

- [1] M. Abbate, J. C. Fuggle, A. Fujimori, L. H. Tjeng, C. T. Chen, R. Potze, G. A. Sawatzky, H. Eisaki, and S. Uchida. Electronic structure and spin-state transition of LaCoO_3 . *Phys. Rev. B*, 47:16124–16130, Jun 1993.
- [2] Markus Aichhorn, Leonid Pourovskii, and Antoine Georges. Importance of electronic correlations for structural and magnetic properties of the iron pnictide superconductor LaFeAsO . *Phys. Rev. B*, 84:054529, Aug 2011.
- [3] J. W. Allen and Richard M. Martin. Kondo volume collapse and the $\gamma \rightarrow \alpha$ transition in cerium. *Phys. Rev. Lett.*, 49(15):1106–1110, Oct 1982.
- [4] B. Amadon, S. Biermann, A. Georges, and F. Aryasetiawan. The $\alpha - \gamma$ transition of cerium is entropy driven. *Phys. Rev. Lett.*, 96(6):066402, Feb 2006.
- [5] B. Amadon, F. Lechermann, A. Georges, F. Jollet, T. O. Wehling, and A. I. Lichtenstein. Plane-wave based electronic structure calculations for correlated materials using dynamical mean-field theory and projected local orbitals. *Phys. Rev. B*, 77:205112, May 2008.
- [6] Bernard Amadon, Thomas Applencourt, and Fabien Bruneval. Screened coulomb interaction calculations: crpa implementation and applications to dynamical screening and self-consistency in uranium dioxide and cerium. *Phys. Rev. B*, 89:125110, Mar 2014.
- [7] P. W. Anderson. Localized magnetic states in metals. *Phys. Rev.*, 124:41–53, Oct 1961.
- [8] P. W. Anderson and G. Yuval. Exact results in the kondo problem: Equivalence to a classical one-dimensional coulomb gas. *Phys. Rev. Lett.*, 23:89–92, Jul 1969.
- [9] N. Andrei, K. Furuya, and J. H. Lowenstein. Solution of the kondo problem. *Rev. Mod. Phys.*, 55:331–402, Apr 1983.
- [10] V. I. Anisimov and O. Gunnarsson. Density-functional calculation of effective coulomb interactions in metals. *Phys. Rev. B*, 43:7570–7574, Apr 1991.
- [11] V. I. Anisimov, D. E. Kondakov, A. V. Kozhevnikov, I. A. Nekrasov, Z. V. Pchelkina, J. W. Allen, S.-K. Mo, H.-D. Kim, P. Metcalf, S. Suga, A. Sekiyama, G. Keller, I. Leonov, X. Ren, and

- D. Vollhardt. Full orbital calculation scheme for materials with strongly correlated electrons. *Phys. Rev. B*, 71:125119, Mar 2005.
- [12] Vladimir I Anisimov, F Aryasetiawan, and A I Lichtenstein. First-principles calculations of the electronic structure and spectra of strongly correlated systems: the lda + u method. *Journal of Physics: Condensed Matter*, 9(4):767, 1997.
- [13] F. Aryasetiawan, M. Imada, A. Georges, G. Kotliar, S. Biermann, and A. I. Lichtenstein. Frequency-dependent local interactions and low-energy effective models from electronic structure calculations. *Phys. Rev. B*, 70:195104, Nov 2004.
- [14] F. Aryasetiawan, K. Karlsson, O. Jepsen, and U. Schönberger. Calculations of hubbard u from first-principles. *Phys. Rev. B*, 74:125106, Sep 2006.
- [15] P. Augustinský, V. Křápek, and J. Kuneš. Doping induced spin state transition in LaCoO_3 : Dynamical mean-field study. *Phys. Rev. Lett.*, 110:267204, Jun 2013.
- [16] Robert A. Bari and J. Sivardière. Low-spin-high-spin transitions in transition-metal-ion compounds. *Phys. Rev. B*, 5:4466–4471, Jun 1972.
- [17] V. G. Bhide, D. S. Rajoria, G. Rama Rao, and C. N. R. Rao. Mössbauer studies of the high-spin-low-spin equilibria and the localized-collective electron transition in LaCoO_3 . *Phys. Rev. B*, 6:1021–1032, Aug 1972.
- [18] N. E. Bickers, D. L. Cox, and J. W. Wilkins. Self-consistent large- n expansion for normal-state properties of dilute magnetic alloys. *Phys. Rev. B*, 36:2036–2079, Aug 1987.
- [19] P. Blaha, K. Schwarz, G. K. H. Madsen, D. Kvasnicka, and J. Luitz. *WIEN2K, An Augmented Plane Wave + Local Orbitals Program for Calculating Crystal Properties*. Karlheinz Schwarz, Techn. Universität Wien, Austria, 2001.
- [20] B. Chakrabarti, T. Birol, and K. Haule. Role of Entropy and Structural Parameters in the Spin State Transition of LaCoO_3 . *ArXiv e-prints*, May 2016.
- [21] B. Chakrabarti, M. E. Pezzoli, G. Sordi, K. Haule, and G. Kotliar. α - γ transition in cerium: Magnetic form factor and dynamic magnetic susceptibility in dynamical mean-field theory. *Phys. Rev. B*, 89:125113, Mar 2014.
- [22] Woo Seok Choi, Ji-Hwan Kwon, Hyoungjeen Jeon, Jorge E. Hamann-Borrero, Abdullah Radi, Sebastian Macke, Ronny Sutarto, Feizhou He, George A. Sawatzky, Vladimir Hinkov, Miyoung

- Kim, and Ho Nyung Lee. Strain-induced spin states in atomically ordered cobaltites. *Nano Letters*, 12(9):4966–4970, 2012. PMID: 22889011.
- [23] Matteo Cococcioni and Stefano de Gironcoli. Linear response approach to the calculation of the effective interaction parameters in the LDA + U method. *Phys. Rev. B*, 71:035105, Jan 2005.
- [24] Piers Coleman. New approach to the mixed-valence problem. *Phys. Rev. B*, 29:3035–3044, Mar 1984.
- [25] B. Coqblin and A. Blandin. *Advan. Phys.*, page 281, 1968.
- [26] B N Cox, M A Coulthard, and P Lloyd. A calculation of the coulomb correlation energy, U , for transition metals in hubbard’s model. *Journal of Physics F: Metal Physics*, 4(6):807, 1974.
- [27] L. Craco and E. Müller-Hartmann. Dynamical correlations across the spin-state transition in LaCoO_3 . *Phys. Rev. B*, 77:045130, Jan 2008.
- [28] M. T. Czyżyk and G. A. Sawatzky. Local-density functional and on-site correlations: The electronic structure of La_2CuO_4 and LaCuO_3 . *Phys. Rev. B*, 49:14211–14228, May 1994.
- [29] A M Durand, D P Belanger, T J Hamil, F Ye, S Chi, J A Fernandez-Baca, C H Booth, Y Abdollahian, and M Bhat. The unusual magnetism of nanoparticle LaCoO_3 . *Journal of Physics: Condensed Matter*, 27(17):176003, 2015.
- [30] R. Eder. Spin-state transition in LaCoO_3 by variational cluster approximation. *Phys. Rev. B*, 81:035101, Jan 2010.
- [31] Suzanne R. English, J. Wu, and C. Leighton. Thermally excited spin-disorder contribution to the resistivity of LaCoO_3 . *Phys. Rev. B*, 65:220407, Jun 2002.
- [32] J. W. Freeland, J. X. Ma, and J. Shi. Erratum: ferromagnetic spin-correlations in strained LaCoO_3 thin films [appl. phys. lett.93, 212501 (2008)]. *Applied Physics Letters*, 94(12):–, 2009.
- [33] D. Fuchs, E. Arac, C. Pinta, S. Schuppler, R. Schneider, and H. v. Löhneysen. Tuning the magnetic properties of LaCoO_3 thin films by epitaxial strain. *Phys. Rev. B*, 77:014434, Jan 2008.
- [34] D. Fuchs, L. Dieterle, E. Arac, R. Eder, P. Adelmann, V. Eyert, T. Kopp, R. Schneider, D. Gerthsen, and H. v. Löhneysen. Suppression of the ferromagnetic state in LaCoO_3 films by rhombohedral distortion. *Phys. Rev. B*, 79:024424, Jan 2009.

- [35] D. Fuchs, C. Pinta, T. Schwarz, P. Schweiss, P. Nagel, S. Schuppler, R. Schneider, M. Merz, G. Roth, and H. v. Löhneysen. Ferromagnetic order in epitaxially strained LaCoO_3 thin films. *Phys. Rev. B*, 75:144402, Apr 2007.
- [36] Antoine Georges, Gabriel Kotliar, Werner Krauth, and Marcelo J. Rozenberg. Dynamical mean-field theory of strongly correlated fermion systems and the limit of infinite dimensions. *Rev. Mod. Phys.*, 68:13–125, Jan 1996.
- [37] Antoine Georges, Gabriel Kotliar, Werner Krauth, and Marcelo J. Rozenberg. Dynamical mean-field theory of strongly correlated fermion systems and the limit of infinite dimensions. *Rev. Mod. Phys.*, 68:13–125, Jan 1996.
- [38] Paolo Giannozzi, Stefano Baroni, Nicola Bonini, Matteo Calandra, Roberto Car, Carlo Cavazzoni, Davide Ceresoli, Guido L Chiarotti, Matteo Cococcioni, Ismaila Dabo, Andrea Dal Corso, Stefano de Gironcoli, Stefano Fabris, Guido Fratesi, Ralph Gebauer, Uwe Gerstmann, Christos Gougoussis, Anton Kokalj, Michele Lazzeri, Layla Martin-Samos, Nicola Marzari, Francesco Mauri, Riccardo Mazzarello, Stefano Paolini, Alfredo Pasquarello, Lorenzo Paulatto, Carlo Sbraccia, Sandro Scandolo, Gabriele Sclauszero, Ari P Seitsonen, Alexander Smogunov, Paolo Umari, and Renata M Wentzcovitch. Quantum espresso: a modular and open-source software project for quantum simulations of materials. *Journal of Physics: Condensed Matter*, 21(39):395502, 2009.
- [39] V. Gnezdilov, V. Fomin, A. V. Yermenko, K.-Y. Choi, Yu. Pashkevich, P. Lemmens, S. Shiryaev, G. Bychkov, and S. Barilo. Low-temperature mixed spin state of co^{3+} in LaCoO_3 evidenced from jahn-teller lattice distortions. *Low Temperature Physics*, 32(2):162–168, 2006.
- [40] X. Gonze, B. Amadon, P.-M. Anglade, J.-M. Beuken, F. Bottin, P. Boulanger, F. Bruneval, D. Caliste, R. Caracas, M. Ct, T. Deutsch, L. Genovese, Ph. Ghosez, M. Giantomassi, S. Goedecker, D.R. Hamann, P. Hermet, F. Jollet, G. Jomard, S. Leroux, M. Mancini, S. Mazevet, M.J.T. Oliveira, G. Onida, Y. Pouillon, T. Rangel, G.-M. Rignanese, D. Sangalli, R. Shaltaf, M. Torrent, M.J. Verstraete, G. Zerah, and J.W. Zwanziger. Abinit: First-principles approach to material and nanosystem properties. *Computer Physics Communications*, 180(12):2582 – 2615, 2009. 40 {YEARS} {OF} CPC: A celebratory issue focused on quality software for high performance, grid and novel computing architectures.
- [41] Emanuel Gull, Andrew J. Millis, Alexander I. Lichtenstein, Alexey N. Rubtsov, Matthias

- Troyer, and Philipp Werner. Continuous-time monte carlo methods for quantum impurity models. *Rev. Mod. Phys.*, 83:349–404, May 2011.
- [42] P Hansmann, N Parragh, A Toschi, G Sangiovanni, and K Held. Importance of d ? p coulomb interaction for high t c cuprates and other oxides. *New Journal of Physics*, 16(3):033009, 2014.
- [43] Kristjan Haule. Quantum monte carlo impurity solver for cluster dynamical mean-field theory and electronic structure calculations with adjustable cluster base. *Phys. Rev. B*, 75:155113, Apr 2007.
- [44] Kristjan Haule. Quantum monte carlo impurity solver for cluster dynamical mean-field theory and electronic structure calculations with adjustable cluster base. *Phys. Rev. B*, 75(15):155113, 2007.
- [45] Kristjan Haule. Quantum monte carlo impurity solver for cluster dynamical mean-field theory and electronic structure calculations with adjustable cluster base. *Phys. Rev. B*, 75(15):155113, 2007.
- [46] Kristjan Haule. Quantum monte carlo impurity solver for cluster dynamical mean-field theory and electronic structure calculations with adjustable cluster base. *Phys. Rev. B*, 75:155113, Apr 2007.
- [47] Kristjan Haule. Exact double counting in combining the dynamical mean field theory and the density functional theory. *Phys. Rev. Lett.*, 115:196403, Nov 2015.
- [48] Kristjan Haule and Turan Birol. Free energy from stationary implementation of the DFT + DMFT functional. *Phys. Rev. Lett.*, 115:256402, Dec 2015.
- [49] Kristjan Haule, Turan Birol, and Gabriel Kotliar. Covalency in transition-metal oxides within all-electron dynamical mean-field theory. *Phys. Rev. B*, 90:075136, Aug 2014.
- [50] Kristjan Haule, Viktor Oudovenko, Sergej Y. Savrasov, and Gabriel Kotliar. The $\alpha \rightarrow \gamma$ transition in ce: A theoretical view from optical spectroscopy. *Phys. Rev. Lett.*, 94(3):036401, Jan 2005.
- [51] Kristjan Haule, Chuck-Hou Yee, and Kyoo Kim. Dynamical mean-field theory within the full-potential methods: Electronic structure of *ceirin*₅ , *cecoin*₅ , and *cerhin*₅. *Phys. Rev. B*, 81(19):195107, May 2010.

- [52] Kristjan Haule, Chuck-Hou Yee, and Kyoo Kim. Dynamical mean-field theory within the full-potential methods: Electronic structure of $\text{ceir}_{\text{in}_5}$, $\text{ceco}_{\text{in}_5}$, and cer_{in_5} . *Phys. Rev. B*, 81:195107, May 2010.
- [53] Kristjan Haule, Chuck-Hou Yee, and Kyoo Kim. Dynamical mean-field theory within the full-potential methods: Electronic structure of $\text{ceir}_{\text{in}_5}$, $\text{ceco}_{\text{in}_5}$, and cer_{in_5} . *Phys. Rev. B*, 81:195107, May 2010.
- [54] Kristjan Haule, Chuck-Hou Yee, and Kyoo Kim. Dynamical mean-field theory within the full-potential methods: Electronic structure of $\text{ceir}_{\text{in}_5}$, $\text{ceco}_{\text{in}_5}$, and cer_{in_5} . *Phys. Rev. B*, 81:195107, May 2010.
- [55] M. W. Haverkort, Z. Hu, J. C. Cezar, T. Burnus, H. Hartmann, M. Reuther, C. Zobel, T. Lorenz, A. Tanaka, N. B. Brookes, H. H. Hsieh, H.-J. Lin, C. T. Chen, and L. H. Tjeng. Spin state transition in LaCoO_3 studied using soft x-ray absorption spectroscopy and magnetic circular dichroism. *Phys. Rev. Lett.*, 97:176405, Oct 2006.
- [56] R. H. Heffner, G. D. Morris, M. J. Fluss, B. Chung, S. McCall, D. E. MacLaughlin, L. Shu, K. Ohishi, E. D. Bauer, J. L. Sarrao, W. Higemoto, and T. U. Ito. Limits for ordered magnetism in Pu from muon spin rotation spectroscopy. *Phys. Rev. B*, 73:094453, Mar 2006.
- [57] R.R. Heikes, R.C. Miller, and R. Mazelsky. Magnetic and electrical anomalies in LaCoO_3 . *Physica*, 30(8):1600 – 1608, 1964.
- [58] K. Held. Electronic Structure Calculations using Dynamical Mean Field Theory. *eprint arXiv:cond-mat/0511293*, November 2005.
- [59] K. Held, A. K. McMahan, and R. T. Scalettar. Cerium volume collapse: Results from the merger of dynamical mean-field theory and local density approximation. *Phys. Rev. Lett.*, 87:276404, Dec 2001.
- [60] A. Herklotz, A. D. Rata, L. Schultz, and K. Dörr. Reversible strain effect on the magnetization of LaCoO_3 films. *Phys. Rev. B*, 79:092409, Mar 2009.
- [61] J. E. Hirsch and R. M. Fye. Monte carlo method for magnetic impurities in metals. *Phys. Rev. Lett.*, 56:2521–2524, Jun 1986.
- [62] Anders Hjelm, Joakim Trygg, Olle Eriksson, Börje Johansson, and John Wills. Field-induced magnetism in itinerant f -electron systems: U , Pu , and Ce . *Phys. Rev. B*, 50:4332–4340, Aug 1994.

- [63] P. Hohenberg and W. Kohn. Inhomogeneous Electron Gas. *Physical Review*, 136:864–871, November 1964.
- [64] Han Hsu, Peter Blaha, Renata M. Wentzcovitch, and C. Leighton. Cobalt spin states and hyperfine interactions in LaCoO_3 investigated by $\text{LDA}+u$ calculations. *Phys. Rev. B*, 82:100406, Sep 2010.
- [65] Mark S. Hybertsen, Michael Schlüter, and Niels E. Christensen. Calculation of coulomb-interaction parameters for La_2CuO_4 using a constrained-density-functional approach. *Phys. Rev. B*, 39:9028–9041, May 1989.
- [66] Masatoshi Imada, Atsushi Fujimori, and Yoshinori Tokura. Metal-insulator transitions. *Rev. Mod. Phys.*, 70:1039–1263, Oct 1998.
- [67] Masayuki Itoh, Ikuomi Natori, Satoshi Kubota, and Kiyoichiro Motoya. Spin-glass behavior and magnetic phase diagram of $\text{La}_{1-x}\text{Sr}_x\text{CoO}_3$ ($0 \leq x \leq 0.5$) studied by magnetization measurements. *Journal of the Physical Society of Japan*, 63(4):1486–1493, 1994.
- [68] Marc Janoschek, Pinaki Das, Bismayan Chakrabarti, Douglas L. Abernathy, Mark D. Lumsden, John M. Lawrence, Joe D. Thompson, Gerard H. Lander, Jeremy N. Mitchell, Scott Richmond, Mike Ramos, Frans Trouw, Jian-Xin Zhu, Kristjan Haule, Gabriel Kotliar, and Eric D. Bauer. The valence-fluctuating ground state of plutonium. *Science Advances*, 1(6), 2015.
- [69] Mark Jarrell and J.E. Gubernatis. Bayesian inference and the analytic continuation of imaginary-time quantum monte carlo data. *Physics Reports*, 269(3):133 – 195, 1996.
- [70] B. Johansson. The $\alpha - \gamma$ transition in cerium is a mott transition. *Philosophical Magazine.*, 30:469, 1974.
- [71] R. O. Jones and O. Gunnarsson. The density functional formalism, its applications and prospects. *Rev. Mod. Phys.*, 61:689–746, Jul 1989.
- [72] V. Křápek, P. Novák, J. Kuneš, D. Novoselov, Dm. M. Korotin, and V. I. Anisimov. Spin state transition and covalent bonding in LaCoO_3 . *Phys. Rev. B*, 86:195104, Nov 2012.
- [73] R. F. Klie, J. C. Zheng, Y. Zhu, M. Varela, J. Wu, and C. Leighton. Direct measurement of the low-temperature spin-state transition in LaCoO_3 . *Phys. Rev. Lett.*, 99:047203, Jul 2007.
- [74] W. Kohn and L. J. Sham. Self-consistent equations including exchange and correlation effects. *Phys. Rev.*, 140:A1133–A1138, Nov 1965.

- [75] M. A. Korotin, S. Yu. Ezhov, I. V. Solovyev, V. I. Anisimov, D. I. Khomskii, and G. A. Sawatzky. Intermediate-spin state and properties of LaCoO_3 . *Phys. Rev. B*, 54:5309–5316, Aug 1996.
- [76] D.C. Koskenmaki and Jr. K.A. Gschneidner. *Cerium, Handbook on the Physics and Chemistry of Rare Earths, Vol 1, KA. Gschneidner, Jr. and L. Eyring, Ed.* Elsevier, North-Holland, Amsterdam, 1978.
- [77] G. Kresse and J. Hafner. *Ab initio* molecular dynamics for liquid metals. *Phys. Rev. B*, 47:558–561, Jan 1993.
- [78] M. Kriener, C. Zobel, A. Reichl, J. Baier, M. Cwik, K. Berggold, H. Kierspel, O. Zabara, A. Freimuth, and T. Lorenz. Structure, magnetization, and resistivity of $\text{La}_{1-x}\text{M}_x\text{CoO}_3$ ($m = \text{Ca, sr, and ba}$). *Phys. Rev. B*, 69:094417, Mar 2004.
- [79] Tôru Kyômen, Yoshinori Asaka, and Mitsuru Itoh. Thermodynamical analysis of spin-state transitions in LaCoO_3 : Negative energy of mixing to assist thermal excitation to the high-spin excited state. *Phys. Rev. B*, 71:024418, Jan 2005.
- [80] J. C. Lashley, J. Singleton, A. Migliori, J. B. Betts, R. A. Fisher, J. L. Smith, and R. J. McQueeney. Experimental electronic heat capacities of α - and δ -plutonium: Heavy-fermion physics in an element. *Phys. Rev. Lett.*, 91:205901, Nov 2003.
- [81] M. Lavagna, C. Lacroix, and M. Cyrot. Volume collapse in the kondo lattice. *Physics Letters A*, 90(4):210 – 212, 1982.
- [82] F. Lechermann, A. Georges, A. Poteryaev, S. Biermann, M. Posternak, A. Yamasaki, and O. K. Andersen. Dynamical mean-field theory using wannier functions: A flexible route to electronic structure calculations of strongly correlated materials. *Phys. Rev. B*, 74:125120, Sep 2006.
- [83] C. A. Marianetti, K. Haule, G. Kotliar, and M. J. Fluss. Electronic coherence in δ -pu: A dynamical mean-field theory study. *Phys. Rev. Lett.*, 101:056403, Aug 2008.
- [84] G. Maris, Y. Ren, V. Volotchaev, C. Zobel, T. Lorenz, and T. T. M. Palstra. Evidence for orbital ordering in LaCoO_3 . *Phys. Rev. B*, 67:224423, Jun 2003.
- [85] S. Masuda, M. Aoki, Y. Harada, H. Hirohashi, Y. Watanabe, Y. Sakisaka, and H. Kato. Observation of anomalously enhanced satellite in metastable atom electron spectrum of LaCoO_3 . *Phys. Rev. Lett.*, 71:4214–4217, Dec 1993.

- [86] A. K. McMahan, K. Held, and R. T. Scalettar. Thermodynamic and spectral properties of compressed ce calculated using a combined local-density approximation and dynamical mean-field theory. *Phys. Rev. B*, 67:075108, Feb 2003.
- [87] A. K. McMahan, Richard M. Martin, and S. Satpathy. Calculated effective hamiltonian for la_2cuo_4 and solution in the impurity anderson approximation. *Phys. Rev. B*, 38:6650–6666, Oct 1988.
- [88] Takashi Miyake and F. Aryasetiawan. Screened coulomb interaction in the maximally localized wannier basis. *Phys. Rev. B*, 77:085122, Feb 2008.
- [89] Takashi Miyake, Kazuma Nakamura, Ryotaro Arita, and Masatoshi Imada. Comparison of ab initio low-energy models for lafepo, lafeaso, bafe2as2, lifeas, fese, and fete: Electron correlation and covalency. *Journal of the Physical Society of Japan*, 79(4):044705, 2010.
- [90] A. P. Murani, S. J. Levett, and J. W. Taylor. Magnetic form factor of α -ce: Towards understanding the magnetism of cerium. *Phys. Rev. Lett.*, 95(25):256403, Dec 2005.
- [91] A. P. Murani, R. Raphael, Z. A. Bowden, and R. S. Eccleston. Kondo resonance energies in cepd_3 . *Phys. Rev. B*, 53:8188–8191, Apr 1996.
- [92] A. P. Murani, A. D. Taylor, R. Osborn, and Z. A. Bowden. Evolution of the spin-orbit excitation with increasing kondo energy in $\text{cein}_{3-x}\text{sn}_x$. *Phys. Rev. B*, 48:10606–10609, Oct 1993.
- [93] C. S. Naiman, R. Gilmore, B. DiBartolo, A. Linz, and R. Santoro. Interpretation of the magnetic properties of lacoo_3 . *Journal of Applied Physics*, 36(3):1044–1045, 1965.
- [94] I. A. Nekrasov, S. V. Streltsov, M. A. Korotin, and V. I. Anisimov. Influence of rare-earth ion radii on the low-spin to intermediate-spin state transition in lanthanide cobaltite perovskites: lacoo_3 versus hocoo_3 . *Phys. Rev. B*, 68:235113, Dec 2003.
- [95] Zoltán Németh, András Szabó, Karel Knížek, Marcin Sikora, Roman Chernikov, Norbert Sas, Csilla Bogdán, Dénes Lajos Nagy, and György Vankó. Microscopic origin of the magnetoelectronic phase separation in sr-doped lacoo_3 . *Phys. Rev. B*, 88:035125, Jul 2013.
- [96] F. Nilsson, R. Sakuma, and F. Aryasetiawan. *Ab initio* calculations of the hubbard u for the early lanthanides using the constrained random-phase approximation. *Phys. Rev. B*, 88:125123, Sep 2013.

- [97] S. K. Pandey, Ashwani Kumar, S. Patil, V. R. R. Medicherla, R. S. Singh, K. Maiti, D. Prabhakaran, A. T. Boothroyd, and A. V. Pimpale. Investigation of the spin state of co in LaCoO_3 at room temperature: *Ab initio* calculations and high-resolution photoemission spectroscopy of single crystals. *Phys. Rev. B*, 77:045123, Jan 2008.
- [98] Hyowon Park, Kristjan Haule, and Gabriel Kotliar. Magnetic excitation spectra in BaFe_2As_2 : A two-particle approach within a combination of the density functional theory and the dynamical mean-field theory method. *Phys. Rev. Lett.*, 107:137007, Sep 2011.
- [99] Maria Elisabetta Pezzoli, Kristjan Haule, and Gabriel Kotliar. Neutron magnetic form factor in strongly correlated materials. *Phys. Rev. Lett.*, 106:016403, Jan 2011.
- [100] A. Podlesnyak, S. Streule, J. Mesot, M. Medarde, E. Pomjakushina, K. Conder, A. Tanaka, M. W. Haverkort, and D. I. Khomskii. Spin-state transition in LaCoO_3 : Direct neutron spectroscopic evidence of excited magnetic states. *Phys. Rev. Lett.*, 97:247208, Dec 2006.
- [101] Jorge Quintanilla and Chris Hooley. The strong-correlations puzzle. *Physics World*, 22(06):32, 2009.
- [102] P. M. Raccah and J. B. Goodenough. First-order localized-electron \rightleftharpoons collective-electron transition in LaCoO_3 . *Phys. Rev.*, 155:932–943, Mar 1967.
- [103] P. G. Radaelli and S.-W. Cheong. Structural phenomena associated with the spin-state transition in LaCoO_3 . *Phys. Rev. B*, 66:094408, Sep 2002.
- [104] James M. Rondinelli and Nicola A. Spaldin. Structural effects on the spin-state transition in epitaxially strained LaCoO_3 films. *Phys. Rev. B*, 79:054409, Feb 2009.
- [105] Z. Ropka and R. J. Radwanski. $5d$ term origin of the excited triplet in LaCoO_3 . *Phys. Rev. B*, 67:172401, May 2003.
- [106] T. Saitoh, T. Mizokawa, A. Fujimori, M. Abbate, Y. Takeda, and M. Takano. Electronic structure and temperature-induced paramagnetism in LaCoO_3 . *Phys. Rev. B*, 55:4257–4266, Feb 1997.
- [107] R. Sakuma and F. Aryasetiawan. First-principles calculations of dynamical screened interactions for the transition metal oxides MO ($M=\text{Mn, Fe, Co, Ni}$). *Phys. Rev. B*, 87:165118, Apr 2013.

- [108] Bi-Ching Shih, Tesfaye A. Abtew, Xun Yuan, Wenqing Zhang, and Peihong Zhang. Screened coulomb interactions of localized electrons in transition metals and transition-metal oxides. *Phys. Rev. B*, 86:165124, Oct 2012.
- [109] J. H. Shim, K. Haule, and G. Kotliar. Fluctuating valence in a correlated solid and the anomalous properties of [dgr]-plutonium. *Nature*, 446(7135):513–516, 03 2007.
- [110] Hiroshi Shinaoka, Matthias Troyer, and Philipp Werner. Accuracy of downfolding based on the constrained random-phase approximation. *Phys. Rev. B*, 91:245156, Jun 2015.
- [111] David. J Singh and Lars Nordstron. Planewaves, pseudopotentials, and the lapw method. 2006.
- [112] M. Springer and F. Aryasetiawan. Frequency-dependent screened interaction in ni within the random-phase approximation. *Phys. Rev. B*, 57:4364–4368, Feb 1998.
- [113] C. Stassis, C.-K. Loong, G.R. Kline, O.D. McMasters, and K.A. Gschneider. Field induced magnetic form factor of γ -ce. *J. Appl. Phys.*, 49:2113–2114, Mar 1978.
- [114] Svein Stølen, Fredrik Grønvd, Hendrik Brinks, Tooru Atake, and Hideki Mori. Energetics of the spin transition in LaCoO_3 . *Phys. Rev. B*, 55:14103–14106, Jun 1997.
- [115] N. Sundaram, Y. Jiang, I. E. Anderson, D. P. Belanger, C. H. Booth, F. Bridges, J. F. Mitchell, Th. Proffen, and H. Zheng. Local structure of $\text{La}_{1-x}\text{Sr}_x\text{CoO}_3$ determined from exafs and neutron pair distribution function studies. *Phys. Rev. Lett.*, 102:026401, Jan 2009.
- [116] G Thornton, B.c Tofield, and A.W Hewat. A neutron diffraction study of LaCoO_3 in the temperature range 4.2 t j 1248 k. *Journal of Solid State Chemistry*, 61(3):301–307, 1986.
- [117] G. van der Laan and M. Taguchi. Valence fluctuations in thin films and the α and δ phases of pu metal determined by 4f core-level photoemission calculations. *Phys. Rev. B*, 82:045114, Jul 2010.
- [118] Loïg Vaugier, Hong Jiang, and Silke Biermann. Hubbard u and hund exchange j in transition metal oxides: Screening versus localization trends from constrained random phase approximation. *Phys. Rev. B*, 86:165105, Oct 2012.
- [119] T. Vogt, J. A. Hriljac, N. C. Hyatt, and P. Woodward. Pressure-induced intermediate-to-low spin state transition in LaCoO_3 . *Phys. Rev. B*, 67:140401, Apr 2003.

- [120] Xin Wang, M. J. Han, Luca de' Medici, Hyowon Park, C. A. Marianetti, and Andrew J. Millis. Covalency, double-counting, and the metal-insulator phase diagram in transition metal oxides. *Phys. Rev. B*, 86:195136, Nov 2012.
- [121] Philipp Werner, Armin Comanac, Luca de' Medici, Matthias Troyer, and Andrew J. Millis. Continuous-time solver for quantum impurity models. *Phys. Rev. Lett.*, 97:076405, Aug 2006.
- [122] Philipp Werner, Armin Comanac, Luca de' Medici, Matthias Troyer, and Andrew J. Millis. Continuous-time solver for quantum impurity models. *Phys. Rev. Lett.*, 97:076405, Aug 2006.
- [123] Philipp Werner, Rei Sakuma, Fredrik Nilsson, and Ferdi Aryasetiawan. Dynamical screening in La_2CuO_4 . *Phys. Rev. B*, 91:125142, Mar 2015.
- [124] Kenneth G. Wilson. The renormalization group: Critical phenomena and the kondo problem. *Rev. Mod. Phys.*, 47:773–840, Oct 1975.
- [125] Yi-feng Yang and David Pines. Emergent states in heavy-electron materials. *Proceedings of the National Academy of Sciences*, 109(45):E3060–E3066, 2012.
- [126] Z. P. Yin, K. Haule, and G. Kotliar. Spin dynamics and orbital-antiphase pairing symmetry in iron-based superconductors. *Nat Phys*, 10(11):845–850, 11 2014.
- [127] J. Zaanen, G. A. Sawatzky, and J. W. Allen. Band gaps and electronic structure of transition-metal compounds. *Phys. Rev. Lett.*, 55:418–421, Jul 1985.
- [128] Guoren Zhang, Evgeny Gorelov, Erik Koch, and Eva Pavarini. Importance of exchange anisotropy and superexchange for the spin-state transitions in $r\text{CoO}_3$ (r = rare earth) cobaltates. *Phys. Rev. B*, 86:184413, Nov 2012.
- [129] C. Zobel, M. Kriener, D. Bruns, J. Baier, M. Grüninger, T. Lorenz, P. Reutler, and A. Revcolevschi. Evidence for a low-spin to intermediate-spin state transition in LaCoO_3 . *Phys. Rev. B*, 66:020402, Jun 2002.
- [130] M. B. Zöfl, I. A. Nekrasov, Th. Pruschke, V. I. Anisimov, and J. Keller. Spectral and magnetic properties of α - and γ -ce from dynamical mean-field theory and local density approximation. *Phys. Rev. Lett.*, 87:276403, Dec 2001.

Appendix A

Details of the calculation of Local Screening

In this appendix, we sketch out the method to evaluate the partially screened u^{cLoc} and fully screened W^{Loc} and elaborate how the local polarization bubbles are evaluated using impurity solver ctqmc. . Since our method takes into account spin degrees of freedom explicitly, we need to reformulate the interaction matrix to factor in the spin degree of freedom. Also note that due to the Pauli principle (which was ignored by the RPA method), we cannot have two fermions with the same spin in the same orbital therefore we set the diagonal components of the interaction matrix to zero. The interaction matrix, which we name V^{Loc} , is now given (in terms of the Hubbard U parameters defined in Chapter 9) by :

$$V^{Loc} = \begin{array}{c|cccc} & d \uparrow & d \downarrow & p \uparrow & p \downarrow \\ \hline d \uparrow & 0 & U_{dd} & U_{dp} & U_{dp} \\ d \downarrow & U_{dd} & 0 & U_{dp} & U_{dp} \\ p \uparrow & U_{dp} & U_{dp} & 0 & U_{pp} \\ p \downarrow & U_{dp} & U_{dp} & U_{pp} & 0 \end{array} \quad (A.1)$$

The basic quantity we want to measure here is the local Polarization bubble P^{Loc} , whose matrix elements shall henceforth be denoted for notational efficiency by \tilde{P}_β^α , which will be calculated from the fourier transform of :

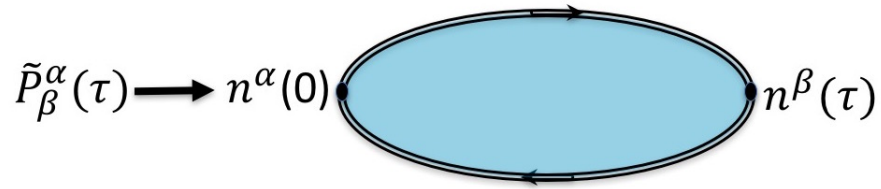


Figure A.1: Diagrammatic Representation of a general matrix element of the local Polarization bubble. The blue shading indicates that we take into account all interaction processes inside the impurity. α and β are condensed spin and orbital indices. It is to be noted that we only calculate the local (impurity) bubble hence there is no q dependence

The CTQMC impurity solver gives us access to the impurity spin and charge susceptibilities χ_c and χ_s which measure the charge and spin autocorrelation functions given by-

$$\chi_s(i\omega) = \int_0^\beta \sum_{\alpha\beta} e^{i\omega\tau} \langle S_z^\alpha(\tau) S_z^\beta(0) \rangle \quad (\text{A.2})$$

$$\chi_c(i\omega) = \int_0^\beta \sum_{\alpha\beta} e^{i\omega\tau} \langle n^\alpha(\tau) n^\beta(0) \rangle \quad (\text{A.3})$$

Where α and β are condensed spin and orbital indices. Now in order to get \tilde{P} matrix elements from these susceptibilities, we first set the spin observable of each electron artificially to ± 1 instead of $\pm \frac{1}{2}$ as that allows us to get rid of factors of 4 in denominator which would have otherwise been present. Note also that since our Hamiltonian has spin symmetry in the paramagnetic phase, we can define new variables $a \dots f$ using the relationships: $\tilde{P}_{d\uparrow}^{d\uparrow} = \tilde{P}_{d\downarrow}^{d\downarrow} = a$, $\tilde{P}_{p\uparrow}^{p\uparrow} = \tilde{P}_{p\downarrow}^{p\downarrow} = b$, $\tilde{P}_{d\downarrow}^{d\uparrow} = \tilde{P}_{d\uparrow}^{d\downarrow} = c$, $\tilde{P}_{p\downarrow}^{p\uparrow} = \tilde{P}_{p\uparrow}^{p\downarrow} = d$, $\tilde{P}_{p\uparrow}^{d\uparrow} = \tilde{P}_{p\downarrow}^{d\downarrow} = \tilde{P}_{d\uparrow}^{p\uparrow} = \tilde{P}_{d\downarrow}^{p\downarrow} = e$, $\tilde{P}_{p\downarrow}^{d\uparrow} = \tilde{P}_{p\uparrow}^{d\downarrow} = \tilde{P}_{d\downarrow}^{p\uparrow} = \tilde{P}_{d\uparrow}^{p\downarrow} = f$. Adopting these definitions, we see that the new impurity charge and spin susceptibilities calculated by CTQMC obey:

$$\chi_c = 2(a + b + c + d) + 4(e + f) \quad (\text{A.4})$$

$$\chi_s = 2(a + b - c - d) + 4(e - f)$$

In order to get the individual variables, we further calculate the single orbital charge and spin susceptibilities using CTQMC. These give us the following identities:

$$\begin{aligned} \chi_c^{(d)} &= 2(a + c), \chi_s^{(d)} = 2(a - c) \\ \chi_c^{(p)} &= 2(b + d), \chi_s^{(p)} = 2(b - d) \end{aligned} \quad (\text{A.5})$$

By solving these equations we can obtain $\{a \dots f\}$ from the sampled $\chi_s, \chi_c, \chi_c^{(\alpha)}, \chi_s^{(\alpha)}$ ($\alpha = p, d$) to get:

$$a = \frac{\chi_c^{(d)} + \chi_s^{(d)}}{4}, c = \frac{\chi_c^{(d)} - \chi_s^{(d)}}{4} \quad (\text{A.6})$$

$$b = \frac{\chi_c^{(p)} + \chi_s^{(p)}}{4}, d = \frac{\chi_c^{(p)} - \chi_s^{(p)}}{4} \quad (\text{A.7})$$

$$e = \frac{1}{8}(\chi_c + \chi_s) - \frac{1}{2}(a + b) \quad (\text{A.8})$$

$$f = \frac{1}{8}(\chi_c - \chi_s) - \frac{1}{2}(c + d) \quad (\text{A.9})$$

Now we have all of the quantities defined to calculate the local Polarization matrix \tilde{P} given by:

$$P^{Loc} = \begin{pmatrix} \tilde{P}_{d\uparrow}^{d\uparrow} & \tilde{P}_{d\downarrow}^{d\uparrow} & \tilde{P}_{p\uparrow}^{d\uparrow} & \tilde{P}_{p\downarrow}^{d\uparrow} \\ \tilde{P}_{d\uparrow}^{d\downarrow} & \tilde{P}_{d\downarrow}^{d\downarrow} & \tilde{P}_{p\uparrow}^{d\downarrow} & \tilde{P}_{p\downarrow}^{d\downarrow} \\ \tilde{P}_{d\uparrow}^{p\uparrow} & \tilde{P}_{d\downarrow}^{p\uparrow} & \tilde{P}_{p\uparrow}^{p\uparrow} & \tilde{P}_{p\downarrow}^{p\uparrow} \\ \tilde{P}_{d\uparrow}^{p\downarrow} & \tilde{P}_{d\downarrow}^{p\downarrow} & \tilde{P}_{p\uparrow}^{p\downarrow} & \tilde{P}_{p\downarrow}^{p\downarrow} \end{pmatrix} \quad (A.10)$$

In order to define a cRPA-like algorithm, we now define P_d^{Loc} as the top 2x2 submatrix of P^{Loc}

$$P_d^{Loc} = \tilde{P}_{ds'}^{ds}, (s, s' = \uparrow, \downarrow) \quad (A.11)$$

We then complete the formalism by defining:

$$P_r^{Loc} = P^{Loc} - P_d^{Loc} \quad (A.12)$$

Now, having obtained the Polarization matrix, we use a cRPA like expansion to obtain the new partially screened u^{Loc} and W^{Loc} by the same diagrammatic expansion as used in the RPA procedure, but with the new P^{Loc} as shown in Fig A.2

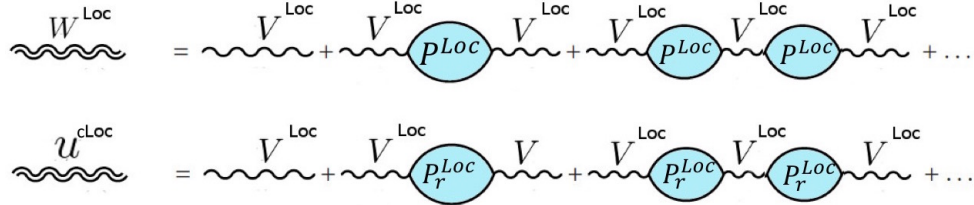


Figure A.2: Diagrammatic representation of the procedure to calculate the new screened interaction parameters using the local Polarization

or explicitly, we get:

$$u^{cLoc} = V^{Loc}(\mathbf{1} - P_r^{Loc}V^{Loc})^{-1} \quad (A.13)$$

$$W^{Loc} = u^{cLoc}(\mathbf{1} - P_d^{Loc}u^{cLoc})^{-1} \quad (A.14)$$

So in this section we have obtained an alternative method to estimate screening of coulomb interaction between electrons within the impurity. As mentioned before, the accurate results obtained using this process is an illustration of the fact that RPA is inadequate. This method cannot provide us with apriori knowledge of screening because we need to run the impurity solver before we obtain these polarization bubbles which precludes this method being used as a predictive tool.

Moreover the calculation of all the orbital-specific polarizations requires multiple impurity solver iterations to be performed with specific inputs, which is a time consuming process. However, the fact that we have obtained more accurate results using this screening procedure, which predicts much reduced screening compared to cRPA shows that DMFT already contains most relevant screening processes (hybridization screening) and the RPA diagrams are not the dominant ones when it comes to estimating local screening.